Metal oxide supported iron-nickel nano-alloys in the reverse water-gas shift reaction

By

Karina de Kock

BScEng in Chemical Engineering, University of Cape Town (2019)

Dissertation submitted to the University of Cape Town in partial fulfilment of the requirements for the degree of

Master of Science in Engineering

DSI-NRF Centre of Excellence in Catalysis (c*change)

Centre for Catalysis Research

Department of Chemical Engineering

University of Cape Town

South Africa

February 2023

CAT CENTRE
Centre for Catalysis Research

cchange
DST-NRF Centre of Excellence in Catalysis

PLAGIARISM DECLARATION

I know the meaning of plagiarism and declare that all the work in the document, save for that which is properly acknowledged, is my own. This thesis/dissertation has been submitted to the Turnitin module (or equivalent similarity and originality checking software) and I confirm that my supervisors have seen my report and any concerns revealed by such have been resolved with my supervisors.

Signed by candidate

Name: Karina de Kock

Date: 30 July 2023

ACKNOWLEDGEMENTS

This study started in April 2021 and was completed by February 2023 at the Catalysis Institute in the Department of Chemical Engineering at the University of Cape Town, South Africa.

First and foremost, thank you to my supervisors, Assoc. Prof. Nico Fischer and Prof. Michael Claeys. To Nico, thank you for giving me this opportunity and for all the time and energy you gave to this project. I am extremely grateful for your expertise, warm guidance, and open-door policy. It has been a great pleasure to work within your group and to learn from you.

To Dr Shaine Raseale and Dr Wijnand Marquart – I cannot thank you two enough for your endless patience even though you were finalizing your PhD theses during this time. It was an immense privilege to receive the support and guidance that I did, and your generosity of time and knowledge made an immeasurable difference to my project and my experience within the group. To Percy Ketlogetswe and Lindo Ngema – thank you for all the support, engagement, and encouragement. I wish all of you the best for the future.

Thank you to the Analytical Laboratory for carrying out ICP-OES and BET analysis, to Mohamed Jaffer for assistance with TEM, to Miranda Waldron for carrying out SEM/EDX analysis and Raman spectroscopy and to the Catalysis Institute technical team for the countless ways in which they supported me in the lab.

Thank you to DSI-NRF Centre of Excellence in Catalysis c*change for your financial support of this work.

Lastly, I would like to thank my friends and family for cheering me on along the way. I express my deepest gratitude to my parents, John and Karen de Kock, for their unconditional love and support and for the many sacrifices they have made. Thank you to Matthew Russell for being the best partner and friend, for going through the highs and lows with me and for picking up the slack during the harder weeks.

SYNOPSIS

Rising atmospheric CO_2 concentrations pose an existential threat to human life. The development of carbon capture and utilization (CCU) technologies which can consume CO_2 at the same scale that it's being produced are necessary to limit the global mean surface temperature increase to 2 °C, in accordance with the Paris Agreement. A challenge in developing these technologies is to activate CO_2, which is thermodynamically low in energy and needs to be reacted with high energy molecules. The Power-to-X (PtX) concept considers various pathways and technologies for the conversion of CO_2 to different target products. PtX assumes the availability of cheap renewable energy and green H_2 in the future and in many of these scenarios, CO_2 is first activated to carbon monoxide via the reverse water-gas shift (RWGS) reaction.

The RWGS is thermodynamically limited. CO and CO_2 methanation are favoured over the RWGS at industrially preferred reaction conditions and there is a need for low temperature catalysts with a high CO selectivity. Noble metal catalysts have been well studied for the RWGS, though affordable and abundant metals are required for large-scale applications. Iron-based catalysts have been widely explored due to their high stability, while nickel catalysts are rarely considered for the RWGS due to their known hydrogenation activity. Metal oxide (MOx) catalysts, such as ceria, have also been studied for the RWGS due to their high oxygen storage capacity and reducibility at high temperatures.

In recent work from the group of Fischer at the University of Cape Town, supported Fe-Ni nanoparticles showed promising CO_2 activation potential. It was found that upon reduction of the oxidic Fe-Ni precursor nanoparticles, a mixture of fcc and bcc alloy phases was formed. An increase in Fe content increased the concentration of the bcc phase in the alloy. It was further demonstrated that the bcc surface of the Fe-Ni alloy activates CO_2 while the fcc surface of the alloy appears to be inert.

This work further studies the Fe_xNi_y/MOx catalysts developed by the group of Fischer, which make use of novel synthesis approaches. The reducibility of two different MOx support materials is studied (M = Cr and Ga). To limit the effect of the varying physical properties of the respective bulk oxides on catalyst performance, bespoke support materials were prepared by impregnating a common γ-Al_2O_3 carrier with MOx overlayers. The surface of the prepared materials has the chemical and electronic properties of the respective MOx, but the pore geometry of the γ-Al_2O_3 is maintained. The effect of iron content on catalytic performance is of interest, and to obtain the Fe-Ni alloy phase, oxidic $(Ni_xFe_{1-x})Fe_2O_4$ precursor nanoparticles of varying composition are synthesized (Fe:Ni = 3, 5 and 7, as well as pure iron oxide). This approach increases the chance of alloy formation upon reduction of the precursor particles compared to techniques such as co-impregnation, as the Fe and Ni are well mixed in the precursor particle. A hydrothermal synthesis technique in benzyl alcohol is employed to produce

nanoparticles with a narrow size distribution without the use of surfactants, which are difficult to remove and can influence catalytic performance. The nanoparticles are deposited onto the two $MOx@Al_2O_3$ overlayer materials, as well as onto inert SiO_2 to isolate the performance of the metallic Fe-Ni phases without support effects.

Characterizations of the unsupported $(Ni_xFe_{1-x})Fe_2O_4$ confirm that nanoparticles of varying composition are successfully synthesized in the correct phase with satisfactory overlap in particle size distribution. Characterizations of the prepared $MOx@Al_2O_3$ overlayer support materials confirm that the desirable textural properties of the underlying γ-Al_2O_3 support are maintained. No bulk MOx crystallites are detected, suggesting the MOx exists as a 2D overlayer covering the γ-Al_2O_3 surface. H_2-TPR studies in *in-situ* XRD confirm that the reduced catalysts contain a mixture of a bcc alloy phase and an fcc alloy phase in agreement with the previous work and irrespective of the support material. The relative concentrations of each phase are a function of iron content, with an increase in iron content increasing the concentration of the bcc alloy phase. *In-situ* XRD temperature-programmed CO_2 activation experiments confirm that the bcc phase has a high affinity towards re-oxidation but, unlike in the previous work, the fcc phase was found to be partially re-oxidized at elevated temperatures (> 600 °C).

Catalytic performance evaluation was carried out in a dual quartz tube fixed-bed reactor set-up at 600 °C. All samples tested show > 99% CO selectivity but, using $Fe100/SiO_2$ as a reference catalyst, it was found that alloying Fe with Ni and the use of an active support has significant impacts on catalytic activity and stability. The SiO_2-supported samples all deactivated rapidly and in general, the CrOx-supported samples have the best activity, and the GaOx-supported samples have the best stability. Catalytic performance is dependent on both the alloy composition and the MOx support, with the surprising observation made of a reversal of the trend in activity with iron content between $CrOx@Al_2O_3$ and $GaOx@Al_2O_3$.

Spent catalyst characterization showed that the rapid deactivation seen on SiO_2 cannot be explained by sintering, oxidation, or carbon deposition. The deactivation is instead credited to the consumption of the bcc phase under reaction conditions. The results show that there is some interaction between the fcc phase and an active supports which enhances RWGS performance. Possible untested explanations for this could be enhanced H_2 activation on the fcc phase which boosts CO_2 activation on the support through a H^+ spillover effect, or the creation of new active sites at the metal-metal oxide interface which are RWGS active.

TABLE OF CONTENTS

LIST OF FIGURES

LIST OF TABLES

GLOSSARY & NOMENCLATURE

Al_2O_3	Alumina
Ar	Argon
bcc	Body centered cubic
BET	Brunauer–Emmett–Teller
BJH	Barrett, Joyner and Halenda
CCS	Carbon capture and storage
CCU	Carbon capture and utilization
CO	Carbon monoxide
CO_2	Carbon dioxide
CO_2-ODH	CO_2-mediated oxidative dehydrogenation
Cu	Copper
d_N	Number based average particle size
d_V	Volume based average crystallite size
EXAFS	Extended X-ray absorption fine structure
fcc	Face centered cubic
Fe	Iron
FeO_x	Iron oxides
FTS	Fischer-Tropsch synthesis
GHG	Greenhouse gas
H_2	Hydrogen
H_2O	Water
HT-WGS	High temperature water-gas shift
ICP-OES	Inductively coupled plasma optical emission spectroscopy
IPCC	Intergovernmental Panel on Climate Change
K	Potassium
LT-WGS	Low temperature water-gas shift
Mo	Molybdenum
MOx	Metal oxides
Ni	Nickel
PTFE	Polytetrafluoroethylene
PtL	Power-to-Liquids
PtX	Power-to-X
RWGS	Reverse water-gas shift

SDG	Sustainable development goal
STEM-EDX	Scanning transmission electron microscopy energy-dispersive X-ray spectroscopy
TEM	Transmission electron microscopy
TGA	Thermogravimetric analysis
TOS	Time on stream
TPR	Temperature-programmed reduction
XPS	X-ray photoelectron spectroscopy
XRD	X-ray diffraction
Θ	Diffraction angle
σ_N	Number based standard deviation

1. INTRODUCTION

Ever-increasing concentrations of atmospheric CO_2 present an existential threat to human life. The development of carbon utilization technologies which mitigate anthropogenic CO_2 emissions is desired in the effort to remain within the 2°C limit in global mean surface temperature increase established by the Intergovernmental Panel on Climate Change (IPCC) and stipulated in the Paris Agreement (IPCC, 2018).

The reverse water-gas shift reaction (RWGS) is the reduction of CO_2 with H_2 to form CO and water. The combination of Fischer-Tropsch synthesis (FTS) and the RWGS in a Power-to-Liquids (PtL) scenario provides a promising pathway to transition global transport sectors from a fossil-fuel basis to a renewable energy basis, with the assumption of the availability of affordable renewable energy and green H_2 in the future. This has benefits over other envisioned futures for green energy in that PtL takes advantage of the preexisting infrastructure for the transportation, storage, and utilization of liquid fuels, particularly in sectors that are challenging to electrify such as aviation. Over and above this application, CO is a versatile feedstock which can be used in any of the well-established syngas conversion processes. Thus, the study of the RWGS has attracted attention in recent years as a potential carbon utilization mechanism (Schmidt et al., 2018).

The RWGS is endothermic and is therefore thermodynamically favored at high temperatures. At lower reaction temperatures, methanation is dominant over the RWGS, so designing highly selective, low-temperature RWGS catalysts is challenging. The catalytic features required for RWGS catalysis include good CO_2 adsorption and dissociation; good H_2 adsorption and dissociation; and a weak CO adsorption ability to promote its release and prevent its hydrogenation (Daza & Kuhn, 2016). Typically, RWGS catalysts are active transition metals on a reducible metal oxide support which work in tandem (Porosoff & Chen, 2013). There is good agreement in literature that the RWGS reaction proceeds via a tandem mechanism, and metal-support interactions must be tuned to promote CO formation and suppress CH_4 formation (Yan, Binhang et al., 2019).

Abundant and economically viable metals would be required for the development of an industrial RWGS process which can consume CO_2 at the same scale that it is being emitted. The RWGS is not itself an industrially developed process, but it is applied to adjust the H_2:CO ratio in syngas for various applications over iron-based catalysts, which are used to catalyze the high temperature water-gas shift (WGS).

In a recent publication by Raseale et al. (2021), supported Fe_xNi_y nanoparticles of various metallic composition demonstrated CO_2 activation potential. To obtain different Fe_xNi_y alloy phases, oxidic

precursor nanoparticles were first synthesized via the surfactant-free, hydrothermal synthesis technique in benzyl alcohol. The intimate mixing of Fe and Ni in the precursor particle increases the chance of alloy formation upon reduction, compared to techniques such as co-impregnation. It was found that upon reduction of the oxidic Fe_xNi_y precursor nanoparticles, a mixture of fcc and bcc alloy phases was formed. An increase in Fe content increased the concentration of the bcc phase in the alloy. This observation agrees with the trends predicted by bulk Fe-Ni phase diagrams reported in literature, supported that different Fe-Ni alloy phases were formed rather than distinct and segregated monometallic phases (Predel, 1995). It was further suggested that the bcc surface of the Fe-Ni alloy activates CO_2 while the fcc surface of the alloy is inert under the studied conditions (Raseale et al., 2021).

Support effects were also investigated by Raseale et al. (2021). To limit the effect of varying textural properties of the chosen support materials on catalytic performance, bespoke support materials were prepared via the impregnation of a common alumina carrier with various metal oxide (MOx) overlayers. Thus, the surface of the prepared materials had the chemical and electronic properties of the MOx overlayer material while the pore geometry of the underlying carrier was maintained.

The aim of the present work is to further study the Fe_xNi_y/MOx catalysts developed by Raseale et al. (2021) in the RWGS. The effect of iron content in the precursor particle, and therefore the alloy composition in the reduced catalyst samples, is studied by preparing oxidic Fe_xNi_y nanoparticles of varying composition via the hydrothermal method in benzyl alcohol. The atomic ratios studied are Fe:Ni = 3, 5 and 7 as well as pure iron oxide in the spinel structure, $FeFe_2O_4$. In addition, the effect of different MOx support materials was studied by preparing two different MOx overlayers dispersed on a common alumina carrier. The chosen materials are oxides of chromium ($CrOx@Al_2O_3$) and gallium ($GaOx@Al_2O_3$). The nanoparticles were deposited onto the prepared supports, as well as onto inert SiO_2. The prepared materials have been characterized and evaluated under RWGS conditions. *In-situ* XRD characterization is used to understand the phase evolution of the samples during reduction and for CO_2 activation in the absence of H_2.

2. LITERATURE REVIEW

This chapter discusses the urgent need for the development of carbon capture and utilization (CCU) technologies which consume CO_2 in quantities large enough to relieve the environmental pressures presented by rising atmospheric CO_2 levels. The role of the reverse water-gas shift (RWGS) in a power-to-liquids (PtL) concept is discussed as a potential pathway to consume CO_2 in a closed loop, particularly for application in aviation, a sector which is typically difficult to abate. The need for efficient, abundant, and cost-effective catalytic materials for the RWGS is demonstrated and a motivation for the use of MOx-supported iron-nickel alloy systems is provided. Lastly, synthesis methods for the preparation of these materials are discussed.

2.1 CLIMATE CHANGE AND THE PTL PATHWAY

The Intergovernmental Panel on Climate Change (IPCC) has stated that without additional efforts to reduce anthropogenic greenhouse gas (GHG) emissions, the global mean surface temperature is expected to increase by 4.8°C by the year 2100 compared to pre-industrial levels. This would have severe adverse effects on food security, human security, human health, water supply, and livelihoods (IPCC, 2018). In response to the existential threat posed by this global warming, the 2015 United Nations Climate Change Conference of the Parties (COP 21) set a target to limit the increase in the global average temperature to ‘‘well below 2 °C’’ with a further aspirational goal of 1.5°, requiring major reductions in GHG emissions across all sectors (Savaresi, 2016). Fossil fuel-related CO_2 emissions account for 76% of total anthropogenic GHG emissions (IPCC, 2014). While the use of carbon-neutral and renewable energy resources is rising, the world remains heavily reliant on fossil fuels to meet its energy demand (Tollefson, 2018). Carbon capture and storage (CCS) and carbon capture and utilization (CCU) technologies are considered by many researchers to be the only way to maintain atmospheric CO_2 concentrations below the limits established by the Paris Agreement.

It is estimated that more than 150 times more CO_2 is produced than what is currently consumed by industrial processes as well as what can potentially be sequestered by ‘large’ projects under evaluation. The use of CCS to reduce CO_2 emissions is limited by its high energy requirement, and hence excessive cost (Daza & Kuhn, 2016). In addition, the effects of CCS on the environment are unknown, and the capacity of carbon storage by mineralization, oceanic or geological means does not match the increasing rate of CO_2 production. Considering this, the research, development, and industrialization of CCU technologies to turn CO_2 from a liability into a cheap and abundant feedstock is a promising and potentially sustainable route (Zhu, Ge & Zhu, 2020).

The industrially developed processes which consume CO_2 are limited, as shown by Figure 2-1 below. Noting the logarithmic scale of the y-axis, urea production accounts for more than 50% of the annual CO_2 usage and other products include salicylic acid and methanol, though the demand for these chemicals is low. A challenge in developing reliable CCU technologies is matching the scale of CO_2 production to a CO_2-derived product with an equally high demand. For example, it has been estimated that to synthesize all the chemicals currently derived from oil from CO_2 would reduce CO_2 emissions by just 3.8% (Daza & Kuhn, 2016). A further challenge in developing these technologies is to activate CO_2 which is thermodynamically low in energy and needs to be reacted with high energy molecules.

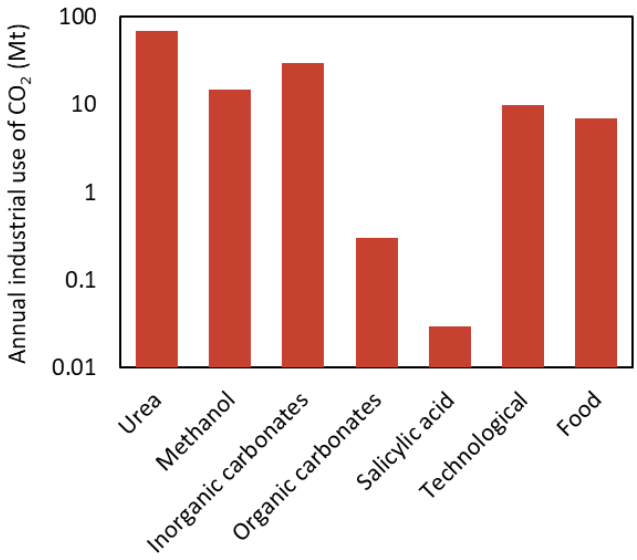

Figure 2-1: The annual industrial use of CO_2 in megatons. Reproduced from Mikkelsen, Jørgensen and Krebs (2010).

Oil accounts for 40.8% of the world's total energy consumption, and nearly two thirds of the world's oil is used to produce transportation fuels. It accounts for 34.1% global CO_2 emissions from fossil fuel combustion (IEA, 2020). In addition to the well-matched scale of CO_2 emissions to the demand for liquid fuels, the infrastructure for liquid fuel storage, transport and utilization is well-established globally.

The power-to-liquids (PtL) pathway is a scalable solution for the transition of global transport systems from a fossil fuel-basis to a renewable basis. Liquid fuels can be produced via the Fischer-Tropsch synthesis (FTS) as shown in Figure 2-2 below, or via the production of methanol as an intermediate product. PtL is spoken of mostly in the context of liquid fuels for aviation as this sector is difficult to abate (Schmidt et al., 2018).

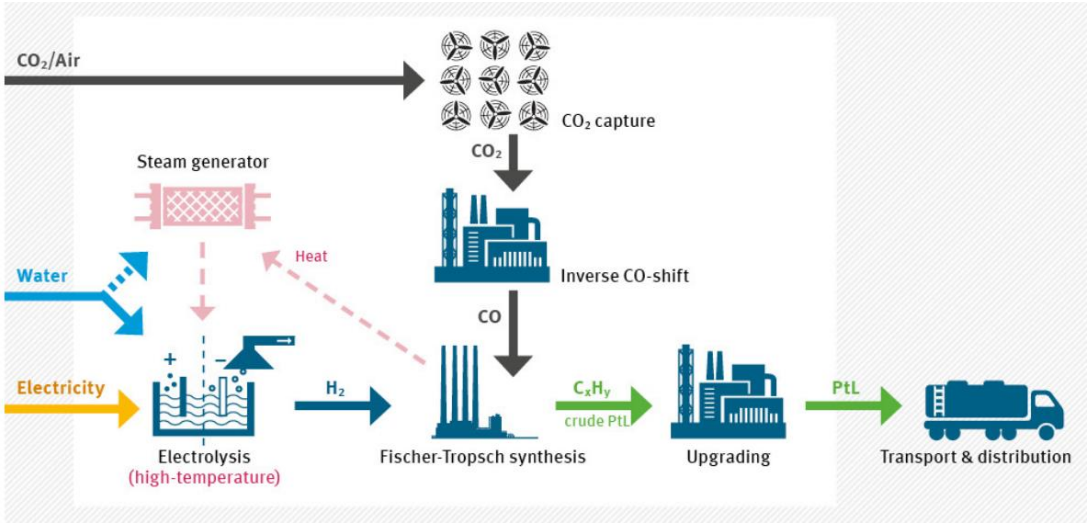

Figure 2-2: FTS pathway to produce PtL, including the option of using high-temperature electrolysis (Schmidt et al., 2018).

In a generic PtL scheme, CO_2 is captured directly from air or from a point source of emissions. Green H_2 is produced via water electrolysis powered by renewable energy. CO_2 is then activated to CO via the reverse water-gas shift reaction (RWGS) which is used to produce C_xH_y via the FTS, which is a well-established production route for liquid hydrocarbons from synthesis gas (see Equation 2-1 below). While the synthesis gas feedstock is currently produced via coal gasification or natural gas reforming, the use of the RWGS (see Equation 2-2 below) allows for FTS products to be produced in a closed carbon loop.

$$CO + 2H_2 \leftrightarrow (-CH_2-) + H_2O \qquad \text{Eq 2-1}$$

$$CO_2 + H_2 \leftrightarrow CO + H_2O \qquad \text{Eq 2-2}$$

Alternatives to the FTS route for PtL have been proposed, as the CO produced from the RWGS can be used as a feedstock for any of the well-established syngas conversion processes, as shown in Figure 2-3 below. Thus, Power-to-X (PtX) has been applied as a more general term for these processes which aim to couple green H_2 with captured CO_2 to produce useful products.

This motivates the study of the RWGS, as a good understanding of RWGS catalysis is required for the industrial development of PtX processes which can address our current carbon crisis.

2.1 CATALYTS FOR THE RWGS REACTION

As discussed above, the conversion of CO_2 to CO via the RWGS reaction (Equation 2-2) is studied because the CO produced can be further converted to valuable chemicals and fuels through well-established syngas conversion technologies. Considerations for the catalysis of the RWGS reaction are discussed below.

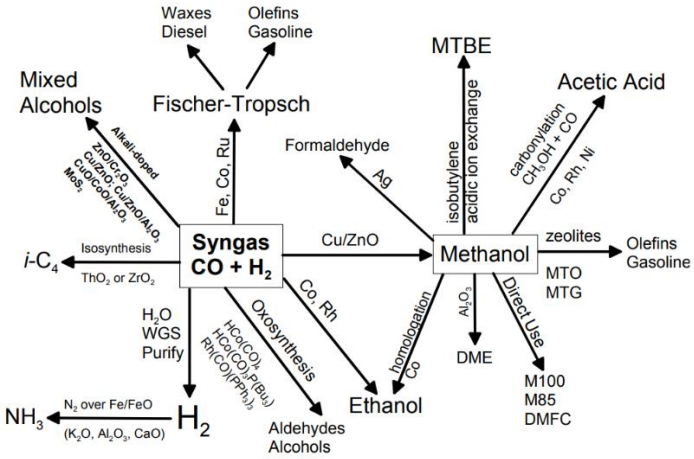

Figure 2-3: Diagram of syngas conversion processes (Spath & Dayton, 2003).

2.1.1 Thermodynamics and activity

CO_2 is a thermodynamically stable molecule with a standard Gibbs free energy of -394.38 kJ/mol. A large amount of energy is required for CO_2 activation by the cleavage the first C=O bond - the molecular dissociation energy of CO_2 is 750 kJ/mol. These thermodynamic limitations of the RWGS can be intuitively understood as CO_2 is one of the terminal products of fossil fuel combustion, together with water (Su et al., 2017).

The RWGS is mildly endothermic in nature and is therefore thermodynamically favored at elevated temperatures. Equilibrium conversion increases with an increase in excess hydrogen and equilibrium conversion is not affected by pressure. Kaiser et al. (2013) analyzed the equilibrium composition of RWGS with temperatures for a molar feed ratio in H_2:CO_2 of 3 at atmospheric pressure, illustrated by Figure 2-4 below. Figure 2-4 shows that at temperatures below 600°C, strongly exothermic methane production is thermodynamically favored over RWGS. Methane is produced from CO_2 (Sabatier reaction) and CO via Equations 2-3 and 2-4 below, respectively, which consume a large amount of valuable hydrogen. At temperatures above 700°C , CO is the prominent product and little or no methane is formed, but the energy requirement and technical considerations of operating above 700°C are limiting. This highlights the challenge in designing highly selective RWGS catalysts at commercially preferred, lower reaction temperatures.

$$CO_2 + 4H_2 \leftrightarrow CH_4 + 2H_2O \qquad \text{Eq 2-3}$$

$$CO + 3H_2 \leftrightarrow CH_4 + H_2O \qquad \text{Eq 2-4}$$

The RWGS is also competed by methanol formation, but this is low or absent at atmospheric pressure and is often ignored (Xiaoding & Moulijn, 1996). In a future industrially developed process, product

separation and/or recycle could be used to further improve the overall conversion of CO_2 beyond these thermodynamic limitations (Daza & Kuhn, 2016).

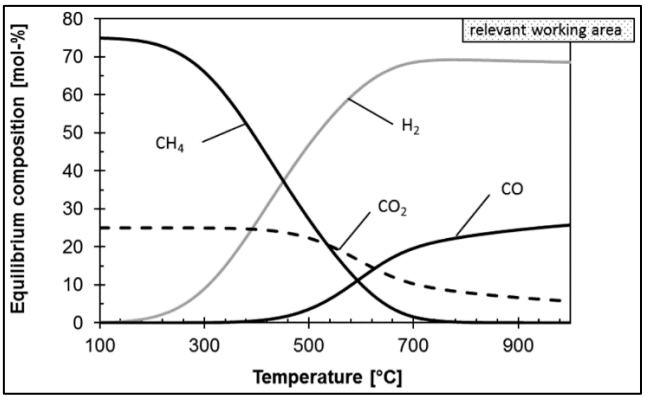

Figure 2-4: Thermodynamic equilibrium composition of the product gas of RWGS reaction at 0.1 MPa for a molar H_2/CO_2 inlet ratio of 3 (Kaiser et al., 2013).

Although the reverse water gas shift is not directly used as an industrially developed process, it is understood to be an intermediate step in the Sabatier reaction (Equation 2-3 above) and in the methanol synthesis. It is also applied to adjust the H_2:CO ratio in syngas for various applications such as to increase the carbon efficiency of the FTS (Bukur, Todic & Elbashir, 2016). Catalytic features required for RWGS catalysts include good CO_2 adsorption and dissociation, good H_2 adsorption and dissociation, and a weak CO adsorption ability to promote its release and prevent its hydrogenation (Zhu, Ge & Zhu, 2020). There is good agreement in literature that the RWGS reaction proceeds via a tandem mechanism. Metal-support interactions must be tuned to promote CO formation and suppress CH_4 formation (Porosoff & Chen, 2013). The nature of the active metal has great influence on the CO selectivity while the choice of support material has a great influence on catalyst activity (Yang et al., 2020). In addition to supported transition metal catalysts, which will be explored below, transition metal carbides have been studied for RWGS (Su et al., 2017).

2.1.2 Mechanisms

Two mechanisms for the RWGS reaction are proposed - the redox mechanism and the associative mechanism, both of which involve oxygen exchange with active sites in the catalyst. These mechanisms are proposed on the basis of reaction kinetics, spectroscopy and density functional theory (DFT) calculations (Zhu, Ge & Zhu, 2020).

The typical reaction pathway of the redox mechanism for RWGS is shown by Equations 2- 5 to 12 below. In this mechanism, CO_2 is reduced to CO with the catalyst being oxidized. The redox mechanism was originally proposed by Ginés, Marchi and Apesteguía (1997) over Cu-based catalysts where the catalytic cycle is completed by H_2 reducing the catalyst again, forming H_2O (Equation 2-13 and Equation 2-14 below). This was studied by submitting catalyst samples to consecutive CO_2 /H_2 cycles

under thermogravimetric analysis (TGA). This regenerative Mars van Krevelen-type mechanism is typically proposed for catalysts containing reducible oxides (Zhu, Ge & Zhu, 2020).

$$H_2 + 2* \rightarrow H* + H* \quad \text{Eq 2-5}$$

$$CO_2 + * \rightarrow CO_2* \quad \text{Eq 2-6}$$

$$CO_2* + * \rightarrow CO* + O* \quad \text{Eq 2-7}$$

$$H* + O* \rightarrow OH* + * \quad \text{Eq 2-8}$$

$$H* + OH* \rightarrow H_2O* \quad \text{Eq 2-9}$$

$$OH* + OH* \rightarrow H_2O* + O* \quad \text{Eq 2-10}$$

$$H_2O* \rightarrow H_2O + * \quad \text{Eq 2-11}$$

$$CO* \rightarrow CO + * \quad \text{Eq 2-12}$$

$$CO_{2(g)} + 2Cu^0_{(s)} \rightarrow CO_{(g)} + Cu_2O_{(s)} \quad \text{Eq 2-13}$$

$$H_{2(g)} + Cu_2O_{(s)} \rightarrow H_2O_{(g)} + + 2Cu^0_{(s)} \quad \text{Eq 2-14}$$

The second proposed mechanism for RWGS catalysis, the associative mechanism or formate decomposition mechanism, is shown by Equations 2- 15 to 23 below. Here the adsorbed CO_2 doesn't dissociate but rather reacts with dissociated surface H to form an intermediate species. The C=O bonds are cleaved, and the intermediate species decomposes to CO and H_2O (Zhu, Ge & Zhu, 2020).

$$H_2 + 2* \rightarrow H* + H* \quad \text{Eq 2-15}$$

$$CO_2 + * \rightarrow CO_2* \quad \text{Eq 2-16}$$

$$CO_2* + H* \rightarrow HCOO*(COOH*) + * \quad \text{Eq 2-17}$$

$$HCOO*(COOH*) + * \rightarrow HCO*(COH*) + O* \quad \text{Eq 2-18}$$

$$HCO*(COH*) + * \rightarrow CO* + H* \quad \text{Eq 2-19}$$

$$COOH* + * \rightarrow CO* + OH* \quad \text{Eq 2-20}$$

$$H* + OH* \rightarrow H_2O* \quad \text{Eq 2-21}$$

$$H_2O* \rightarrow H_2O + * \quad \text{Eq 2-22}$$

$$CO* \rightarrow CO + * \quad \text{Eq 2-23}$$

The intermediate formed depends on the catalyst type and reaction conditions but may include formate, carbonate, bicarbonate, or carboxyl species. The associative mechanism for RWGS is often supported by the direct observation of these intermediate species under reaction conditions (Su et al., 2017). The associative mechanism is proposed for group VIII metals on metal oxide supports on

which hydrogen dissociation is thermoneutral and the hydrogen spillover effect causes CO_2 to hydrogenate readily (Porosoff & Chen, 2013).

Redox and associative mechanisms have been debated and as such, no consensus has been reached regarding different mechanisms over catalyst types and under reaction conditions (Zhu, Ge & Zhu, 2020). Irrespective of the mechanism followed, key features required for effective and efficient RWGS catalysis are enhanced CO_2 adsorption, to encourage a high activity at desired lower temperatures, and facile CO desorption to prevent its hydrogenation to undesired products thus to ensure high CO selectivity.

2.1.3 Catalytic materials

Supported transition metal catalysts have most widely been explored for the RWGS reaction. Supporting an active metal increases its dispersion and available surface area while limiting surface area loss by sintering. While noble metals such as Pt, Ru and Rh are known active metals for RWGS, abundant and economic active metals would be required for the development of an industrial process which can viably consume CO_2 in significant quantities. For this reason, transition metals such as Fe, Cu and Ni are of great interest for RWGS catalysts (Porosoff, Yan & Chen, 2016).

Cu is commonly used in the low temperature water-gas shift (LT-WGS) and has been reported to be active for RWGS with little to no CH_4 formation. However, at the elevated temperatures required for acceptable CO_2 conversion, Cu-based catalysts deactivate easily due to its poor thermal stability. The stability of Cu-based catalysts can be improved by the addition of Fe as a thermal stabilizer (Wang et al., 2011). Ni is known to have high hydrogenation activity, therefore methanation is the main challenge in Ni-based catalysts. It has been found that hydrogenation activity in Ni-based catalysts can be tuned by doping with Fe (Yan, Binhang et al., 2019). Fe-based catalysts are commonly used in the high temperature water-gas shift (HT-WGS), and they show near 100% selectivity for CO over CH_4 under RWGS conditions (Kim et al., 2015). However, Fe-based catalysts are less active compared to other group VIII metals. Promoters are substances with little to no catalytic activity themselves that are added to catalysts to improve their performance. Promoters such as K and Mo are used to improve the reaction rate of Fe-based catalysts (Yang et al., 2020).

As discussed in chapter 2.1.2 above, a reducible metal oxide (generalized as MOx) can donate a lattice-oxygen in a Mars-van-Krevelen type mechanism. There is good agreement in literature that the activity of a supported metal catalyst in the RWGS is influenced by the reducibility and acid-base properties of the metal oxide carrier material. Examples of irreducible supports are SiO_2 and Al_2O_3. These are used as reference materials for activity in RWGS studies, as they disperse the supported species but do not directly activate CO_2 (Zhu, Ge & Zhu, 2020). Reducible supports such as TiO_2 and CeO_2 readily

accept oxygen from CO_2. CeO_2 is a recommended support for CO_2 activation as it has a high intrinsic activity for CO_2 adsorption. As CeO_2 is highly reducible, oxygen vacancies are created on the material, particularly on the (110) surface which has shown greater activity than the (100) or (111) surfaces (Cheng, Sherman & Lo, 2013).

Porosoff and Chen (2013) investigated both support effects and the effect of alloying on RWGS catalysts in several batch reactor experiments. Monometallic and bimetallic catalysts were supported on CeO_2 and γ-Al_2O_3, representing a reducible and a non-reducible support, respectively. Figure 2-5A shows that the PtCo bimetallic catalyst showed a greater normalized CO_2 consumption than either the pure Pt or Co catalysts. All the catalysts supported on CeO_2 showed greater activity than the catalysts supported on γ-Al_2O_3 with the same composition, as seen in Figure 2-5B. It was also found that the extent to which the support was pre-reduced affected activity, with fully reduced CeO_2-supported catalysts having higher activity than partially reduced CeO_2-supported catalysts. These observations are explained by the ability of CeO_2 to store and release oxygen, with the oxygen vacancies for the reduction of CO_2 increasing as the support is reduced.

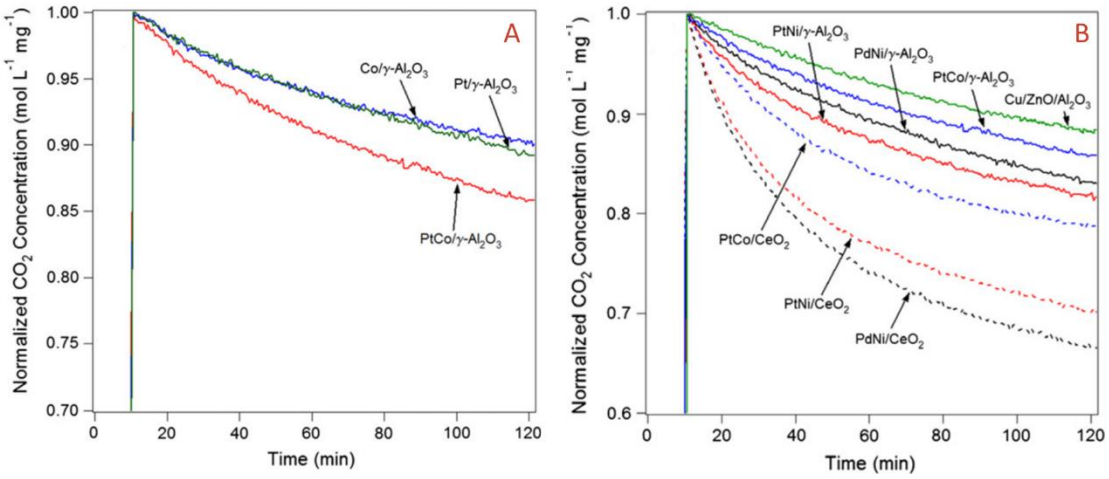

Figure 2-5: The consumption of CO_2 during the reduction of CO_2 by H_2 at 573 K for a series of Pt-Co-based catalysts, supported on γ-Al_2O_3 (A) and for a series of bimetallic catalysts, supported on γ-Al_2O_3 and CeO_2 (B) (Porosoff & Chen, 2013).

This study by Porosoff and Chen (2013) highlights the use of varying supports and bimetallic alloy formation as strategies to improve the activity and selectivity of the RWGS reaction. The addition of active metal(s) to a catalyst is a strategy to improve catalytic performance, either by introducing new active sites or new metal-oxide interfaces, or by altering the chemical and electronic properties of the catalyst surface through alloy formation (Yan, Binhang et al., 2019). Additional strategies include reducing the particle size of the metal to maximize the metal-support interfacial area, adjusting pre-treatment procedures during catalyst preparation to tune metal-support interactions, and the addition of reducible transition metal oxide or alkali metal promoters. The direct comparison in literature between different supports for RWGS is rare, specifically in which the effect of support

surface area is decoupled from the effect of the chemical and electronic nature of the support (Zhu, Ge & Zhu, 2020).

2.2 FE-NI CATALYTIC SYSTEMS

As mentioned above, the introduction of a second metal to catalyst systems can improve or modify their catalytic performance through the introduction of new active sites or through alloy formation, which alters the chemical and electronic properties of the parent metals. Bimetallic Fe-Ni systems are discussed in more detail in the following chapters.

2.2.1 Properties of Fe-Ni alloy systems

Theoretical CO_2 dissociation energy over a range of monometallic and bimetallic alloy surfaces has been predicted by DFT studies where it was found that bimetallic alloys have a lower energy barrier for CO_2 activation than their monometallic counterparts (Ko, Kim & Han, 2016). Figure 2-6 presents a map of CO_2 activation energy for the studied monometallic and bimetallic surfaces, from which the favorable dissociation energy of bimetallic alloy combinations of abundant non-noble metals (Fe, Ni and Co) can be seen.

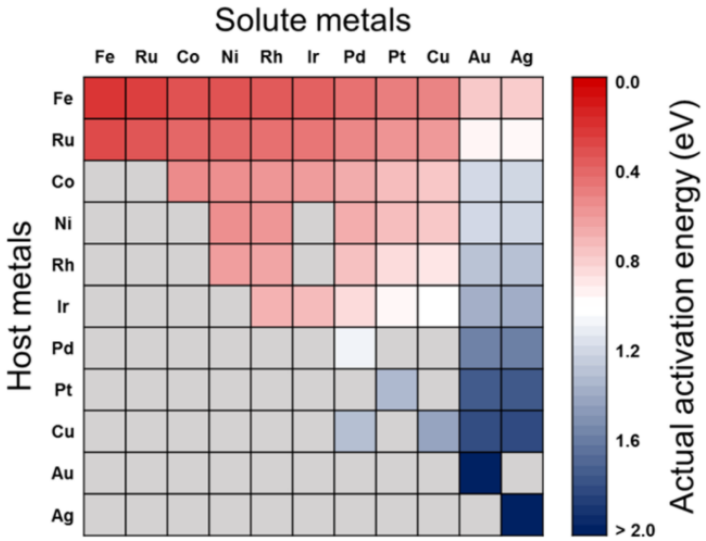

Figure 2-6: Screening for E_a^{act} for CO_2 dissociation on pure metals and bimetallic alloys. Gray cells indicate that the bimetallic alloys are not preferred due to the surface segregation of solute atoms (Ko, Kim & Han, 2016).

Bimetallic Fe-Ni systems have been studied for CO_2 activation. Ni is known to have a high intrinsic activity, while Fe is favored for its high oxygen mobility, thermal stability, and high CO:CH_4 selectivity (Su et al., 2017). Figure 2-7 below illustrates a bulk Fe-Ni phase diagram as a function of temperature and Ni content (Predel, 1995). Two allotropes of Fe-Ni alloys are observed – a body centered cubic (bcc) phase and a face centered cubic (fcc) phase. At temperatures below 350 °C only the bcc phase is present. Above 330 °C, either a mix of bcc & fcc phases are present, or pure fcc phase is present, depending on the atomic % of Ni in the alloy. Above 330 °C, the bcc allotrope is more stable with

decreasing Ni content i.e., increasing Fe content. It is not well understood whether the trends predicted by bulk phase diagrams can be used to predict behavior in nanoalloys.

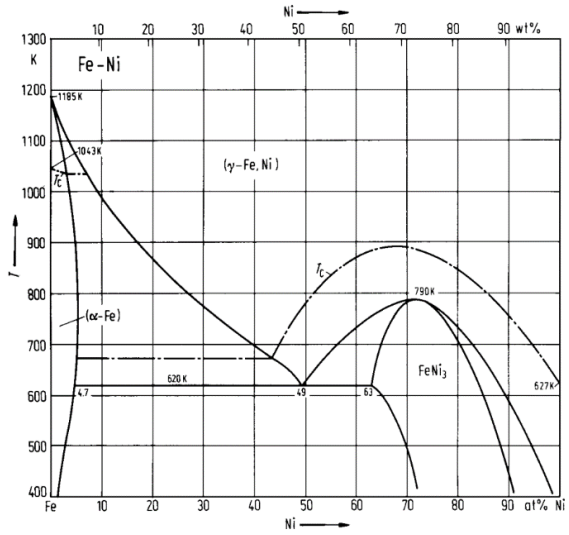

Figure 2-7 : Bulk Fe-Ni phase diagram as function of temperature Ni content (Predel, 1995).

2.2.2 Synthesis and characterization of Fe-Ni nanoalloys

The group of Chen prepared Ni/CeO_2, Fe/CeO_2 and bimetallic $Ni\text{-}Fe/CeO_2$ catalysts of varying composition by impregnation and co-impregnation, respectively. Extended X-ray absorption fine structure (EXAFS) results supported the formation of Ni-Fe alloy bonds due to the slight increase in bond length compared to the pure Ni catalyst. The phases present in the prepared catalysts were characterized by XRD as a Ni-rich fcc phase and a mixture of amorphous and crystalline iron oxides, FeO_x (Yan, B. et al., 2018). In a later publication the same group prepared ZrO_2-supported Ni_3Fe_x catalysts of varying composition (x = 0, 1, 2, 3 and 9) by the same method but here, the phases present were characterized only as metallic Ni and FeO_x and no suggestion of alloy formation was made (Yan, Binhang et al., 2019). The non-homogenous distribution of Ni and Fe in the spent Ni_xFe_y samples after CO_2 hydrogenation with H_2 at 673 K is shown by the scanning transmission electron microscopy (STEM) image in Figure 2-8 below (Yan, Binhang et al., 2019). This highlights that the preparation and characterization of bimetallic alloy catalysts, particularly confirming true alloy formation at the nanoscale, is non-trivial.

In contrast, Raseale et al. (2021) prepared oxidic precursor Fe-Ni nanoparticles in the inverse spinel structure, generalized by the formula AB_2O_4. In this structure the A site has a valency of 2+ and the B site has a valency of 3+, thus different Fe:Ni compositions were synthesized using substitution of the A site of nickel ferrite, $NiFe_2O_4$, with ferrous oxide to achieve nanoparticles with the generalized formula $(Ni_xFe_{1-x})Fe_2O_4$. The close association of Fe and Ni in the precursor nanoparticles increases

the chances of alloy formation when the particles are reduced compared to a technique such as co-impregnation.

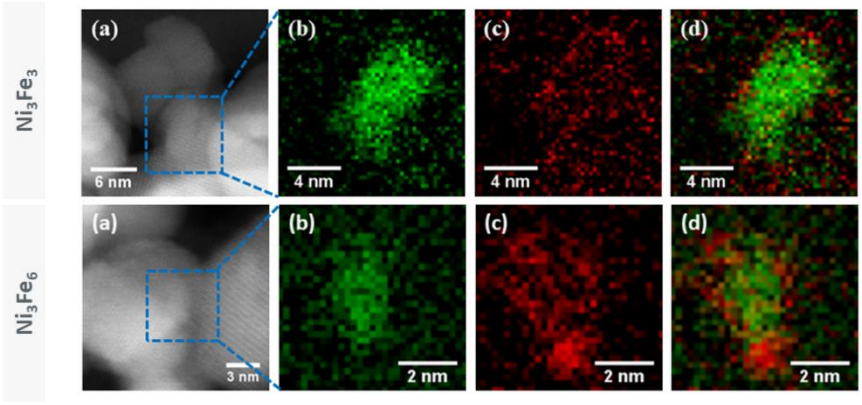

Figure 2-8: ADF-STEM images and corresponding EELS elemental maps of the spent Ni_3Fe_3/ZrO_2 and Ni_3Fe_6/ZrO_2 samples: ADF-STEM (a), Ni map (green,b), Fe map (red, c), and mixed maps (d) (Yan, Binhang et al., 2019).

The homogenous, intimate mixing of Fe and Ni in the precursor particles was confirmed by STEM energy-dispersive X-ray spectroscopy (EDX) mapping as shown in Figure 2-9. Where the atomic ratio of Fe to Ni was less than 1:2 (Figure 2-9A, Fe:Ni = 1:1), some Ni was not incorporated into the nanoparticles and formed needle-like structures. This is in good agreement with the DFT study by Ko, Kim and Han (2016) presented earlier (see Figure 2-6) which showed that bimetallic alloys where Ni is the host atom and Fe is the solute atom are not preferred to the surface segregation of solute atoms.

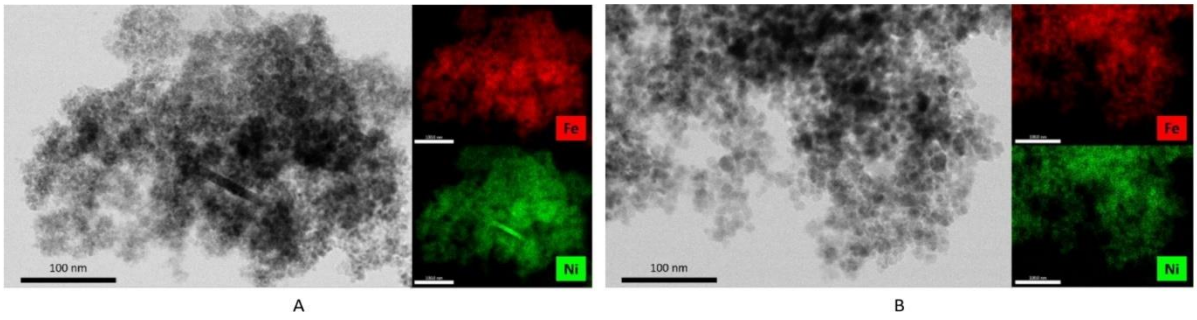

Figure 2-9: TEM images with STEM-EDX elemental mapping of oxidic unsupported Fe1Ni1 (A) Fe3Ni1 (B) (Raseale et al., 2021).

Further *in-situ* XRD data on the catalysts developed by Raseale et al. (2021) confirmed that, upon reduction of the precursor particles, a mixture of bcc and fcc Fe-Ni phases were formed in good agreement with the phase diagram presented in Figure 2-7. Rietveld Refinement confirmed that the iron richer catalysts formed a predominantly bcc structure while the nickel richer catalysts formed a predominantly fcc structure. This further supported that an Fe-Ni alloy was formed as opposed to distinct and segregated monometallic phases which would not behave in this way. It is possible that the bcc phase was enriched with Fe and the fcc phase was enriched with Ni, but this could not be concluded based on the results available (Raseale et al., 2021).

The reduction of spinel $NiFe_2O_4$ nanoribbons was also investigated by Jing et al. (2016). Formation of a nano-alloy upon reduction was supported by XRD analysis and HRTEM analysis. A similar trend to Raseale et al. (2021) in the phase configuration with temperature was observed. From around 300°C, the oxidic spinel precursor particles began deoxidizing first into the bcc Fe-Ni alloy and were then transformed to the fcc phase. Above 400°C no oxidic phases were observed, and the sample was described as a mixture of bcc and fcc alloys, and above 600°C only the fcc alloy phase was present.

2.2.3 Catalytic performance of Fe-Ni systems

Yan, Binhang et al. (2019) tested Ni_3Fe_x/ZrO_2 catalysts of varying Fe content for CO_2 activation in flow reactor experiments under CO_2 hydrogenation conditions (400 °C, H_2:CO_2 = 2:1). It was found that, compared to pure Ni, a low Fe content initially promoted hydrogenation activity in the catalyst (87% CH_4 selectivity) but the selectivity for CO over CH_4 increased with increasing Fe content. The catalyst with the highest Fe content, Ni_3Fe_9/ZrO_2, had a CO selectivity of 96%. Density functional theory (DFT) calculations were conducted to understand this trend. The Ni-FeO_x interface was proposed to be the active site for RWGS. It was proposed that the weak binding energy between Ni-FeO_x and CO causes gaseous CO to desorb from the surface instead of being hydrogenated. CO* binding energy with phases present on the catalyst surface is therefore a predictor for CO:CH_4 selectivity (Yan, Binhang et al., 2019). In a previous publication, the same research group proposed the Ni-FeO_x interfacial sites to be responsible for the role of increased Fe content in improved ethylene selectivity under CO_2-ODH conditions (Yan, B. et al., 2018).

In the study by Raseale et al. (2021), a clear distinction in the CO_2 activation potential between the different alloy allotropes (bcc and fcc) was observed. This was studied in *in-situ* temperature-programmed CO_2 activation experiments in which the reduced catalyst samples were exposed to a dilute stream of CO_2 while temperature was increased linearly. At elevated temperatures the bcc alloy phase was re-oxidized back to the $(Ni_xFe_{1-x})Fe_2O_4$ spinel structure while the fcc structure remained unchanged. It was concluded that independent of Fe content, the bcc allotrope of Fe_xNi_y promotes the dissociation of CO_2 to yield gaseous CO, while the fcc allotrope of the alloy is inert (Raseale et al., 2021). Figure 2-10 shows the top view in-situ of both the reduction and CO_2 activation, and CO evolution as function of temperature in the CO_2 activation step, for an iron richer sample (Fe5N1, A) and a nickel richer sample (Fe1Ni1, B). Increased CO formation is observed over than the iron-richer sample which was associated with the increased proportion of the bcc allotrope in the reduced sample. It is undetermined whether the introduction of H_2 to this system will remove O* as water, following the redox mechanism for RWGS; hydrogenate CO_2* to follow the associative mechanism for RWGS; or promote the hydrogenation of CO_2 to CH_4.

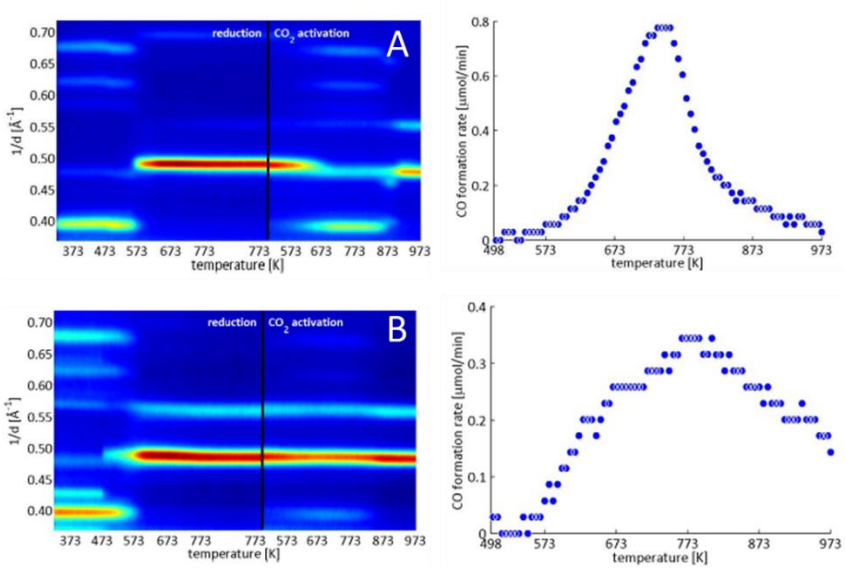

Figure 2-10: Top view of in-situ XRD study of reduction and CO_2 activation studies (left) and CO evolution as function of temperature in the CO_2 activation step (right) of KIT-6 supported Fe5N1 (A) and Fe1Ni1 (B). From Raseale et al. (2021).

The Fe_xNi_y catalysts were tested under CO_2-ODH reaction conditions. When supported on the reducible metal oxide (CrO_x), an increase in Fe content supported CO_2-ODH activity. An increase in Ni content in the catalyst increased the conversion of both ethane and CO_2, but decreased the selectivity to ethylene in favor of CO. The increase in CO selectivity was explained by the dry reforming and reverse Boudouard pathways with no reference to RWGS made. XRD analysis of the spent catalysts revealed a significant increase in the crystallite size compared to the reduced catalyst for the Fe-rich catalyst (Raseale et al., 2021). Additionally in this work, two support materials were tested, namely ZrO_x and CrO_x overlayer surfaces representing a non-reducible and reducible material, respectively. Little to no activity was observed on both bare and Fe_xNi_y-containing ZrO_x under CO_2-ODH reaction conditions. In contrast, bare CrO_x showed an initial, low conversion on ethane and CO_2 which decreased linearly with time on stream (TOS) to 0%.

2.3 SYNTHESIS ROUTES FOR METAL OXIDE-SUPPORTED IRON-NICKEL ALLOY SYSTEMS

Effective RWGS catalysts consists of highly dispersed nanoparticles on a metal-oxide support. This is important to maximize the interfacial area between the active metal and the support, as both materials participate in the reaction (Porosoff, Yan & Chen, 2016). The MOx-supported Fe_xNi_y catalysts prepared by Raseale et al. (2021) made use of novel approaches for the synthesis of $(Ni_xFe_{1-x})Fe_2O_4$ nanoparticles and bespoke $MOx@Al_2O_3$ support materials which will be discussed below.

2.3.1 MOx overlayer preparation

The preparation of $MOx@Al_2O_3$ supports has been described by Prieto et al. (2015) in response to the discrepancies observed in the performance of Co-based FTS. Different metal oxides studied as support materials have a great variability in inherent bulk physical properties, such as pore size and volume. As a result, it cannot be known with certainty whether discrepancies in catalytic performance are because of the surface composition of a catalyst support or because of its physical and textural properties. The pore geometry of a support influences the rate of intraparticle diffusion of reactants and products, which in turn influences catalytic activity and selectivity. The available surface area of a support also influences the metal dispersion which can influence activity and selectivity in size-dependent reactions (Prieto et al., 2015).

$MOx@Al_2O_3$ denotes the overlayer coverage of a common, high surface are γ-Al_2O_3 carrier by a metal oxide, MOx. To target monolayer coverage of γ-Al_2O_3 by the MOx, incipient wetness impregnation of the Al_2O_3 carrier is performed under vacuum targeting an atomic loading of 4.0 − 5.0 atoms/nm^2 (Prieto et al., 2015).

The catalysts developed by Raseale (2022) also employ this technique for the preparation of $MOx@Al_2O_3$ overlayers with comparable textural properties. Table 2-1 shows a comparison of the textural properties of the prepared $MOx@Al_2O_3$ materials to the bare γ-Al_2O_3. The pore geometry of the underlying γ-Al_2O_3 carrier is maintained while the surface is modified by the MOx overlayer. The minor reduction in the specific surface area and pore volume of the $MOx@Al_2O_3$ supports compared to the underlying γ-Al_2O_3 carrier was attributed to the partial filling of smaller γ-Al_2O_3 mesopores. The absence of bulk MOx crystallites was confirmed via XRD.

Table 2-1: Physicochemical Properties of $MOx@Al_2O_3$ support materials. Reproduced from Raseale (2022)

	Composition		Textural properties			Acid-base character
support	M (wt.%)	δ (atoms/nm^2)	BET (m^2/g)	V_p (cm^3/g)	PD (nm)	η (eV)
Al_2O_3			151	0.50	9	2.51
$CrO_x@Al_2O_3$	7.5	6.2	128	0.44	11	2.27
$SmO_x@Al_2O_3$	18.9	6.2	123	0.33	9	2.38
$TiO_x@Al_2O_3$	7.9	1.7	141	0.44	9	2.46
$GaO_x@Al_2O_3$	8.3	5.2	133	0.44	9	2.48
$ZrOx@Al_2O_3$	11.5	5.7	144	0.43	9	2.49
$VO_x@Al_2O_3$	9.9	8.6	111	0.40	8	2.60

M = metallic loading, δ = surface coverage of the Al_2O_3 surface with M atoms, BET = specific surface area, V_p = total specific pore volume, PD = pore diameter, η = Energy of intramolecular charge transfer (IMCT) band of adsorbed alizarin.

Figure 2-11 shows a comparison of the H_2 temperature programmed reaction (TPR) profiles (A), diffuse reflectance (DR-UV/Vis) spectra after saturation adsorption of alizarine (B), and NH_3 temperature

programmed desorption (TPD) profiles (C) for the prepared $MOx@Al_2O_3$ supports, showing how the chemical and electronic properties of the underlying Al_2O_3 carrier is altered. Figure 2-11A shows that of the materials prepared, only $VOx@Al_2O_3$ and $CrOx@Al_2O_3$ show reflexes indicative of reduction within the temperature range studied, thus these were termed reducible overlayers with $CrOx@Al_2O_3$ being the most readily reducible at 275 °C. The DR-UV/Vis spectra collected for the overlayer materials (see Figure 2-11B) suggest the following order of relative surface Lewis acid strength: $VOx@Al_2O_3$ > $CrOx@Al_2O_3$ > γ-Al_2O_3 > $ZrOx@Al_2O_3$ > $GaOx@Al_2O_3$ > $TiOx@Al_2O_3$ > $SmOx@Al_2O_3$. This is in good agreement with the order of acid strength obtained via NH_3-TPD (see Figure 2-11C) except for the order of $GaOx@Al_2O_3$ and $ZrOx@Al_2O_3$.

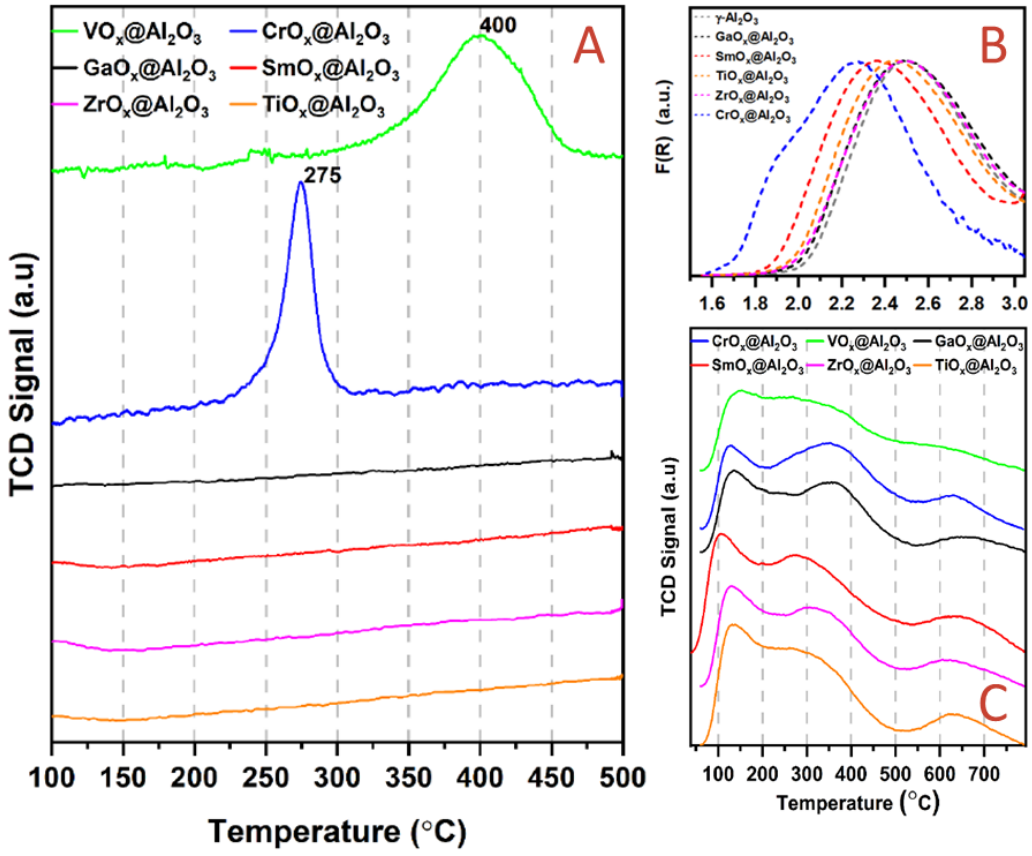

Figure 2-11: H_2-TPR profiles (A), DR-UV/Vis spectra after saturation adsorption of alizarine (B), and NH_3-TPD profiles (C) of various $MOx@Al_2O_3$ supports (Raseale, 2022).

2.3.2 Nanoparticle synthesis

Conventional synthesis methods for the preparation of highly dispersed catalytically active bimetallic particles onto a support include co-impregnation, successive impregnation, or co-precipitation. While advantages of these methods include their ease and economic viability, the resultant materials often have a non-uniform size distribution and/or metallic distribution which may impact catalytic performance evaluation (Xie, Winter & Chen, 2021). Moreover, for these approaches, post-treatment steps such as solvent removal and high temperature calcination may be needed which may

compromise the size, position, morphology and/or homogeneity of the clusters formed (Munnik, de Jongh & de Jong, 2015). This, in addition to the increased chances of alloy formation with close association of the constituent metals discussed above, motivates for the synthesis of precursor nanoparticles which can be anchored onto the support.

The synthesis of nanoparticles with a controlled size and shape and with a narrow size distribution is challenging. The use of surfactants, such as in the reverse micelles technique, allows for the controlled synthesis of well-defined nanoparticles, however the nanoparticles are usually poorly crystalline with low yields. While heat treatment can be used to improve the crystallinity of prepared particles, this has adverse effects on the physical properties of the nanoparticles. Moreover, a large amount of solvent is required to prevent agglomeration. Residual surfactant may be challenging to remove and, as a bulky organic impurity which reduces accessibility to the catalytic active surface, has detrimental effects on catalytic performance (Wolf, Fischer & Claeys, 2018).

Nanometer-scale spinel ferrites, MFe_2O_4 (M = Mn, Co, Ni, etc.) are important magnetic materials widely used for studies of nanomagnetism with technological applications across a wide range of fields such as information storage, colour imaging, catalysis, biomolecule separation and drug delivery. MFe_2O_4 has been shown to be prepared via surfactant-free solvothermal synthesis route for the controlled preparation of monodisperse nanoparticles. In this approach, precursors such as metal acetates and alkoxides are decomposed in a solvent such as water, ethylene glycol or alcohols under moderate to high pressures and temperatures to produce nanoparticles. Benzyl alcohol can act as both a solvent and a ligand during the synthesis, preventing agglomeration (Yáñez-Vilar et al., 2009).

Synthesis parameters which influence the crystallite size, size distribution and shape include temperature, pressure, reaction time, precursor mass, ammonia addition and total reaction volume. The particle size of highly monodisperse spinel Co_3O_4 nanoparticles prepared via surfactant-free solvothermal synthesis in benzyl alcohol was found to be controllable by the quantity of ammonium hydroxide added. In addition, larger crystallite sizes were obtained through an increase in the reaction temperature and by an increase in the concentration of the precursor salts. This synthesis route was scaled up to yield up to 1 g of nanoparticles, with sufficient mixing of the reaction mixture identified as a critical requirement for scale up (Wolf, Fischer & Claeys, 2018). A similar synthesis route has been successfully employed for the preparation of substituted nickel ferrite nanoparticles, $(Ni_xFe_{1-x})Fe_2O_4$ with (Fe:Ni = 1, 3 and 5) (Raseale et al., 2021).

3. PROPOSED WORK

This chapter discusses the overall objectives and scope of the present work.

3.1 OBJECTIVES

The goal of the present study is to further study the materials prepared by Raseale et al. (2021) in the RWGS. The effect of iron content in an iron-nickel alloy phase and the effect of varying MOx support materials on catalytic activity, selectivity, and stability is of interest. The objectives of this research are summarized as:

- Prepare batches of $(Ni_xFe_{1-x})Fe_2O_4$ oxidic iron-nickel nanoparticles of varying Fe content (Fe:Ni = 3, 5 and 7 as well as pure iron oxide, $FeFe_2O_4$) via the benzyl alcohol route
- Prepare MOx overlayer support materials of varying reducibility
- Deposit nanoparticles onto the support materials, as well as onto SiO_2 (inert support)
- Evaluate the prepared materials under RWGS conditions

3.2 HYPOTHESES AND KEY QUESTIONS

The following is hypothesized based on the literature reviewed and the objectives of this research.

3.2.1 H1 - RWGS performance vs alloy composition

Activity and selectivity in the RWGS over Fe_xNi_y alloy catalysts will increase with an increase in Fe content. Bulk Fe-Ni phase diagrams indicate that at elevated temperatures, an increase in Fe improves the stability of the bcc allotrope of the Fe-Ni alloy. Under RWGS reaction conditions, CO_2 is activated on the bcc surface of an Fe_xNi_y alloy. This occurs via a Mars van Krevelen – type mechanism in which the bcc phase is oxidized by O* forming a spinel oxide structure. The bcc phase is regenerated via the reductive pressure of H*, completing the catalytic cycle

- How does Fe content affect catalyst activity?
- Can bulk phase diagrams be used to predict alloy formation at the nanoscale?
- How does temperature effect the stability of the bcc phase?
- What factors influence successful alloy formation at the nanoscale?
- What mechanism is followed for RWGS over supported Fe_xNi_y catalysts?
- Does the bcc phase promote methanation under RWGS conditions?

3.2.2 H2 – RWGS performance vs MOx overlayer material

Catalytic performance will be improved when oxidic Fe_xNi_y precursors are deposited on supports of increasing reducibility. The support participates in the RWGS mechanism through the provision of a reactive O* surface sites on which CO_2 is reduced to CO

- To what extent does the reducibility of the catalyst support material play a role in activity?
- How is CO and CH_4 selectivity affected by the reducibility of the support?

3.3 SCOPE

The aim of the synthesis stage was to obtain substituted nickel ferrite nanoparticles of varying composition with comparable size, in the 10 – 20 nm range. A development and/or understanding of the benzyl alcohol method and/or synthesis conditions for different target Fe:Ni ratios was not within the scope of this project. The lower bound of Fe:Ni atomic composition that can be studied is Fe:Ni = 2:1, as this is the maximum amount of Ni that can be accommodated in the spinel structure, $(Ni_xFe_{1-x})Fe_2O_4$. At Ni contents above this, upon reduction, Ni fails to be incorporated into the nanoalloy structure (Raseale et al., 2021). Characterizations will be carried out on the unsupported nanoparticles to confirm the crystalline phases present, the particle size and morphology, the metallic composition, and the metallic distribution in the nanoparticles.

It is the goal of overlayer synthesis to obtain $MOx@Al_2O_3$ carrier materials with comparable textural properties. Characterizations will be carried out to confirm that no bulk MOx is present on the as-prepared samples, and that the textural properties (pore size and volume) are comparable. The electronic and chemical properties of the prepared overlayers such as reducibility and acid/base properties were investigated thoroughly by Raseale (2022) and will be referenced in this work.

Catalyst testing was limited to one set of conditions at ambient pressure, 600 °C and at a stoichiometric H_2:CO_2 ratio. A suitable space velocity was determined at which the catalysts were operating below thermodynamic equilibrium but at a high enough conversion that the trends between samples could be reliably established (See Appendix B: Preliminary testing to determine testing space velocity).

3.4 SUSTAINABLE DEVELOPMENT GOALS

This project is linked to the United Nation's sustainable development goal (SDG) 13, to ensure access to affordable, reliable, sustainable, and modern energy for all. A better understanding of RWGS catalysis will accelerate the development of reliable PtL pathways with the ambition to replace a portion of today's oil-derived products with synthetic liquid fuels. A considerable benefit of this approach to sustainable energy over others is that it leverages the well-established FTS process, as well as pre-existing infrastructure for the transport, storage, and consumption of energy dense liquid fuels. As outlined above, oil accounts for 40.8% of the world's total energy consumption and 34.1% of CO_2 emissions from fossil fuel combustion. The affordability and sustainability of this pathway is, however, dependent on the availability of affordable H_2 produced from renewable energy.

4. EXPERIMENTAL METHODOLOGY

This chapter discusses the detailed experimental approach taken for the synthesis, characterization, and testing of the metal oxide-supported iron-nickel alloy catalysts.

4.1 CATALYST PREPARATION

Four batches of oxidic precursor particles were prepared and deposited onto two MOx overlayer materials, as well as onto SiO_2. This resulted in a library of 12 supported metal catalysts and three bare supports. All chemicals were used as received and a full list of chemicals used is available in Appendix C.

4.1.1 Nanoparticle synthesis

Four batches of substituted nickel ferrite $(Ni_xFe_{1-x})Fe_2O_4$ inverse spinel precursor nanoparticles were synthesized using the surfactant-free hydrothermal treatment of Fe (II) and Ni (II) acetates in benzyl alcohol in the presence of ammonium hydroxide. The targeted compositions were Fe:Ni = 3, 5 and 7, as well as iron oxide.

Iron(II) acetate (Sigma-Aldrich, ≥ 95.00%) and Nickel(II) acetate tetrahydrate (Sigma-Aldrich, ≥ 98.00%) metal precursors were used. Table 4-1 summarizes reaction conditions and reagent quantities used for the synthesis. Please see Appendix A for a sample calculation of how the required precursor quantities for the respective target ratios were determined. 4.1 g total precursor in the targeted atomic ratio was dissolved in 155 ml benzyl alcohol (Sigma-Aldrich, ≥ 99.90%) and stirred at 500 rpm for 2 hours under magnetic stirring in a PTFE autoclave insert. Ammonium hydroxide (Kimix, 25.00 wt.%) was added dropwise to the metal solution, resulting in a black emulsion. The emulsion was transferred to an autoclave (in-house design) and heated under magnetic stirring and autogenous pressure at 200 °C for 12 hours. The mixture was cooled to room temperature and washed several times – first with isopropanol (Kimix, ≥ 99.98%), followed by ethanol (Kimix, ≥ 99.30%), and then several acetone (Kimix, ≥ 99.30%) washes.

Table 4-1: Summary of reaction conditions and reagent quantities for nanoparticle synthesis.

Sample	Temperature (°C)	Time (h)	Fe (II) acetate (g)	Ni (II) acetate tetrahydrate (g)	Benzyl alcohol (ml)	Ammonium hydroxide (ml)
Fe3Ni	200	12	2.66	1.44	155	95
Fe5Ni	200	12	2.78	1.32	155	95
Fe7Ni	200	12	3.19	0.91	155	30
Fe100	200	12	4.1	-	190	-

The nanoparticles were named Fe3Ni, Fe5Ni, Fe7Ni and Fe100 according to their respective target Fe:Ni atomic ratios.

4.1.2 Overlayer synthesis

Reducibility of a metal oxide support is expected to have a significant effect on RWGS activity and selectivity with reference to the reaction mechanisms presented in Chapter 2.1.2 above. This was investigated by preparing two MOx overlayer materials of varying reducibility, namely $CrOx@Al_2O_3$ and $GaOx@Al_2O_3$, representing a readily reducible and an irreducible material, respectively.

The $MOx@Al_2O_3$ overlayer materials were prepared as described by Prieto et al. (2015) and Raseale et al. (2021). Incipient wetness impregnation was used to disperse metal oxide overlayers onto a common, large-surface area (151 m^2/g) γ-Al_2O_3 carrier material (Puralox SCCa 5-150, SASOL South Africa). For each synthesis, 5 g of γ-Al_2O_3 was calcined in a furnace under static air at 723 K overnight and then immediately transferred to a Schlenk flask which allowed storage under vacuum. The γ-Al_2O_3 was subjected to thermal treatment under vacuum at 553 K for 3 h to remove surface adsorbed water. The sample was cooled to room temperature, whereafter Ar was added to the flask slowly to maintain an inert, dry environment.

Metal precursor solutions of 2.73 M chromium (III) nitrate nonahydrate (Sigma-Aldrich, ≥ 99.90%) and 2.73 M gallium (III) nitrate hydrate (Sigma-Aldrich, ≥ 99.90%) in deionized water were prepared. These concentrations correspond to the target surface specific metal loading sufficient to obtain nominal monolayer coverage on the surface on the γ-Al_2O_3 carrier at 5 atoms/nm^2. 2.3 ml of metal precursor solution, corresponding to the total mesopore volume of the γ-Al_2O_3, was added to the sample under Ar.

The samples were dried at 343 K for 12 hours under static air and calcined in a tubular furnace at 873 K for 4 hours under air flow. The obtained overlayers were termed $CrOx@Al_2O_3$ and $GaOx@Al_2O_3$, respectively.

4.1.3 Supporting of nanoparticles

The precursor nanoparticles were dispersed on each carrier via a sonication method described by Fischer, van Steen and Claeys (2013) at a target metallic loading of 10 wt.-%. 0.15 g of the nanoparticles was re-dispersed in 1000 ml ethanol (Kimix, ≥ 99.30%) via ultrasonication at 100 % power setting in a UBM22 ultrasonic bath for 4 hours. Subsequently, 0.99g AEROSIL® 200 hydrophilic fumed silica (AEROSIL, > 99.8 wt.%) or the respective MOx overlayer support was added and the mixture was allowed to sonicate for a further 1 hour. Ethanol was then evaporated from the suspension at 460 mbar with a round-bottom 1000 ml Büchi flask in a rotary evaporator.

4.2 CATALYST CHARACTERIZATION

4.2.1 Transmission electron microscopy (TEM)

TEM was used to obtain particle size distributions for the nanoparticles produced. Carbon coated copper TEM grids were prepared for each sample considered. Dried samples were redispersed in absolute ethanol and sonicated in an ultrasonic bath to obtain a well-mixed particle suspension, which was then dropped onto the grids. Once dried, the grids were ready for analysis. The UCT Electron Microscope Unit has two transmission electron microscopes which were used for imaging depending on their availability – either a FEI Tecnai F20 with a 200 kV field emission gun or a FEI T20 with a 200 kV LaB_6 filament. Open-source ImageJ software was used to measure individual particle sizes from the obtained micrographs. The particle size distribution, mean particle size and standard deviation was calculated.

4.2.2 Ex situ powder X-ray diffraction (PXRD)

PXRD was used to identify the crystalline phases present in the unsupported nanoparticles, as well as the supported nanoparticles, passivated reduced catalysts, and passivated spent catalysts. A Bruker D8 Advance X-ray diffractometer equipped with a position sensitive LynxEye E 1D mode detector and a cobalt source (λ = 1.78897 Å) operated at 35 kV and 40 mA was used. All samples were scanned over a 2θ range of 20 – 120 ° using a size step and scan rate of 0.043 ° and 0.75 s respectively, leading to a total scan time of 29 minutes and 50 seconds. The obtained diffractograms were compared with reference data files reported in the ICDD PDF-4 database.

Rietveld refinement was conducted using the TOPAS 5.0 software to extract weight fractions and average crystallite sizes of the identified phases of the collected diffractograms.

4.2.3 Inductively coupled plasma optical emission spectroscopy (ICP-OES)

The Fe, Ni and O content of the unsupported nanoparticles and the metallic loading of the supported samples was determined by ICP-OES measurements in a Varian OES 730 spectrometer. The samples were prepared by acid digestion in 4 ml HNO_3, 2 ml H_2SO_4, 2 ml aqua regia and 2 ml HF in a MARS-5 microwave digester at 180 °C for 40 minutes.

4.2.4 Scanning electron microscopy (SEM) and energy dispersive X-ray (EDX) elemental mapping

SEM-EDX elemental mapping was used to confirm the homogenous distribution and intimate mixing of metals within the precursor particles. Samples were prepared by depositing powdered sample onto a holey film carbon-coated copper grid. SEM-EDX elemental maps were collected using a high-resolution field emission Nova NanoSEM 230 (FEI) equipped with high resolution in-lens secondary, low voltage backscatter, STEM, as well as Oxford X-Max silicon drift EDX detectors.

4.2.5 Raman spectroscopy

Raman spectroscopy was conducted on the prepared MOx overlayers to compare the surface of the carriers to their respective bulk oxides. The Raman spectra for selected spent catalysts were also collected to detect potential carbon deposition or the sintering of MOx to form bulk crystallites. Raman spectra were measured in an inVia Raman microscope (Renishaw, UK) in the range from 1100 to 100 cm^{-1} using a 532 nm green laser under ambient conditions at a laser power of 20 mW and an exposure time of 60 s.

4.2.6 Nitrogen physisorption analysis (BET)

The physical properties of the support materials were determined by analysis of nitrogen adsorption/desorption isotherms recorded using a Micromeritics TriStar II 3020 instrument. Approximately 500 mg of sample was degassed at 120 °C overnight. The Brunauer-Emmett-Teller (BET) method was used to determine specific surface areas from the adsorption branch of the isotherms. The Barrett-Joyner-Halenda (BJH) method was used to pore size distributions and average pore diameters from the desorption branch of the isotherms.

4.3 *IN-SITU* CHARACTERISATION

Catalyst reduction and CO_2 activation as a function of temperature was studied using *in-situ* XRD. An Anton Paar XRK900 reaction cell attached to a laboratory XRD (Bruker D8 Advance) was used and operated at 50 kV and 35 mA. The diffractometer was equipped with a molybdenum source and a position-sensitive detector (Bruker AXS Vantec).

4.3.1 In-situ XRD temperature-programmed reduction (TPR)

The powder samples (200 mg) were loaded into the XRK cell and were reduced using a mixture of 10 vol% H_2 in N_2 at a total flowrate of 50 mL/min. The temperature was increased to 500 °C, at a rate of 1 °C/min and held at 500 °C for 5 hours while XRD scans were collected every 5 min in the 2θ range of 15−29° at a step size of 0.017° and time per step of 0.2 s. The cell was then cooled to room temperature and flushed with N_2 for two hours to remove residual gaseous hydrogen.

4.3.2 In-situ XRD temperature-programmed CO_2 activation

For the CO_2 activation studies, the reduced sample was exposed to 5 vol% CO_2 in N_2 at a total flowrate of 100 mL/min. The temperature was increased from 50 °C to 700 °C at a rate of 1 °C/min while XRD scans were collected in the 2θ range of 15−29° at a step size of 0.017° and time per step of 0.2 s.

The XRK cell is known to have dead volumes within the cell, and outlet gas analysis would not yield sensible or reliable results during the *in-situ* XRD studies. Thus, the CO_2 activation experiments were

repeated in a dual quartz tube fixed-bed reactor setup to accurately measure CO formation as a function of temperature over the freshly reduced catalysts. These experiments are described below.

4.3.3 Temperature-programmed CO_2 activation in fixed bed reactor set-up

To probe CO_2 activation on the catalyst samples, the formation of CO as a function of temperature was recorded for the reduced samples in a fixed-bed reactor setup (See Figure 4-1 and Figure 4-2 below). Only one catalyst sample was loaded and evaluated at a time to ensure good time resolution in the results. The second tube of the dual quartz tube setup was filled with SiC, and the product gas from this tube was not analyzed.

The samples were loaded and reduced as described in section 4.4.2 below. After reduction, the samples were cooled to 50 °C under flowing Ar. Once 50 °C was reached, the inlet gas mixture (50 mL/min 1 vol% CO_2 in Ar) was measured in a bypass analysis to obtain baseline values for the subsequent data analysis as detailed below. Once the bypass was stable the temperature was increased linearly from 50 °C to 700 °C at a rate of 5 °C/min while the outlet gas was analyzed continuously. After CO_2 activation, the catalysts were cooled to room temperature under flowing Ar and passivated in 1% O_2 in N_2 for 1 hour, whereafter they were removed from the quartz tube for spent catalyst characterization by TEM, XRD and Raman as outlined above.

Product gas analysis was conducted in a Hiden HPR-20 R&D (Hiden Analytical, United Kingdom) mass spectrometer (MS), which provides better time resolution than the thermal conductivity detector (TCD) used during catalytic performance evaluation. The MS was equipped with a Quartz Inert Capillary and two detectors: the Faraday Cup and Secondary Electron Multiplier. Control of the instrument and data analysis were performed using Massoft Professional software. The operating principle of the MS is that components in the gas mixture being analyzed are ionized by electron impact to form positive ions. Each molecule has a characteristic fragmentation pattern, which is tabulated as intensity versus mass for different molecules. To quantify the components in a gas mixture, theoretical relative sensitivity factors (RSF) are available per molecule.

During the CO_2 activation experiments, MS readings for the masses 28, 40 and 44 were taken continuously. Masses 40 and 44 correspond to the gasses Ar and CO_2 respectively, while mass 28 has contributions from both CO and CO_2. To deconvolute the signal at mass 28 to calculate CO formation rate, the contribution to mass 28 from CO_2 was calculated in reference to the bypass analysis. The contribution to mass 28 from CO_2 was then subtracted from the mass 28 signal, yielding the contribution from CO, which was converted to a molar formation rate using RSF values.

4.4 CATALYST TESTING

4.4.1 Test unit and reactor set-up

A flow diagram for the test unit used for catalyst testing is shown in Figure 4-1 below. The gasses used for testing are 50% CO_2 in Ar (AFROX), Ar and H_2 (both Air Products, 99.999%) and are fed into the test unit using three Brooks Instruments mass flow controllers (MFCs). The MFCs were calibrated before use for each gas. The gasses are combined after the MFCs, whereafter the gas is directed to either the dual reactor system or bypass line via a 3-way valve (3WV-4). In the former case, the gas flows through two capillary columns (Sigma Aldrich, 0.1 mm ID) of equal length to achieve and even split of the gas into each quartz reactor tube.

Figure 4-2 below illustrates a packed quartz tube reactor (Hilgenberg GmbH, Germany, L = 150 ± 0.5 mm, OD = 6.36 ± 0.3 mm, ID = 4 mm, S = 1.175 ± 0.2 mm). The figure shows how the catalyst bed is tightly packed in the middle of the tube, corresponding to the isothermal zone of the stainless-steel mounting block with four heating cartridges (Energy Solutions South Africa Pty Ltd, L = 100 mm, 40 mm cold end, D = 8 mm, 200 W, 230 V) and a thermocouple located in the center of the block. The catalyst bed is prevented from moving by two quartz wool plugs. SiC is packed on either side of the catalyst bed to assist with preheating of the gasses and to keep the catalyst bed in the isothermal zone.

The outlet gasses from the reactor were maintained at 80 °C to ensure the products remain gaseous until water was condensed in dedicated traps at room temperature. After the water trap, the product gas from each reactor flows to an individual 3/2-way-solenoid valve (Bürkert)which is programmed to allow gas from one reactor at a time to be sent for analysis and to switch to the other reactor in each time interval. For all tests, gasses from reactor were analyzed for 1 hour, after which the positions of the solenoid valves were switched to allow analysis from the second reactor for 1 hour, and so on. While the gas from one reactor was being analyzed, the gas from the other was sent to a vent.

The bypass line was used to confirm the baseline inlet gas composition for each run before the gas was sent to the activated catalyst. Four two-way needle valves were installed in series on the bypass line to pressurize the bypass line to equal the pressure generated before the capillaries ahead of the two reactor tubes.

4.4.2 Generalized experimental procedure

The generalized experimental procedure can be summarized into four stages – catalyst activation, bypass analysis, catalyst testing and passivation. Each catalyst was activated in 50 mL/min H_2 while the temperature was raised from room temperature to 500 °C at a rate of 1 °C/min. The temperature was then held constant at 500 °C for five hours. After five hours, the reactors were flushed with Ar.

The reactors were held in Ar to protect the activated catalysts in an inert environment while the bypass analysis was conducted.

To conduct the bypass analysis, the gas flow was redirected from the reactors to the bypass line, and the target inlet gas composition was set using the MFCs. The composition was confirmed by an online micro gas chromatograph (Agilent 490 Micro GC) equipped with a thermal conductivity detector (GC-TCD), while the total gas flow was confirmed with a flowmeter. The inlet gas composition was analyzed until stable data from fifteen measurements was collected, as these results formed the basis of CO_2 conversion calculations. After the bypass analysis, the reactors were heated from 500 °C to the reaction temperature of 600 °C at a rate of 5 °C/min. Once the reaction temperature was reached, the inlet gasses were redirected from the bypass line to the reactors to start the catalyst testing.

During catalyst testing, the product gasses were measured using the GC-TCD. As described above, the product gas from one reactor at a time was sampled, with the sampled reactor switching every 1 hour by means of the automated solenoid valves. Once the desired testing time had elapsed, the reactors were cooled to room temperature under Ar flow. At room temperature, the catalysts were passivated in 1% O_2 in N_2 for 1 hour, whereafter they were removed from the quartz tube for spent catalyst characterization by TEM, XRD and Raman as outlined above.

4.4.3 Product analysis

Product gas analysis was completed by an online micro-GC equipped with two TCDs (Agilent 490 Micro GC), which detect gasses based on differences in thermal conductivity. Table 4-2 below contains the column details as well as the gasses detected and their order of elution in each column.

Table 4-2: GC-TCD configuration.

Agilent 490 Micro GC	Channel 1	Channel 2
Elutes in order of increasing retention time	H_2, CO	H_2, O_2, N_2, CO, CH_4, CO_2
Column	Molsieve 5Å	Agilent CP-COx
Column length	10 m	
Carrier gas	Ar	Ar
Injection time	100 ms	20 ms
Injector temperature	80 °C	100 °C
Column oven temperature	80 °C	100 °C
Column pressure	150 kPa	200 kPa
Stabilization time	5 s	5 s
Sampling time	35 s	30 s
Backflush	120 s	13 s

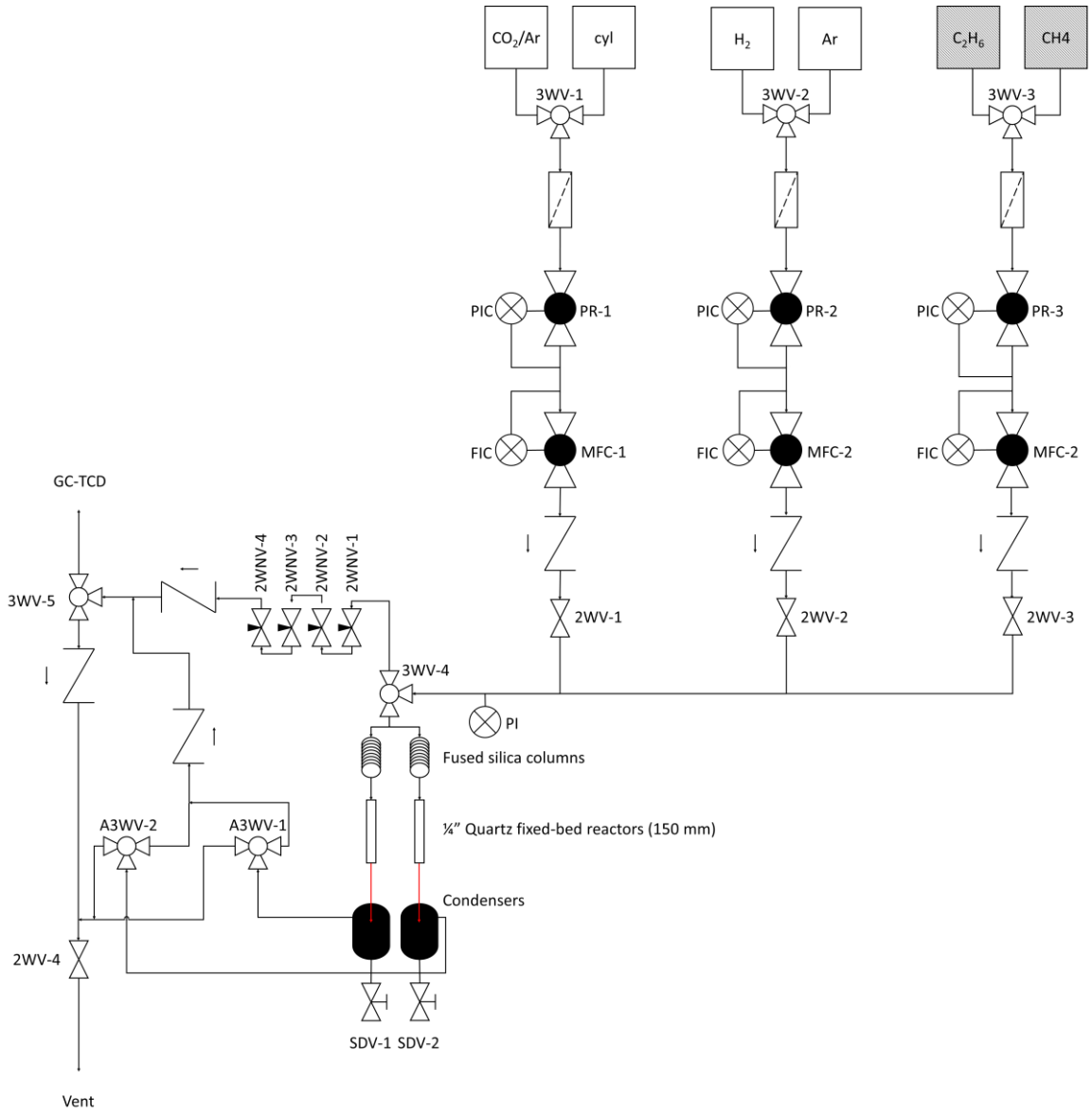

Figure 4-1: Process flow diagram of the test unit used for catalyst testing and CO_2 activation experiments. Lines in red are heated.

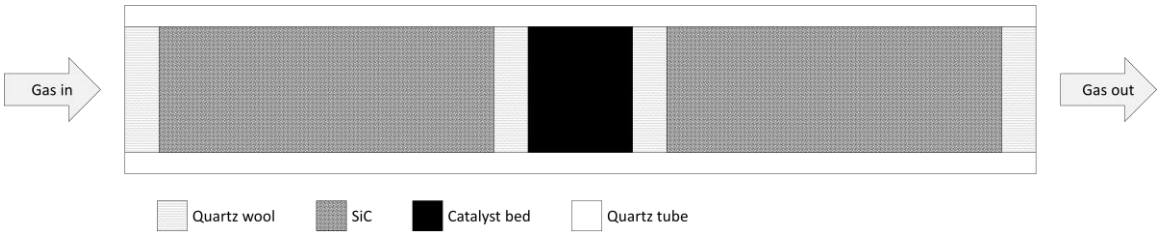

Figure 4-2: Illustration of the reactor used for catalyst testing.

The GC was calibrated using a gas mixture of known concentration, using Ar as an internal standard. From this calibration, response factors for each gas relative to Ar were determined using Equation 4-1 below. F_i is the response factor of gas *i* with respect to Ar, A_i and A_{Ar} are the measured peak areas of

gas *i* and Ar respectively and n_{Ar} and n_i are the molar gas flowrates of Ar and gas *i* respectively known from the calibration gas.

$$F_i = \frac{n_{Ar} A_i}{A_{Ar} n_i} \quad \text{Eq 4-1}$$

Using the response factors calculated above, the product gas composition is determined from the individual chromatograms taken over the course of the reaction using Equation 4-2 below. In this equation, $n_{i,out}$ is the molar flowrate of gas i in the product stream, $n_{AR,in}$ is the molar flowrate of the internal standard Ar determined in the bypass analysis, A_i is the peak area of gas *i* and $A_{Ar,out}$ is the peak area of Ar.

$$n_{i,out} = F_i \frac{n_{Ar,in} A_i}{A_{Ar,out}} \quad \text{Eq 4-2}$$

From the molar flowrates calculated above, catalytic performance was evaluated. Catalytic activity was expressed as CO_2 conversion (X_{CO_2}), calculated by Equation 4-3 below. This describes the amount of CO_2 converted during the reaction in relation to the CO_2 fed into the reactor.

$$X_{CO_2}(\%) = \frac{n_{CO_2,in} - n_{CO_2,out}}{n_{CO_2,in}} \cdot 100\% \quad \text{Eq 4-3}$$

The efficacy of the catalysts was expressed as CO selectivity (S_{CO}), calculated by Equation 4-4 below. This describes the amount of desired carbon product formed ($n_{CO,out}$) in relation to the total carbon products formed ($n_{CO,out} + n_{CH_4,out}$). This calculation is based on the experimental observation that CO and CH_4 are the only carbon products formed. This was validated for each data point by calculating an overall carbon balance using Equation 4-5 below which expresses the error in the total carbon exiting the system relative to the total carbon entering the system.

$$S_{CO}(\%) = \frac{n_{CO,out}}{n_{CO,out} + n_{CH_4,out}} \cdot 100\% \quad \text{Eq 4-4}$$

$$\%\ Error = \frac{n_{CO_2,out} + n_{CO,out} + n_{CH_4,out}}{n_{CO_2,in}} \quad \text{Eq 4-5}$$

4.4.4 In-situ RWGS testing

As a final experiment following catalyst characterization and catalytic performance evaluation, a selected sample ($Fe7Ni/SiO_2$) was studied in the *in-situ* XRD under RWGS conditions. The sample was loaded and reduced as described in section 4.3.1 above. The cell was flushed with Ar and heated to 600 °C at a heating rate of 5 °C/min, like in the fixed bed studies. The reduced sample was exposed to a dilute reaction mixture of 5% each H_2 and CO_2 in Ar (total flowrate = 100 mL/min) while XRD scans were collected every 5 min in the 2θ range of 15−29° at a step size of 0.017° and time per step of 0.2 s.

5. SYNTHESIS & CHARACTERISATION RESULTS

The characterization of as-prepared unsupported nanoparticles, bare MOx@Al_2O_3 overlayer supports and the supported metal catalysts are presented below.

5.1 UNSUPPORTED NANOPARTICLES

The characterizations discussed below demonstrate that nanoparticles of varying composition are successfully synthesized in the correct phase with satisfactory overlap in particle size distribution. Particularly, it is demonstrated that the benzyl alcohol method can be used to synthesize nanoparticles with a higher iron content than previously studied (i.e., Fe7Ni), as well as pure iron oxide in the spinel structure. The synthesis is also scaled up to produce a larger batch of nanoparticles than in the previous work by Raseale (2022) (4.1 g total acetate precursor vs 1.9 g).

5.1.1 ICP-OES

ICP-OES is performed to confirm the metallic composition of the unsupported nanoparticle. The raw results are a weight percentage of each analyte (Fe and Ni) in the sample were converted to atomic ratios using the atomic mass for each species. The achieved Fe:Ni ratio is computed for each bimetallic nanoparticle sample and summarized in Table 5-1 below, which shows that in all cases for the bimetallic nanoparticles, the actual Fe:Ni ratio was lower than the target. This suggests that some Fe is lost and not incorporated into the nanoparticles during synthesis.

Table 5-1 Comparison of target atomic Fe:Ni ratio of unsupported nanoparticles to achieved ratio derived from ICP-OES.

Sample	Total Fe (wt.%)	Total Ni (wt.%)	Target atomic Fe:Ni	Actual Fe:Ni
Fe3Ni	44.2	16.3	3	2.8
Fe5Ni	48.3	11.9	5	4.3
Fe7Ni	57.1	9.8	7	6.1

5.1.2 TEM

TEM is used to analyze the particle size, morphology, and size distribution of the as-prepared $(Ni_xFe_{1-x})Fe_2O_4$ nanoparticle. Figure 5-1 below shows TEM micrographs and particle size distributions of the four batches of as-prepared, unsupported nanoparticles. The number base average particle size, d_N, and standard deviation, σ_N, for each batch is shown in Table 5-2. This shows that there is a good amount of overlap in the particle size distribution across samples in the 10 – 20 nm range. In this range, the particle size effects are not predicted to be significant according to the classes of structure sensitivity-particle size relationships reported in literature (Van Santen, 2009).

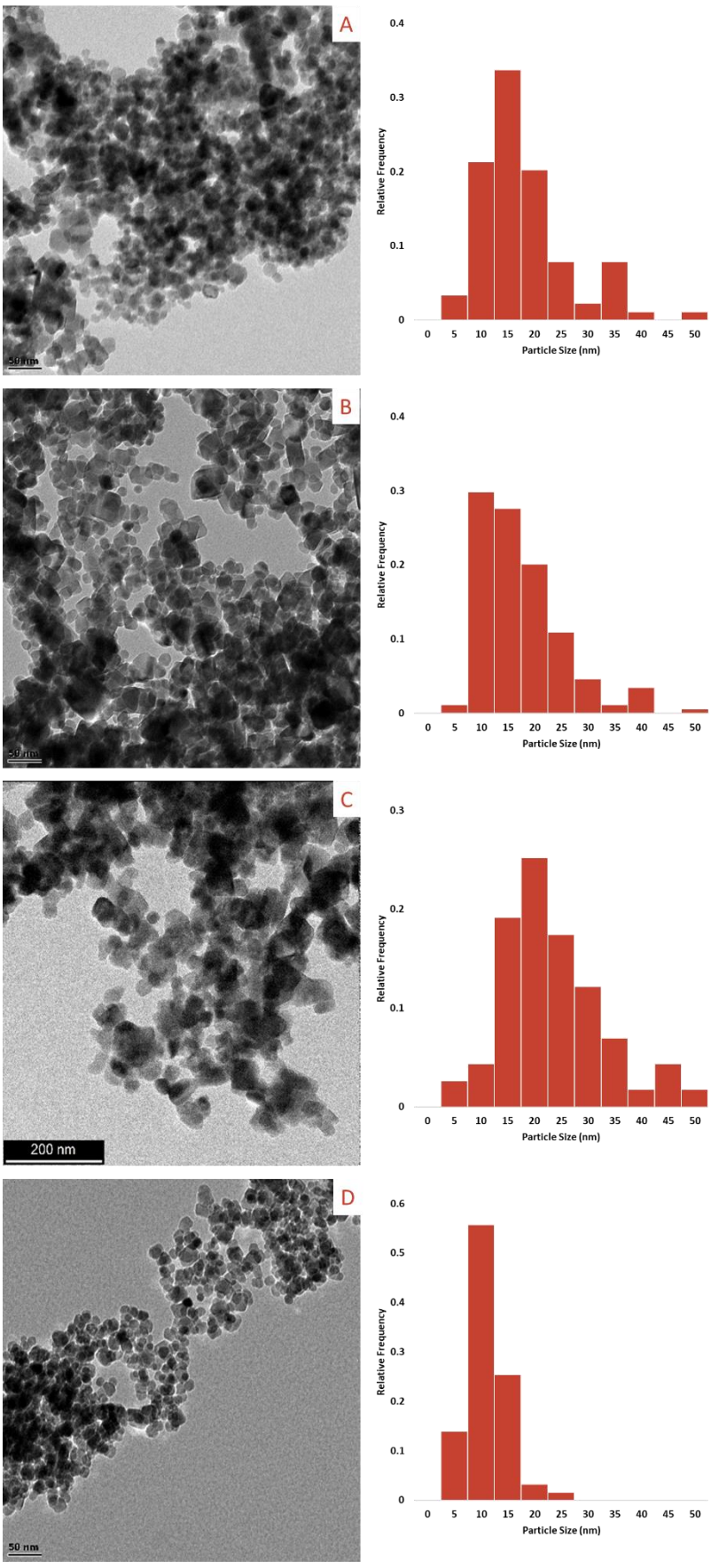

Figure 5-1: TEM Images and particle size distributions of the as-prepared nanoparticles. Fe3Ni (A), Fe5Ni (B), Fe7Ni (C) and Fe100 (D).

The achieved particle sizes are larger than the sub-10 nm particles achieved by Raseale (2022). This is probably the result of the greater mass of metal acetate precursor used with the aim of increasing the total nanoparticle yield, which influences mixing dynamics. The synthesis temperature, volume of ammonium hydroxide and mass of precursor can be optimized to produce better size control and/or distribution if required (Wolf, Fischer & Claeys, 2018).

Table 5-2 TEM number base average particle sizes, d_N, and standard deviations, σ_N, for the as prepared/unsupported nanoparticles.

	TEM		XRD
Sample	d_N (nm)	σ_N (nm)	d_V (nm)
Fe3Ni	20.7	9.3	13.7
Fe5Ni	20.3	8.5	19.8
Fe7Ni	27.8	13.1	27.6
Fe100	13.6	3.8	13.8

5.1.3 SEM-EDX

SEM images and SEM-EDX elemental maps (Fe, Ni and O) were taken of the as-prepared $(Ni_xFe_{1-x})Fe_2O_4$ nanoparticles at the varying atomic ratios. Figure 5-2 shows the SEM micrographs and elemental mapping for Fe3Ni. This confirms that there is in all cases homogenous, intimate mixing between iron and nickel in the precursor particles, increasing the chances of alloy formation upon reduction. The results for Fe5Ni and Fe7Ni show the same result and are available in Appendix D. Moreover, this confirms that no amorphous, or XRD-invisible phases with varying metal composition have formed or are present in the nanoparticle samples.

5.1.4 XRD

Figure 5-3A below shows the XRD patterns obtained for the as-prepared $(Ni_xFe_{1-x})Fe_2O_4$ nanoparticles. The only crystalline phase present in the samples is unambiguously the substituted nickel ferrite spinel structure, as seen with reference to $NiFe_2O_4$ (PDF-04-014-8286).

Figure 5-3B shows the same figure enlarged in the region of the most intense reflex for the $NiFe_2O_4$, which shows that the patterns are shifted to lower 2θ values compared to the reference with an increase in shift observed with iron content. This is expected with reference to Bragg's law (Equation 5-1 below) in which the incidence angle, θ, is inversely proportional to the spacing of the crystal layers, d. Because Fe has a lower atomic radius than Ni (126 pm and 163 pm respectively), as the iron content of the nanoparticles is increased, the spacing of the crystal layers is decreased. As a result, the same reflexes are observed at higher incident angles.

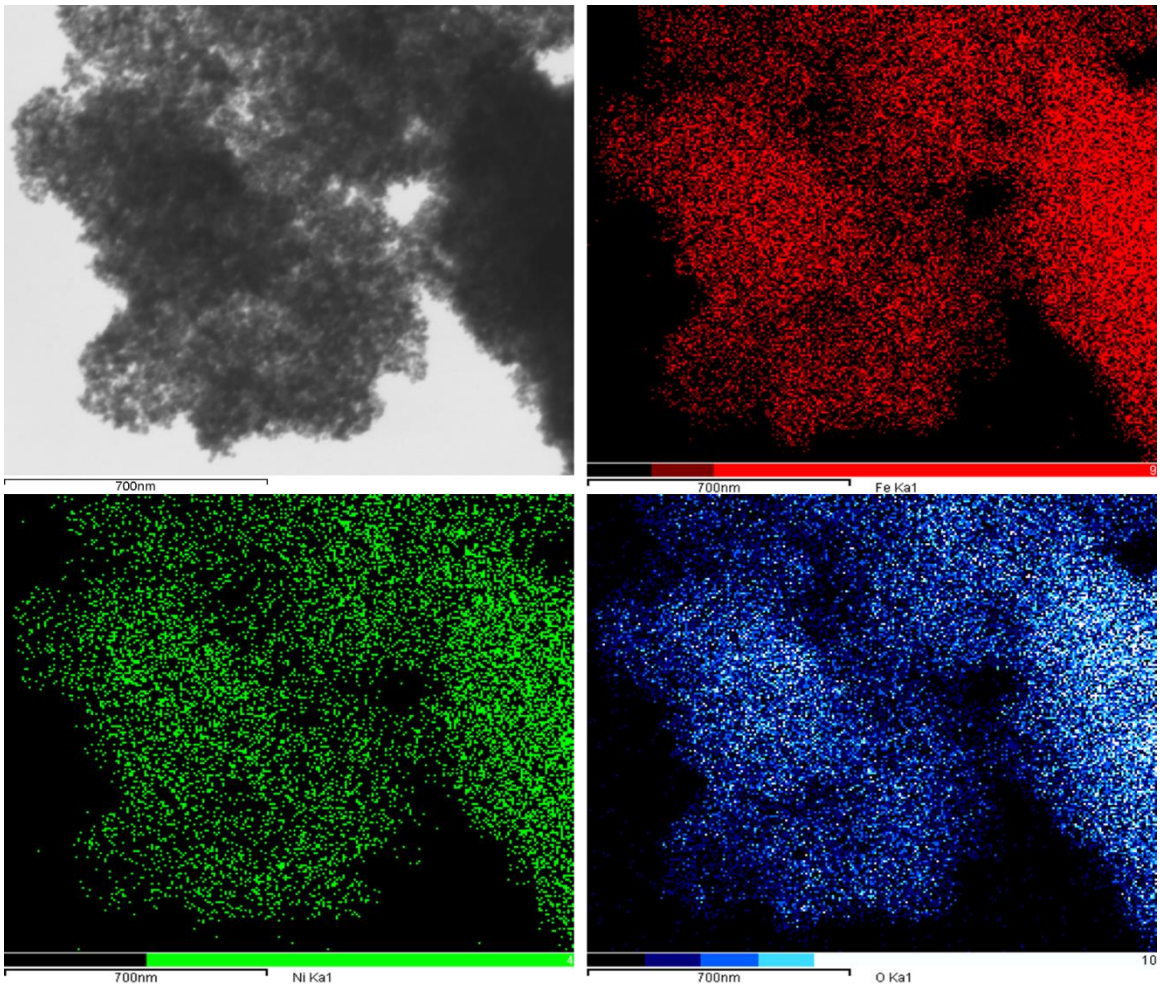

Figure 5-2: SEM images (top left) and SEM-EDX elemental maps (right) of the as-prepared Fe3Ni nanoparticles. The elemental map for Fe is shown in red (top right), Ni in green (bottom left) and O in blue (bottom right).

For the bimetallic nanoparticles, an increase in iron content appears to increase the average crystallite size, confirmed visually by the narrowing reflexes with iron content. This agrees with the increase in particle size with iron content observed in TEM (see section 5.1.1). The Scherrer equation (Equation 5-2 below) is used to compute the volume weighted crystallite size for the nanoparticles using the most intense reflex. This equation relates the average diameter (D_v) to the wavelength of the X-rays (λ), peak broadening due to particle size (β, FWHM) and the position of the reflex measured (θ). The absolute values obtained from this calculation are not reliable because the contributions to peak broadening from the instrument and strain have not been considered, however the trend in sizes is reliable as this is a series of measurements done on similar samples, measured with the same instrument, and measuring the same reflex.

$$n\lambda = 2d \sin\theta \qquad \text{Eq 5-1}$$

$$d_v = \frac{K\lambda}{(\beta \cos\theta)}$$ Eq 5-2

The results are presented in Table 5-2 above which shows the increase in average crystallite size with an increase in iron content for the bimetallic particles. This overall trend agrees with the TEM results.

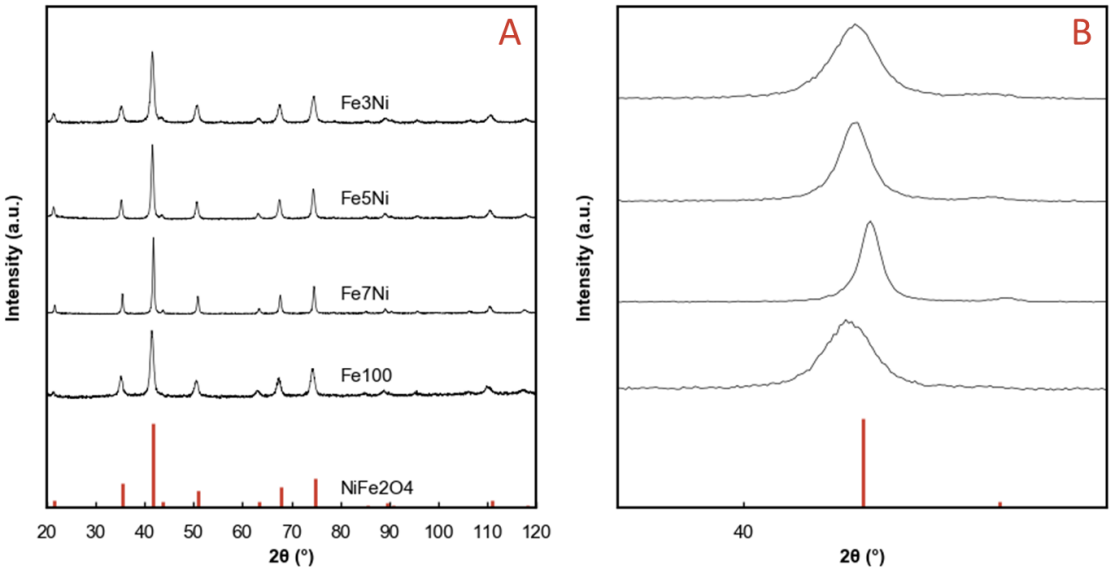

Figure 5-3: XRD patterns of the as-prepared (Ni_xFe_{1-x})Fe_2O_4 nanoparticles (A) and the most intense reflex of the as-prepared nanoparticles, showing a shift in 2θ with iron content (B).

5.2 MO_X OVERLAYERS

The characterizations discussed below show that 2D overlayer coverage of MOx on γ-Al_2O_3 is achieved i.e., that no bulk metal oxides have formed on the γ-Al_2O_3 surface, and that the pore geometry of the γ-Al_2O_3 carrier is maintained. The reducibility and Lewis acidity/basicity of the MOx@Al_2O_3 overlayers was investigated by Raseale (2022) and was therefore not studied again here, but will be referenced. Although monolayer coverage was targeted, the materials are more generally termed 'overlayers' because perfect monolayer coverage cannot be confirmed due to the detection limits of the characterization techniques used. This is particularly relevant for the supported metal catalyst samples where the nominal monolayer is subjected to ultrasonication, which could further alter the surface of the bare, as-prepared MOx@Al_2O_3 materials.

5.2.1 XRD

Figure 5-4 below shows the XRD patterns collected for the prepared CrOx@Al_2O_3 and GaOx@Al_2O_3 overlayers compared to bulk oxide references and to the γ-Al_2O_3 carrier. The only reflexes recorded for the prepared overlayer samples belong to the γ-Al_2O_3 carrier i.e., there is no contribution from either bulk oxide. The XRD patterns suggests a highly dispersed coating of MOx on the γ-Al_2O_3 carrier.

It is also possible that bulk MOx exists in the form of very small crystallites below the detection limit of XRD (< 3 nm) though this is not supported by the additional characterizations described below.

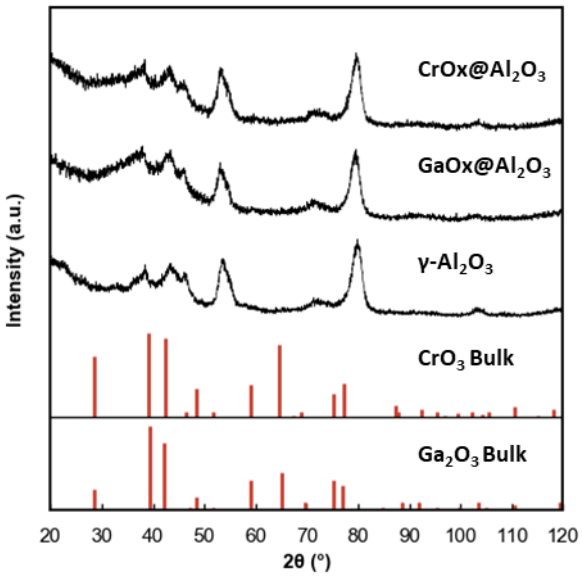

Figure 5-4: XRD patterns of the prepared $CrOx@Al_2O_3$ and $GaOx@Al_2O_3$ overlayers compared to bulk oxide references and to the γ-Al_2O_3 carrier.

5.2.2 Raman spectroscopy

Raman spectroscopy offers near-surface sensitivity which was used to further investigate the chemical species present on the prepared $CrOx@Al_2O_3$ and $GaOx@Al_2O_3$ overlayers. Figure below shows the Raman spectra collected for the prepared overlayers compared to references for their respective bulk oxides. The γ-Al_2O_3 carrier shows no Raman features in this range (Martinezhuerta et al., 2006) therefore the observed bands are attributable to the MOx species. The bulk references show characteristic bands below 770 cm^{-1} which are absent from the prepared overlayers' spectra, further supporting that the CrOx and GaOx respectively exist as 2D overlayers on the γ-Al_2O_3 surface without bulk characteristics. The overlayer materials can therefore be understood as a surface-modified γ-Al_2O_3, rather than as directly comparable to their respective bulk oxides.

5.2.3 Nitrogen physisorption analysis (BET)

The mass-specific surface areas were determined using the BET method based on collected N_2 adsorption/desorption isotherms. The textural properties of the prepared $MOx@Al_2O_3$ overlayer materials are presented in Table 5-3 below and are compared to the γ-Al_2O_3 carrier. There is a decrease in mass-specific surface area, S_{BET}, and pore volume, V_{pore}, seen from the γ-Al_2O_3 to each of the $MOx@Al_2O_3$ overlayers. This is most likely due to the partial filling of smaller pores of the materials when the MOx is dispersed onto the γ-Al_2O_3 carrier surface. This partial filling also causes the slight increase in the average pore diameter and decrease in the pore volume for $GaOx@Al_2O_3$.

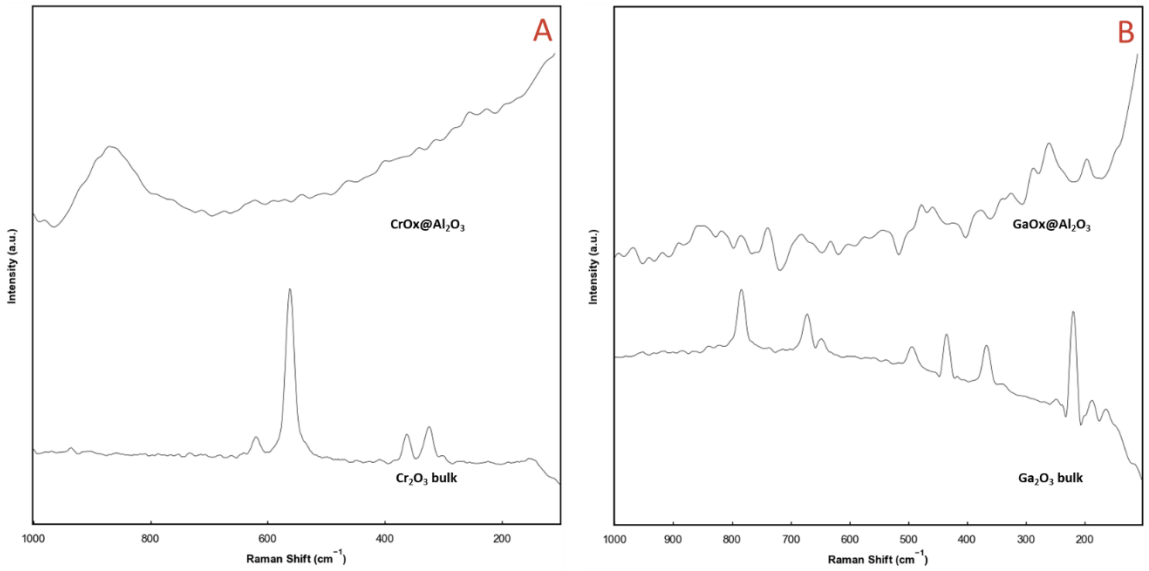

Figure 5-5: Raman spectra of prepared $MOx@Al_2O_3$ (M = Cr (A) and Ga (B)) with corresponding bulk metal oxide references.

The BET results support the successful synthesis of the $CrOx@Al_2O_3$ and $GaOx@Al_2O_3$ overlayers, specifically that their textural properties are comparable. Thus, the contribution of differences in surface area to any observed differences in activity during catalytic performance evaluation between supports is limited. The inert SiO_2 support, utilized to study the effect of the metallic Fe_xNi_y phases without support effects, has a greater mass-specific surface area than either $CrOx@Al_2O_3$ or $GaOx@Al_2O_3$, which will be taken into consideration.

Table 5-3 Textural properties of prepared $MOx@Al_2O_3$ supports compared to γ-Al_2O_3 carrier.

Sample	S_{BET} (m^2/g)	V_{pore} (cm^3/g)	d_{pore} (nm)
SiO_2*	200 ± 25		
γ-Al_2O_3	152	0.44	11.7
$CrOx@Al_2O_3$	140	0.41	11.7
$GaOx@Al_2O_3$	130	0.40	12.3

**S_{BET} for Aerosil 200 SiO_2 support taken from manufacturer*

5.3 SUPPORTED CATALYSTS

The characterizations discussed below demonstrate that the nanoparticles were effectively anchored onto the support materials, achieving good dispersion of the active metals. For the $MOx@Al_2O_3$ supports, it was confirmed that the 2D overlayer coverage of MOx on the γ-Al_2O_3 remains intact during the supporting protocol, as well us under high-temperature reducing and oxidizing environments, as no bulk MOx crystallites were detected.

5.3.1 XRD

XRD patterns obtained for the library of 12 supported metal catalysts and three bare supports compared to the $NiFe_2O_4$ reference are available in Figure 5-6. For the SiO_2-supported samples, the only observable reflexes are for the $(Ni_xFe_{1-x})Fe_2O_4$ nanoparticles and the amorphous hump corresponding to SiO_2 near 25° 2θ.

For the overlayer-supported materials, the only features observed are reflexes associated with the $(Ni_xFe_{1-x})Fe_2O_4$ nanoparticles and the underlying γ-Al_2O_3 carrier. No reflexes for bulk oxides of Cr or Ga are observed, suggesting the 2D overlayer coverage of MOx on the γ-Al_2O_3 is maintained after the nanoparticles are supported.

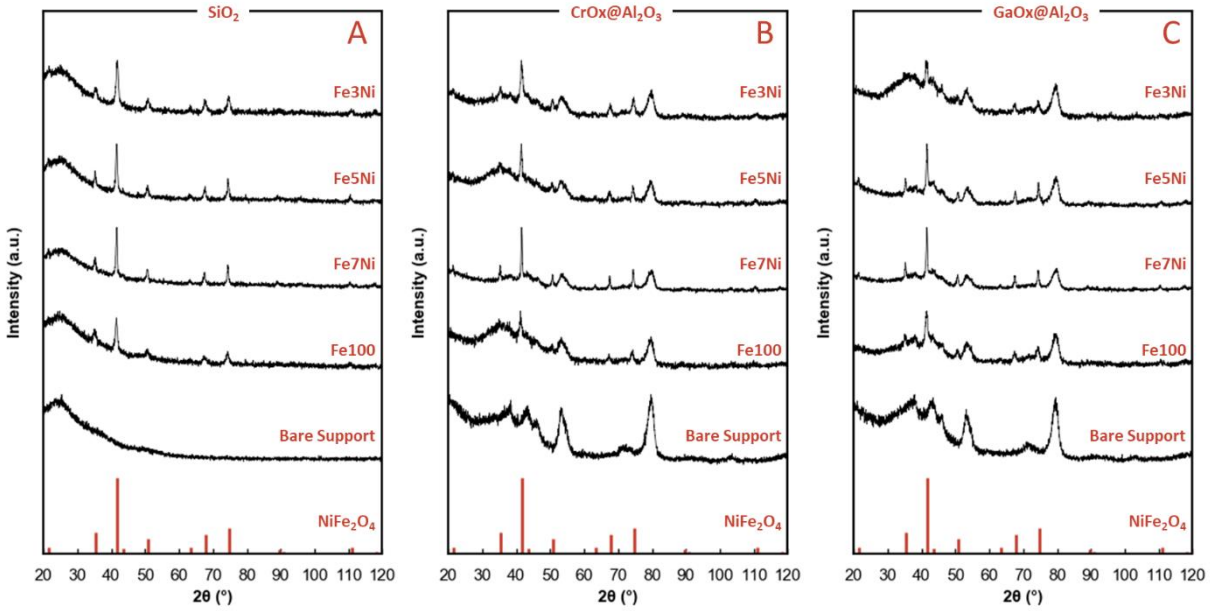

Figure 5-6: XRD patterns of supported nanoparticles of varying composition, and bare supports for SiO_2 (A), CrOx@Al_2O_3 (B) and GaOx@Al_2O_3 (C).

5.3.2 TPR

The reduction of 6 supported samples was investigated in temperature-programmed reduction (TPR) experiments in an *in-situ* XRD setup. The active phases for RWGS are the metallic Fe and Fe-Ni alloys. To obtain these phases the oxidic precursor particles are reduced in a flow of H_2 at elevated temperatures *in-situ* in the fixed-bed reactor setup for catalytic performance evaluation. The reduction onset temperature, the phase evolution during reaction, and the phase composition of the final reduced catalyst are therefore of interest in understanding catalytic performance.

Fe7Ni and Fe3Ni supported on the three supports, SiO_2, CrOx@Al_2O_3 and GaOx@Al_2O_3, were studied. This selection allows for both the effects of iron content and MOx support material on the reducibility of the nanoparticles to be studied, as well as showing potential interactions between the metallic

composition and the MOx support. The key results of each study are the onset temperature of nanoparticle reduction and the alloy phase distribution after reduction.

An illustrative guide on how the top view *in-situ* XRD patterns should be read based on the exemplary reduction of Fe3Ni/SiO_2 is provided in Figure 5-7. The strong reflex at 0.40 $Å^{-1}$ observed in the region between 50 and 300 °C corresponds to the most intense reflex of the oxidic precursor particles and is used to track the disappearance or appearance of the oxide phase. The other reflexes observed in this region at 0.68 $Å^{-1}$, 0.62 $Å^{-1}$ and 0.42 $Å^{-1}$ also correspond to the oxide, but they are weaker and, in some cases, overlap with the relevant metallic phases. In this example, the reflexes observed from 400 °C onwards correspond to the metallic alloy phases. At the most intense reflex near 0.48 $Å^{-1}$ there is an overlap of reflexes from the bcc and fcc alloy phases (0.49 $Å^{-1}$ and at 0.48 $Å^{-1}$ respectively). The reflex at 0.56 $Å^{-1}$ corresponds to the fcc phase and the reflex at 0.70 $Å^{-1}$ corresponds to the bcc phase, so these two reflexes will be used to track the appearance and disappearance of the alloy phases.

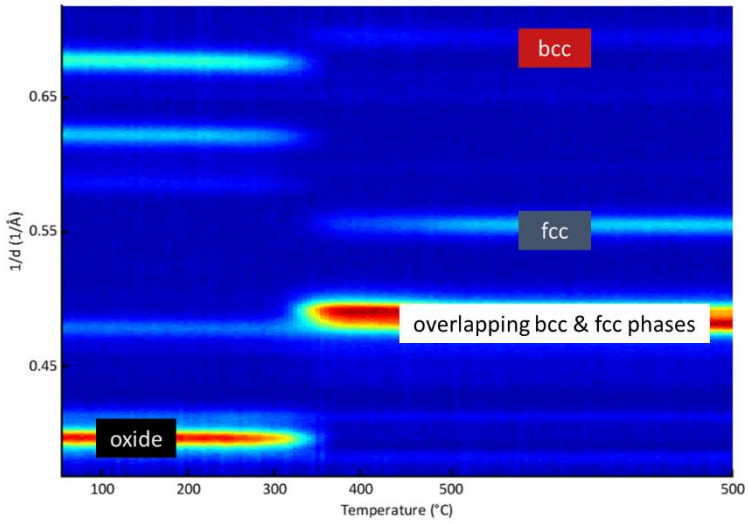

Figure 5-7: Illustrative guide showing the positions of the relevant reflexes of the $(Ni_xFe_{1-x})Fe_2O_4$ oxide phase, bcc Fe-Ni alloy phase and fcc Fe-Ni alloy phase respectively

The respective Fe:Ni atomic ratios were assumed and kept constant for the oxide precursor nanoparticles, the bcc alloy phase and fcc alloy phase for all the refinements presented in this chapter. Variations thereof are accounted for by varying lattice parameters if necessary. Specifically, the oxide precursor particles were assumed to be $Fe_{25}Ni_{75}Fe_2O_4$ and the fcc and bcc phases were assumed to be Fe_1Ni_1. Across all studies, the bcc phase is refined with less precision than the fcc and oxide phases. This is because over the short range of the XRD scans, the most intense reflex for the bcc phase is overlapping with reflexes from the fcc and underlying Al_2O_3 support, and the second reflex visible in this range has a low relative intensity. For this reason, the phase compositions are reported as trends and may not be numerically precise.

TPR experiments were performed in the *in-situ* XRD. Figure 5-8 and shows the top view of *in-situ* XRD patterns (top), the evolution of crystallite size (middle) and the phase evolution (bottom) for TPR over SiO_2-supported Fe3Ni (A, left) and Fe7Ni (B, right). There is agreement between these refined crystallite sizes and what was reported in Table 5-2 above for the unsupported nanoparticles, with the oxide phase in Fe7Ni/SiO_2 having a greater crystallite size than in Fe3Ni/SiO_2. In both cases, the metallic phases begin to appear just before 300 °C and by 375 °C the oxide phase has disappeared, and only metallic phases are observed. A decrease in the crystallite size of the oxide particles within this temperature range is observed which could suggest that the larger oxide particles are initially preferably reduced, however the error of the refinement increases as the concentration of the analyte decreases. The phase composition and crystallite sizes stabilize as the temperature is held at 500 °C and the final reduced sample consists of a mixture of bcc and fcc alloy phases. In the Fe3Ni sample (Figure 5-8A) the final composition is 55 wt.% fcc and 45 wt.% bcc while in the Fe7Ni sample the final composition is 20 wt.% fcc and 80 wt.% bcc. This increase of bcc phase with an increase in iron content agrees with the work by Raseale et al. (2021) discussed in chapter 2.2. In both samples, there is a greater proportion of the bcc phase initially upon reduction compared to the final reduced composition. This relative shift to fcc with an increase in temperature correlates well with the bulk Fe-Ni phase diagram presented earlier in Figure 2-7. For emphasis, no significant sintering is observed in the metallic crystallites once the final reduction temperature of 500 °C is reached.

Figure 5-9 below shows the TPR results over CrOx-supported Fe3Ni (A, top) and Fe7Ni (B, bottom). The weak reflexes at 0.42 $Å^{-1}$ and 0.50 $Å^{-1}$ correspond with the underlying γ-Al_2O_3 carrier and thus is present throughout all *in-situ* XRD studies on the MOx-supported samples. The initial appearance of the metallic alloy phases is delayed on both CrOx-supported samples compared to SiO_2, with the reflex for the bcc phase at 0.49 $Å^{-1}$ first emerging near 400 °C and the oxide only completely disappearing after 450 °C. Thus, the CrOx@Al_2O_3 overlayer materials appears to have hindered the reduction of the precursor materials compared to SiO_2. The final phase composition of the reduced samples with respect to iron content follows the observations on SiO_2, with an increase in iron increasing the proportion of the bcc phase. Once again, the compositions stabilize, and no significant sintering is observed after the temperature first reaches 500 °C.

The reduction of the GaOx-supported samples can be seen in Figure 5-10 below for Fe3Ni (A, top) and Fe7Ni (B, bottom). The reflexes from Al_2O_3 at 0.42 $Å^{-1}$ and 0.50 $Å^{-1}$ are visible throughout the study. Both samples behave similarly to their equivalents supported on SiO_2 in terms of reduction onset. The bcc phase at 0.49 $Å^{-1}$ first emerges near 300 °C followed by the fcc phase. The oxide has completely disappeared by 400 °C. The final metallic compositions show an increase in the bcc phase with an

increase in iron content. The phase compositions and crystallite sizes are stable when the sample is held at 500 °C.

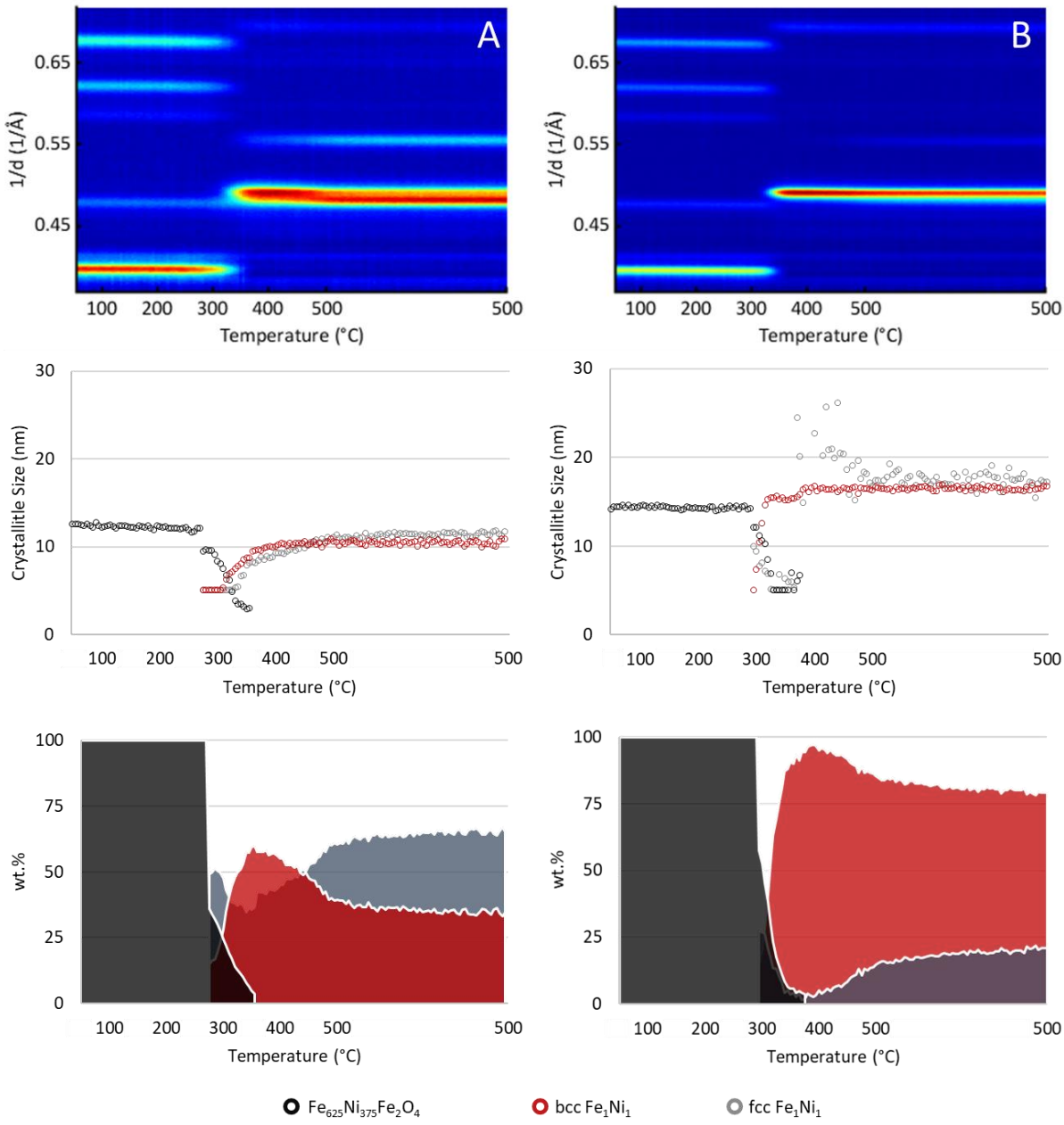

Figure 5-8: Top view of in-situ XRD patterns (top), evolution of crystallite size (middle) and phase evolution (bottom) of TPR experiments performed in the in-situ XRD over SiO_2-supported Fe3Ni (A, left) and Fe7Ni (B, right). The samples were heated to the reduction temperature of 500 °C in 5 vol.-% H_2 in N_2 at a heating rate of 1 °C/min and held at 500 °C for 5 hours.

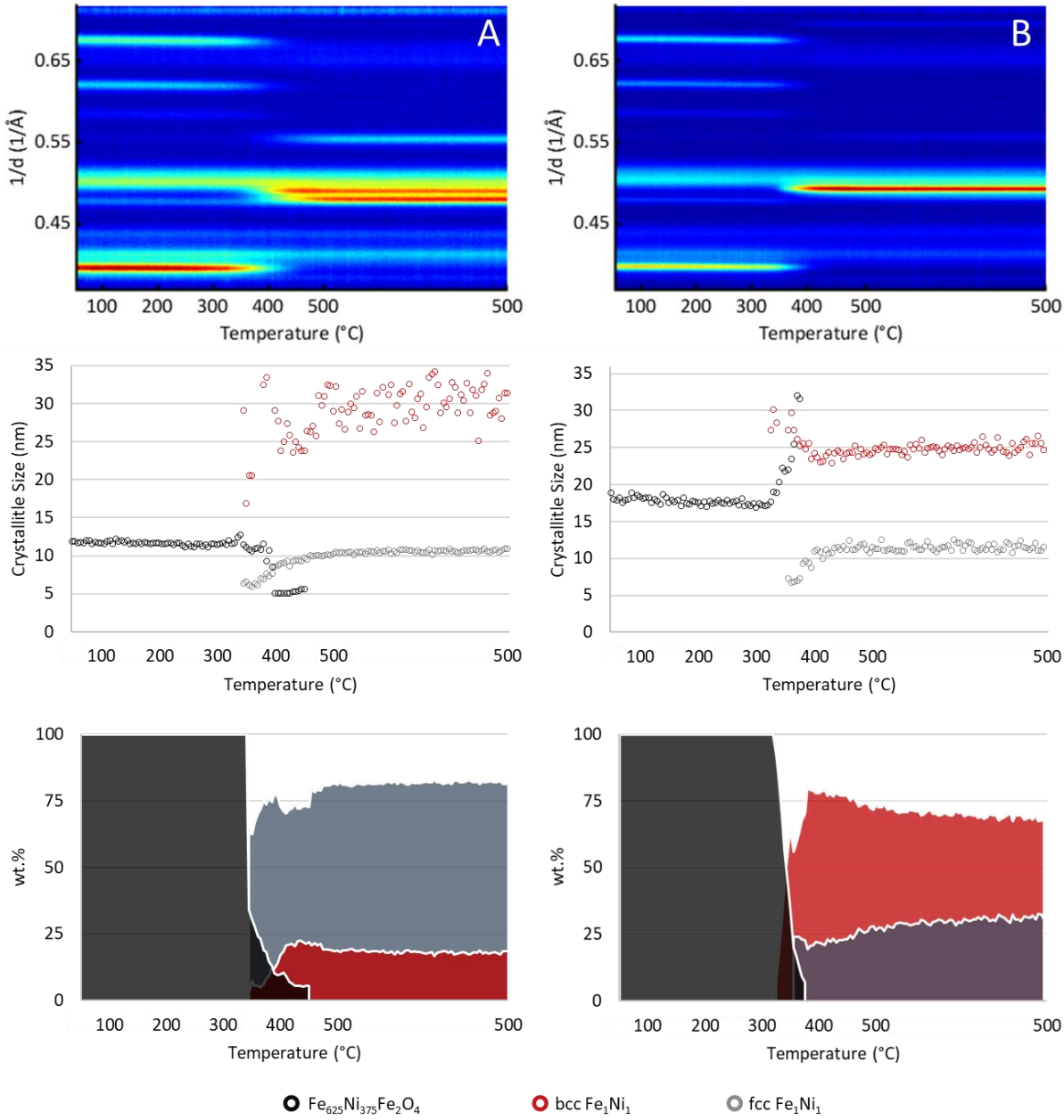

Figure 5-9: Top view of in-situ XRD patterns (top), evolution of crystallite size (middle) and phase evolution (bottom) of TPR experiments performed in the in-situ XRD over CrOx-supported Fe3Ni (A, left) and Fe7Ni (B, right). The samples were heated to the reduction temperature of 500 °C in 5 vol.-% H_2 in N_2 at a heating rate of 1 °C/min and held at 500 °C for 5 hours.

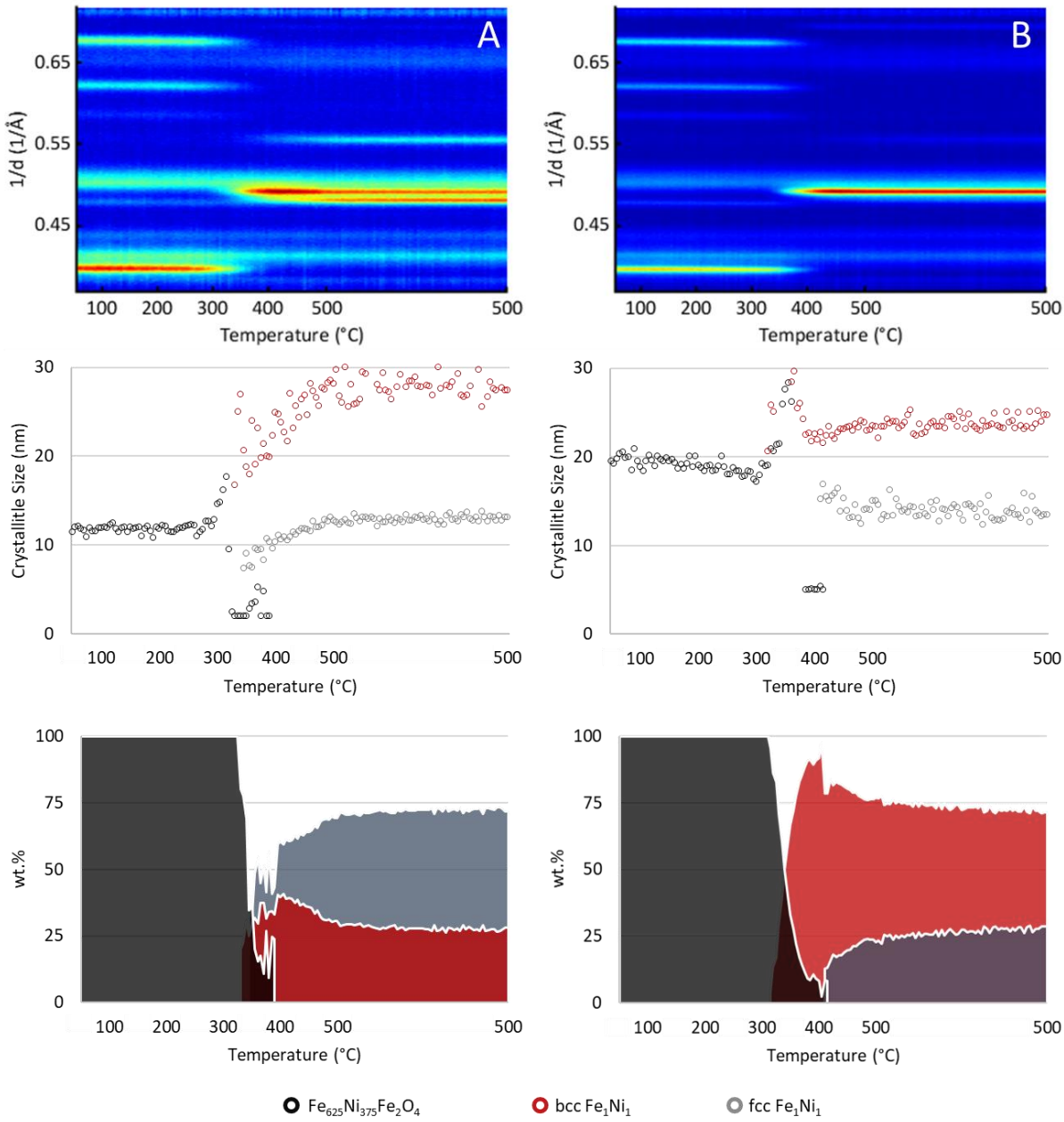

Figure 5-10: Top view of in-situ XRD patterns (top), evolution of crystallite size (middle) and phase evolution (bottom) of TPR experiments performed in the in-situ XRD over GaOx-supported Fe3Ni (A, left) and Fe7Ni (B, right). The samples were heated to the reduction temperature of 500 °C in 5 vol.-% H_2 in N_2 at a heating rate of 1 °C/min and held at 500 °C for 5 hours.

The combined results of the TPR study are summarized in Figure 5-11 below. The final phase composition per iron content is similar across supports – i.e., all supported Fe3Ni samples show a bcc content of 20 – 30 % and the Fe7Ni samples show a bcc content of 70 – 80 %. In terms of reduction onset, the onset temperature for the SiO_2 and GaOx-supported samples increases with an increase in iron content but decreases with an increase in iron content on CrOx@Al_2O_3. Both observed onset temperatures on the CrOx-supported samples are also much higher than observed for the SiO_2 and GaOx-supported samples.

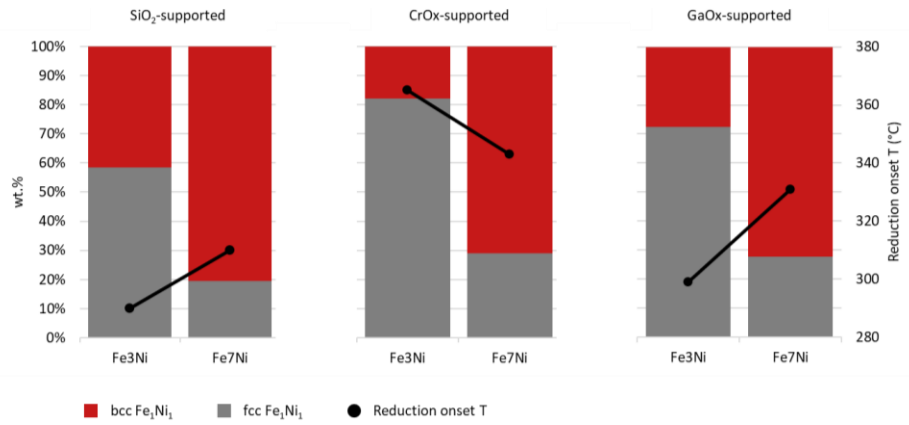

Figure 5-11: Reduction onset temperature and phase compositions in reduced catalysts from TPR experiments.

5.3.3 Temperature-programmed CO_2 activation

Because the activation of CO_2 is a key step in the RWGS reaction, temperature programmed CO_2 activation was studied in both the fixed-bed reactor set-up and in the *in-situ* XRD.

In the *in-situ* XRD 6 catalysts were studied, namely the bimetallic samples with the highest and lowest iron content, Fe7Ni and Fe3Ni respectively, supported on the 3 supports - SiO_2, $CrOx@Al_2O_3$ and $GaOx@Al_2O_3$. This selection allows for the independent effects of iron content and MOx support material on the phase transformations to be studied upon CO_2 activation, as well as potential interactions between bimetallic composition and MOx support. The key results from this study are the onset temperature for re-oxidation of the alloy phase, and the phase evolution profile during CO_2 activation. See Figure 5-7 above for an illustrative guide on how the top view *in-situ* XRD patterns should be read.

Figure 5-12 below shows results from CO_2 activation studies on $Fe3Ni/SiO_2$ (A) and $Fe7Ni/SiO_2$ (B). The initial composition is the mixture of bcc and fcc alloy phases obtained after reduction (see Figure 5-8). When exposed to a dilute CO_2 stream near 275 °C there is partial re-oxidation back to the $(Ni_xFe_{1-x})Fe_2O_4$ spinel structure, as seen by the appearance of the strong reflex at 0.40 $Å^{-1}$ for both samples. By tracking the reflexes of the metallic phases between 300 and 500 °C it is observed that the intensity of the fcc phase at 0.56 $Å^{-1}$ remains constant while the bcc phase at 0.70 $Å^{-1}$ disappears, suggesting that only the bcc phase is re-oxidized in this temperature range. The decrease in crystallite size observed over this temperature range could suggest that larger crystallites are preferentially oxidized first, though the increasing error of refinement at decreasing concentrations should be considered. No sintering of any of the crystallites is observed at elevated temperatures (above 400 °C). The refined phase compositions show a relative increase in the weight fraction for the fcc phase over this range, which would not be expected if the fcc was inert and the only change taking place was the oxidation of the bcc to the oxide. Given that the reflex intensity of the fcc phase remains constant, it is likely

that the oxide is partially amorphous, and therefore XRD-invisible, and that the concentration of fcc is overestimated. The observation that the bcc surface of the iron-nickel alloy activates CO_2 while the fcc structure is inert is consistent with the observations made by Raseale et al. (2021).

Between 500 and 700 °C, the fcc reflex at 0.56 $Å^{-1}$ of Fe3Ni/SiO_2 appears to decrease in intensity while the relative weight fraction of the oxide phase increases. This suggests that there is some activation of CO_2 by the fcc phase at this higher temperature range which was not observed by Raseale et al. (2021). This is not seen in the Fe7Ni/SiO_2 sample, probably because the fcc content in this reduced sample is lower and minor changes cannot be observed. It is likely for a similar reason that this activation of CO_2 by the fcc phase was not previously observed by Raseale et al. (2021), who studied the Fe:Ni atomic ratios of 1:1 and 5:1. In the 1:1 sample, the fcc phase is possibly too dominant for minor decreases to be observed, while in the 5:1 sample it is too low in concentration.

There is a slight difference in the observed onset temperature for re-oxidation between alloy compositions on SiO_2. In the Fe3Ni sample, re-oxidation is first observed around 270 °C and in the Fe7Ni sample re-oxidation is first observed at 290 °C. This narrow difference should be considered in light of the overall experimental uncertainties.

Once 700 °C is reached the oxide phase disappears and the intensity of the fcc phase increases, suggesting a decomposition of the oxide phase at this elevated temperature. The fact that only an fcc phase is present at this temperature is consistent with the bulk Fe-Ni phase diagram presented in Figure 2-7. The decomposition appears to take place through a Wüstite (FeO) phase, as seen by the emergence and consequent disappearance of the reflex at 0.46 $Å^{-1}$.

Figure 5-13 below shows the results of CO_2 activation over the CrOx-supported Fe3Ni (A) and Fe7Ni (B). Both samples behave similarly to the SiO_2-supported samples with respect to the observed phase transformations upon CO_2 activation. In the lower temperature range the bcc phase is exclusively re-oxidized back to the spinel structure while the fcc phase remains unchanged. After the bcc phase is completely consumed and at elevated temperatures (~600 °C), the fcc phase is partially re-oxidized, seen by a weakening of the fcc reflex at 0.56 $Å^{-1}$ and a relative increase in the weight fraction of the oxide phase over this temperature range. This shows that the fcc phase requires a higher temperature for CO_2 activation and it is more protected from bulk oxidation.

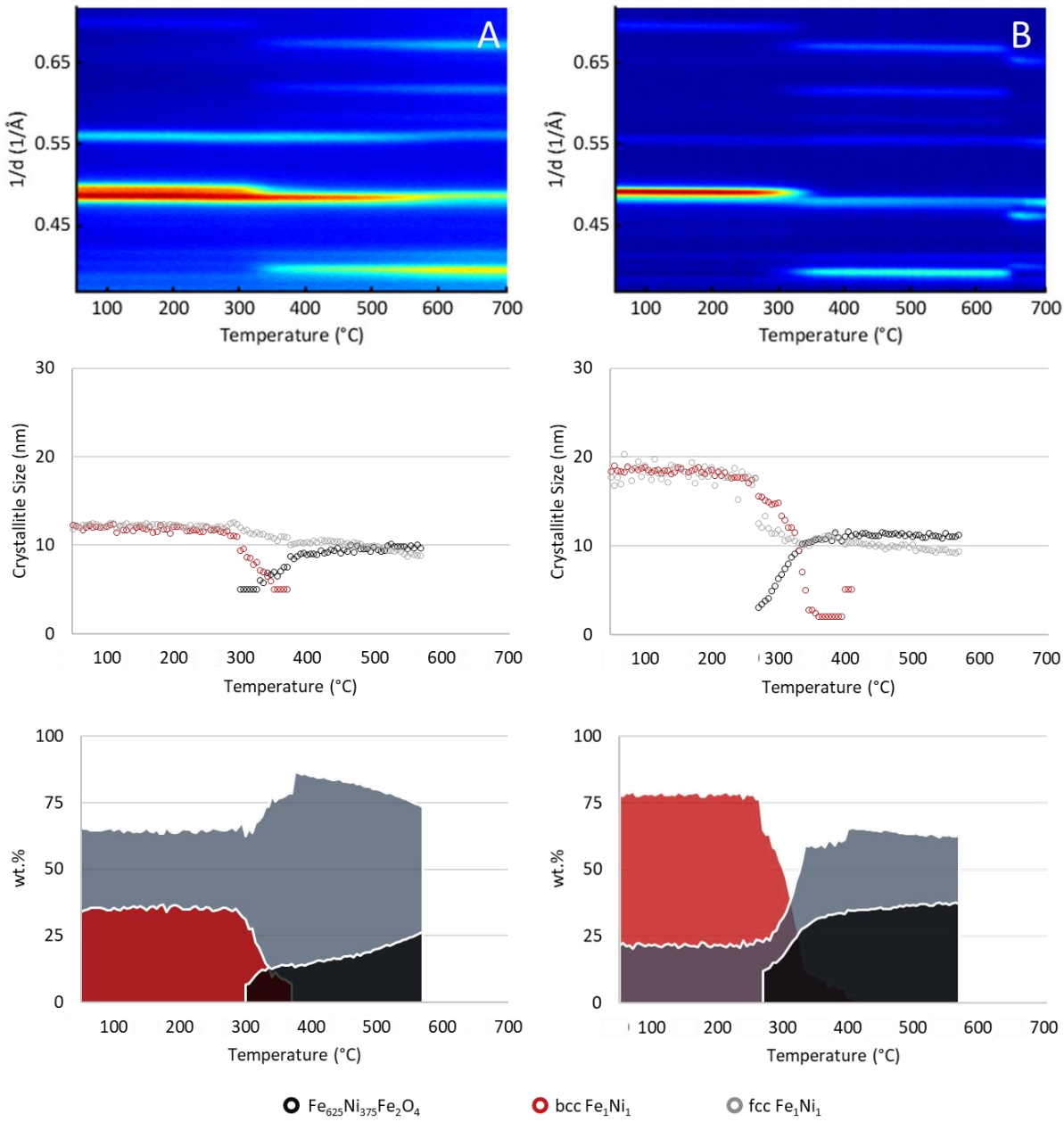

Figure 5-12: Top view of in-situ XRD patterns (top), evolution of crystallite size (middle) and phase evolution (bottom) of temperature-programmed CO_2 experiments performed in the in-situ XRD over SiO_2-supported Fe3Ni (A, left) and Fe7Ni (B, right). The reduced samples were heated to the target temperature of 700 °C in 5 vol.-% CO_2 in N_2 at a heating rate of 1 °C/min and held at 700 °C for 30 minutes.

A more significant difference in re-oxidation onset temperature is observed between the two Fe:Ni ratios on the CrOx@Al_2O_3 overlayer. In the Fe3Ni sample, re-oxidation is first observed near 230 °C and in the Fe7Ni sample re-oxidation is first observed near 260 °C. Both temperatures are lower than in the case of SiO_2, showing enhanced CO_2 activation on CrOx@Al_2O_3. The trend with iron content is consistent with the trend on SiO_2, with the sample lower in Fe showing an earlier re-oxidation of the bcc phase. Again, no sintering of any of the crystallites is observed at elevated temperatures (above 400 °C). The increased variance in crystallite size for the bcc phase of Fe7Ni/CrOx@Al_2O_3 during its

consumption reflects that this phase was refined with a greater error. After 700 °C is reached, the oxide decomposes into a pure fcc alloy phase. Here, no Wüstite phase is detected.

Figure 5-14 below shows the results of CO_2 activation over the GaOx-supported Fe3Ni (A) and Fe7Ni (B). The overall phase evolutions over the course of the experiment are consistent with the observations on SiO_2 and CrOx@Al_2O_3. At the start of the experiment the mixture of bcc and fcc Fe-Ni phases are present. The bcc phase is re-oxidized near 300 °C while the fcc phase is unchanged in this range. There is a partial re-oxidation of the fcc phase near 600 °C. Lastly, the oxide phase is decomposed to fcc at 700 °C. The GaOx-supported samples showed the greatest difference in re-oxidation onset temperature with iron content. In the Fe3Ni sample, re-oxidation is first observed near 285 °C and in the Fe7Ni sample re-oxidation is first observed near 245 °C. Not only is this the greatest observed difference across the three supports in re-oxidation onset temperature with iron content, but the trend in iron content is reversed from SiO_2 and CrOx@Al_2O_3.

The CO_2 activation studies showed that the bcc Fe-Ni phase was completely consumed under oxidizing conditions while the fcc Fe-Ni phase was partially re-oxidized at elevated temperatures (> 600 °C). In the SiO_2 and CrOx-supported samples, re-oxidation onset temperature increased with an increase in iron content and for the GaOx-supported samples it decreased with an increase in iron content. For each Fe:Ni composition, the re-oxidation onset temperature was lower when the alloys were supported on CrOx@Al_2O_3 compared to SiO_2 and GaOx@Al_2O_3.

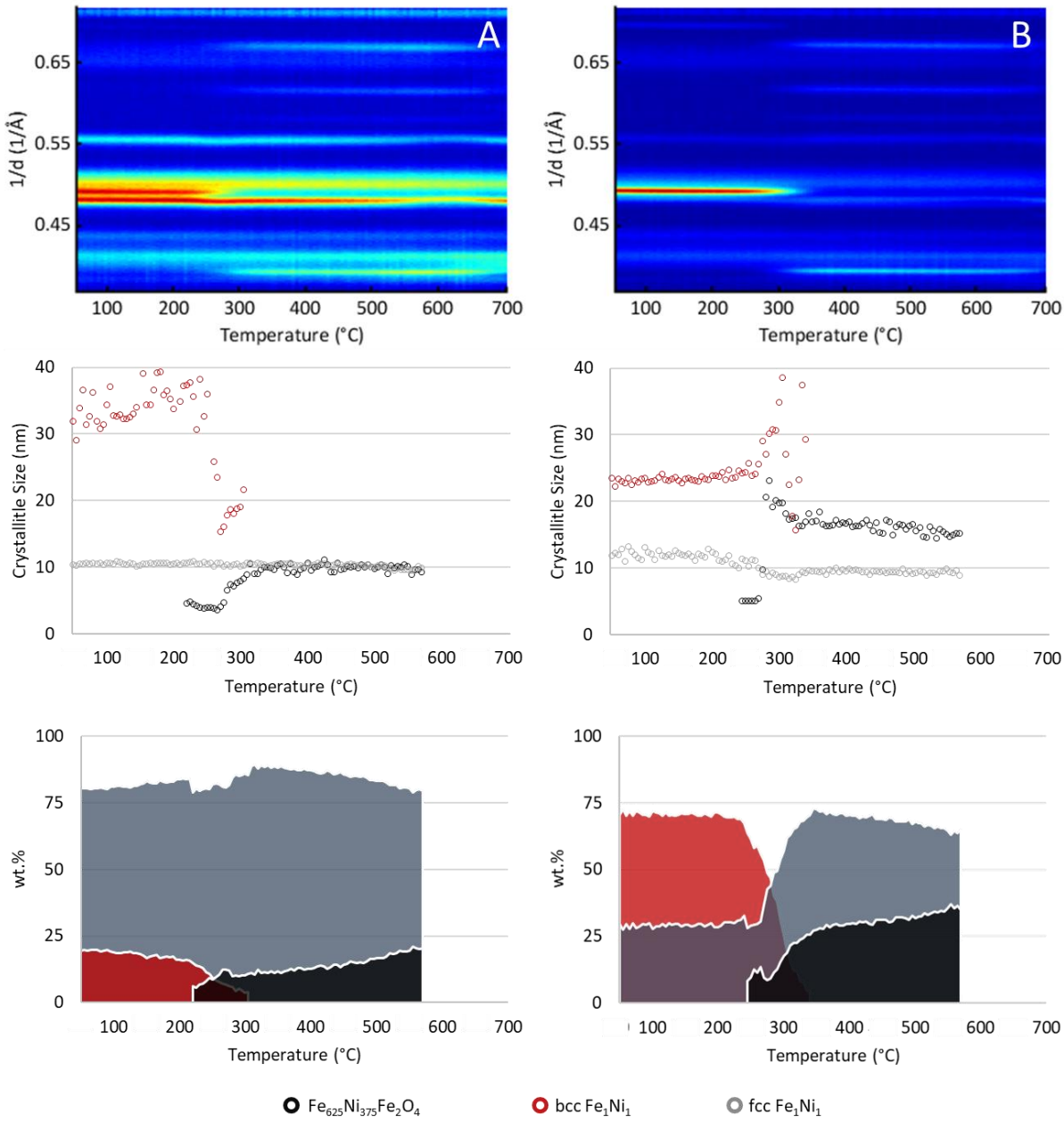

Figure 5-13: Top view of in-situ XRD patterns (top), evolution of crystallite size (middle) and phase evolution (bottom) of temperature-programmed CO_2 experiments performed in the in-situ XRD over CrOx-supported Fe3Ni (A, left) and Fe7Ni (B, right). The reduced samples were heated to the target temperature of 700 °C in 5 vol.-% CO_2 in N_2 at a heating rate of 1 °C/min and held at 700 °C for 30 minutes.

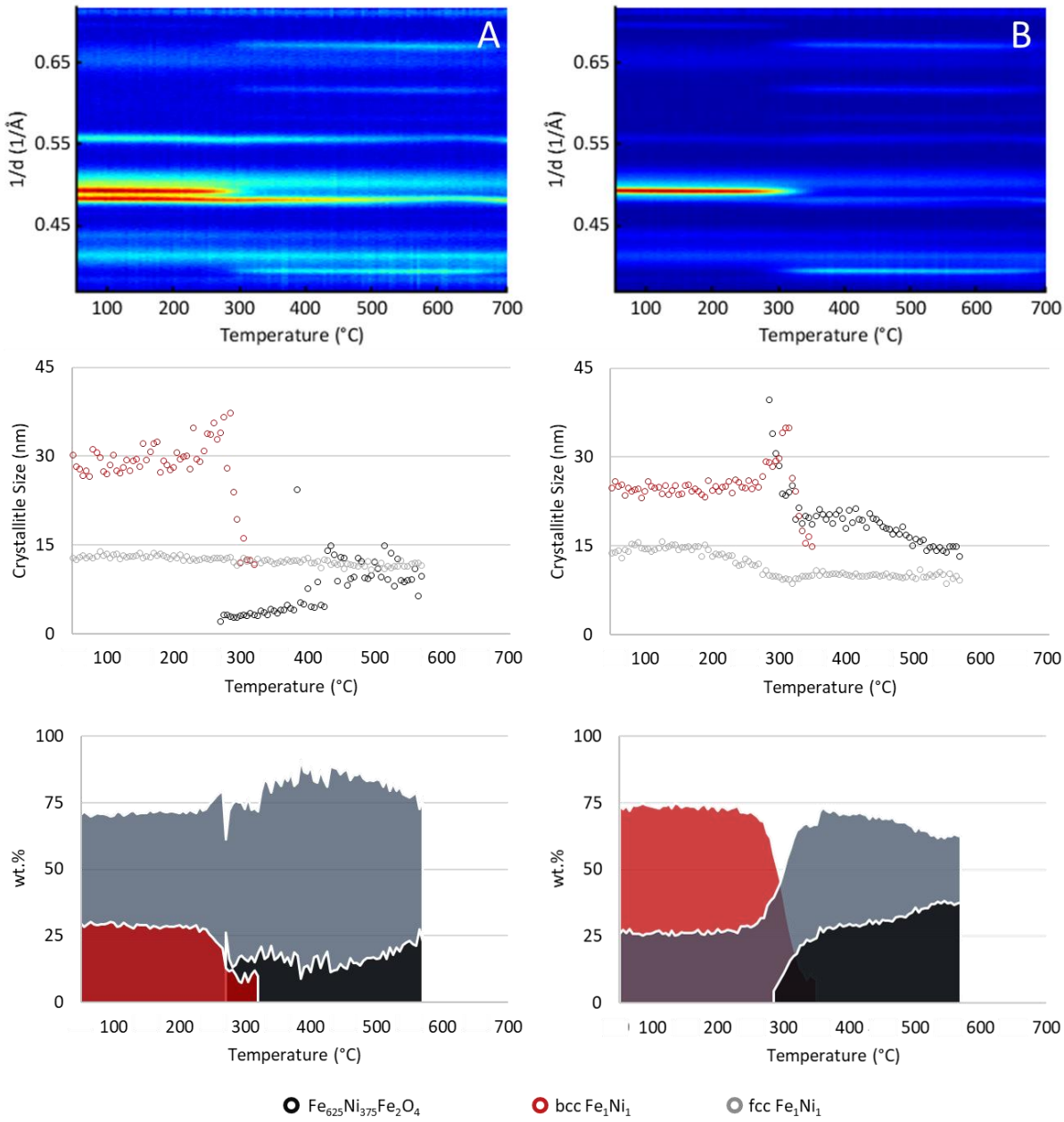

Figure 5-14: Top view of in-situ XRD patterns (top), evolution of crystallite size (middle) and phase evolution (bottom) of temperature-programmed CO_2 experiments performed in the in-situ XRD over GaOx-supported Fe3Ni (A, left) and Fe7Ni (B, right). The reduced samples were heated to the target temperature of 700 °C in 5 vol.-% CO_2 in N_2 at a heating rate of 1 °C/min and held at 700 °C for 30 minutes.

Figure 5-15 below shows CO formation profile as a function of temperature over selected samples in the fixed-bed reactor set-up. The key results of this study are the onset temperature for CO formation, as well as the overall formation profile. The onset temperatures and peak formation rates from the fixed-bed study cannot be numerically compared to those obtained from the *in-situ* XRD study. This is due to differing experimental conditions such as heating rate and space velocity which could not be kept constant due to technical constraints in the *in-situ* XRD cell. However, the trends in behavior across supports and between compositions are comparable.

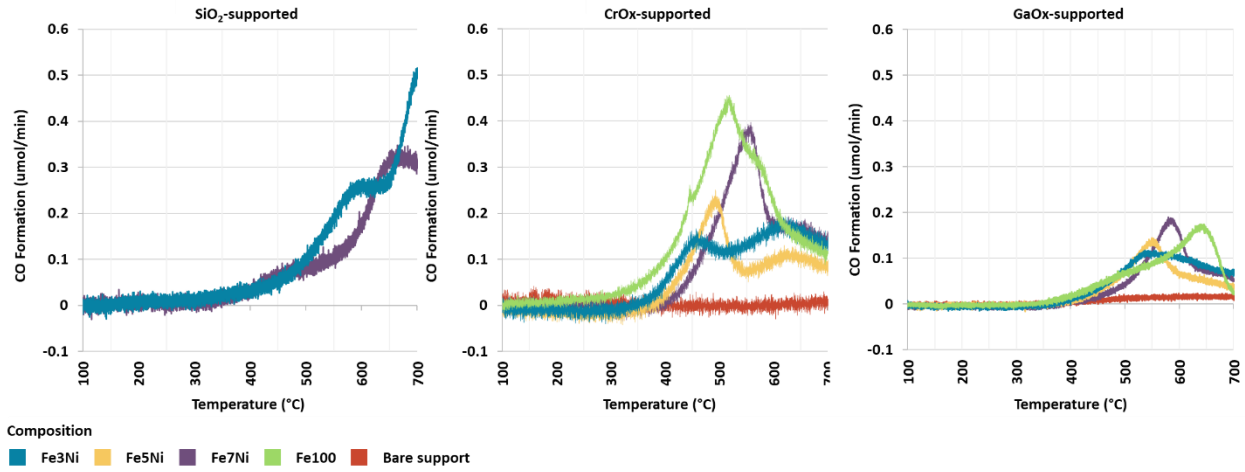

Figure 5-15: CO formation - Temperature programmed CO_2 activation.

The data suggests that there are two regions of CO formation – a potential explanation for this is that the CO formed at lower temperatures is produced from CO_2 activation and dissociation, whereas at the higher temperatures, it is formed by bulk oxidation of the catalyst with some contribution from the oxidation of the fcc phase observed in the *in-situ* XRD experiments presented above. It's therefore proposed that the samples with an earlier onset of CO_2 activation that reach peak formation rate at lower temperatures have a higher intrinsic activity and/or a higher affinity for re-oxidation.

CO formation is first observed between 300 and 400 °C in the samples. On SiO_2, the initial behaviour of both bimetallic compositions is similar, both showing CO formation onset near 350 °C. CO formation continues to increase gradually between 350 and 500 °C after which it increases rapidly, suggesting the catalyst is oxidising rapidly.

The bimetallic CrOx@Al_2O_3 samples show onset temperatures and peak temperatures of CO formation at lower temperatures compared to the SiO_2-supported samples, with an increase in iron content increasing the onset temperature. The overall CO yield, deducible from the area under the curve, increases with an increase in iron content. This agrees with the *in-situ* studies, which show that the bcc phase has a higher affinity for re-oxidation than the fcc phase and that the bcc content of the reduced samples increases with an increase in iron content. Fe100/CrOx@Al_2O_3 stands out from the other supported samples, showing early CO formation and the largest overall CO yield from any of the CrOx-supported samples. An explanation for this is that this sample oxidises too rapidly, and good performance in the RWGS is not expected. The bare CrOx@Al_2O_3 overlayer shows no detectable CO formation.

The bimetallic GaOx@Al_2O_3-supported samples show similar CO formation onset temperatures with one another, but different peak formation temperatures following the trend with iron content observed on CrOx@Al_2O_3. The overall CO yields, deducible from the area under the curve, are lower

than the corresponding CrOx-supported samples but follow the same trend in iron content, corresponding to the bcc content of the reduced samples. Fe100/GaOx@Al_2O_3 shows a similar formation profile to the highest iron content sample on GaOx@Al_2O_3, Fe7Ni/GaOx@Al_2O_3, but shifted to higher temperatures. The bare GaOx@Al_2O_3 shows little CO formation.

There is good agreement between the trends observed in the *in-situ* XRD and the fixed bed set-up experiments. The CO formation onset temperature and observed re-oxidation onset temperatures are both very similar for the SiO_2-supported samples. Fe3Ni/CrOx@Al_2O_3 shows the earliest CO formation onset temperature, peak CO formation temperature and re-oxidation onset temperature in the *in-situ* XRD.

6. CATALYTIC PERFORMANCE EVALUATION

The catalytic performance evaluation was carried out in a dual quartz tube fixed-bed reactor set-up at 600°C and atmospheric pressure. The oxidic catalysts were reduced *in-situ* to obtain the active metallic phases before testing. After catalyst activation, 20 $L \cdot g_{cat}^{-1} \cdot h^{-1}$ of equal parts H_2, CO_2 and Ar were fed to the reactors while the product gas was analyzed using an online GC-TCD. The CO_2 conversion at thermodynamic equilibrium at these conditions is 37 %. The key results from catalytic performance evaluation are activity defined by CO_2 conversion, CO selectivity and stability defined by the loss in activity with time on stream.

6.1 ACTIVITY

Figure 6-1 below shows the CO_2 conversion results for the catalysts supported on SiO_2, CrOx@Al_2O_3 and GaOx@Al_2O_3. Clear, significant differences are observed in activity and stability across supports and between bimetallic compositions.

On the SiO_2-supported samples, all samples show a moderate initial activity between 15 – 25 % CO_2 conversion, but the catalysts deactivate rapidly. After 12 hours TOS, all samples have a CO_2 conversion under 10 %. For the alloy catalysts a clear trend in iron content is observed where an increase in iron results in a higher activity: the CO_2 conversion is 5 %, 7 % and 9 % on SiO_2-support Fe3Ni, Fe5Ni and Fe7Ni, respectively. The sample with the highest iron content, Fe7Ni/SiO_2, only slightly outperforms the pure iron catalyst.

On SiO_2, it is difficult to fairly compare the initial conversions of the samples i.e., within the first two hours as they rapidly deactivate. This is because firstly, in the dual quartz tube set up, only one reactor is sampled at a time for one hour each. Secondly, before analysis starts, the activated sample is held in Ar while the bypass analysis is being conducted. GC analysis begins as the reactant gas flow is

switched from the bypass line to the quartz tubes, and as a result the first few gas samples taken contain additional argon and it takes some minutes for the system to equilibrize.

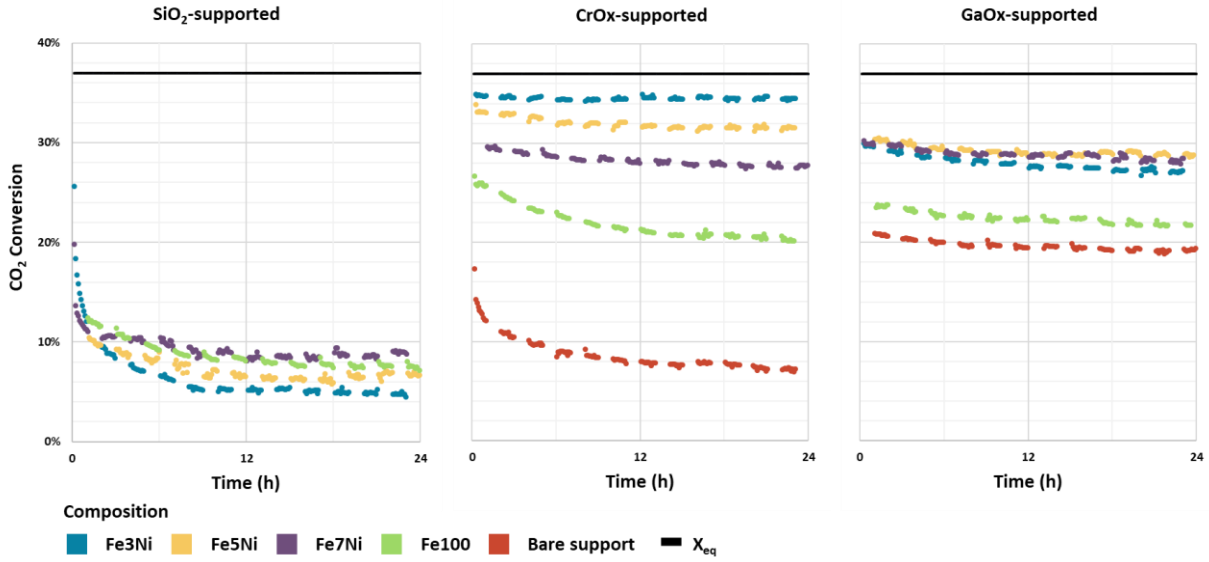

Figure 6-1: CO_2 conversions obtained during catalytic performance evaluation of MOx-supported $(Ni_xFe_{1-x})Fe_2O_4$ nanoparticles under RWGS conditions.

The CrOx-supported samples behave very differently to the SiO_2-supported samples. The bare $CrOx@Al_2O_3$ overlayer shows a comparable deactivation profile to the SiO_2-samples. Pure iron on the overlayer, $Fe100/CrOx@Al_2O_3$, shows that the addition of metallic Fe dispersed onto the support adds activity as expected, but the deactivation profile of the underlying $CrOx@Al_2O_3$ is still apparent. For the alloy compositions however, the deactivation of $CrOx@Al_2O_3$ is overcome and all alloy samples show little to no deactivation with TOS. The catalytic activity is substantially increased on $CrOx@Al_2O_3$ in the presence of the alloy compared to SiO_2. As an illustrative example, the CO_2 conversion for Fe3Ni improves from 5 % to 35 % when supported on $CrOx@Al_2O_3$ instead of SiO_2. A similar improvement in activity is observed for every metallic composition studied. Enhanced catalytic activity on a reducible support compared to an irreducible support has also been observed by Porosoff and Chen (2013) in the catalytic reduction of CO_2 by H_2 and by Raseale et al. (2021) in CO_2-ODH.

Interestingly, the trend in activity with iron content is reversed from what was observed on SiO_2, and there is no difference in the comparative performance between compositions at 1 hour and 24 hours TOS. For the alloy catalysts, activity consistently increases as Fe content decreases: the CO_2 conversion is 34 %, 32 % and 28 % on CrOx-support Fe3Ni, Fe5Ni and Fe7Ni respectively after 24 hours. The most active sample is $Fe3Ni/CrOx@Al_2O_3$, which has the greatest Ni content. For emphasis, while on SiO_2 all supported samples show a similar activity, there is a clear difference in the performance of Fe100 on $CrOx@Al_2O_3$ compared to the alloy samples. On $CrOx@Al_2O_3$, the overall activity of the alloy samples

is greater than the sum of the bare overlayer support and the metallic samples without support effects (i.e., on SiO_2), suggesting a synergistic effect between the Fe-Ni alloy and the active supports.

The overall activity of the GaOx-supported samples is higher than on SiO_2 but not as high as on $CrOx@Al_2O_3$. These samples display the best relative stability, with all samples deactivating only slightly with time on stream. Again, all the alloy samples have improved activity compared to the pure Fe catalyst Fe100/GaOx, however this improvement is not as dramatic as on $CrOx@Al_2O_3$. The alloy samples all have a similar initial activity – no clear comparisons between alloy compositions can be made within the first two hours of reaction. However, after 24 hours under reaction conditions, the samples containing more Fe, $Fe5Ni/GaOx@Al_2O_3$ and $Fe7Ni/GaOx@Al_2O_3$, have higher activity than the sample containing the least Fe, $Fe3Ni/GaOx@Al_2O_3$. This is comparable to the trend observed on SiO_2.

Upon closer inspection it appears that $Fe5Ni/GaOx@Al_2O_3$ has a higher activity after 24 hours than $Fe7Ni/GaOx@Al_2O_3$, however this cannot be reliably concluded as the difference between the two is small and within the error range of the experiment. A potential cause for error between experiments is fluctuations in gas flows, both in the absolute volumetric amounts and the relative amounts which could change the actual H_2:CO_2 ratio in the reactor, and hence the equilibrium conversion. Additionally, this can cause minor differences in the actual space velocity in the reactor when normalised for total metallic loading, along with the small variances in the catalyst mass loaded into the reactor and nanoparticle loading on the support. For this reason, the observation on Fe content is generalised on $GaOx@Al_2O_3$ – the two samples with higher Fe have a higher activity than the alloy sample with the least Fe.

The difference between the CO_2 conversion of $Fe5Ni/GaOx@Al_2O_3$ and $Fe7Ni/GaOx@Al_2O_3$ after 24 hours can be resolved by running the samples at a lower SV i.e., achieving a CO_2 conversion closer to equilibrium conversion of 37 %. This will reduce the relative impact of any catalyst loading and/or packing error on CO_2 conversion.

6.2 SELECTIVITY

Figure 6-2 below shows the results of CO selectivity with TOS. As mentioned in section 4.4.3 above, CO selectivity is calculated as the percentage share of total carbon products, shown to be CO and CH_4. This is validated by the computation of a total carbon balance for each data point, which closes within 99 % in all cases (See Appendix D: Carbon Balance data for RWGS runs). Noting the scale of the y-axis, the carbon monoxide selectivity is extremely high, above 99%, with no significant trends discernable between samples. The balance of this is a small amount of CH_4 that is detected, but this high selectivity suggests CO and CO_2 methanation is kinetically suppressed on the samples although it is

thermodynamically favored over the RWGS at these conditions (see Figure 2-4). This indicates a high degree of catalytic effectiveness.

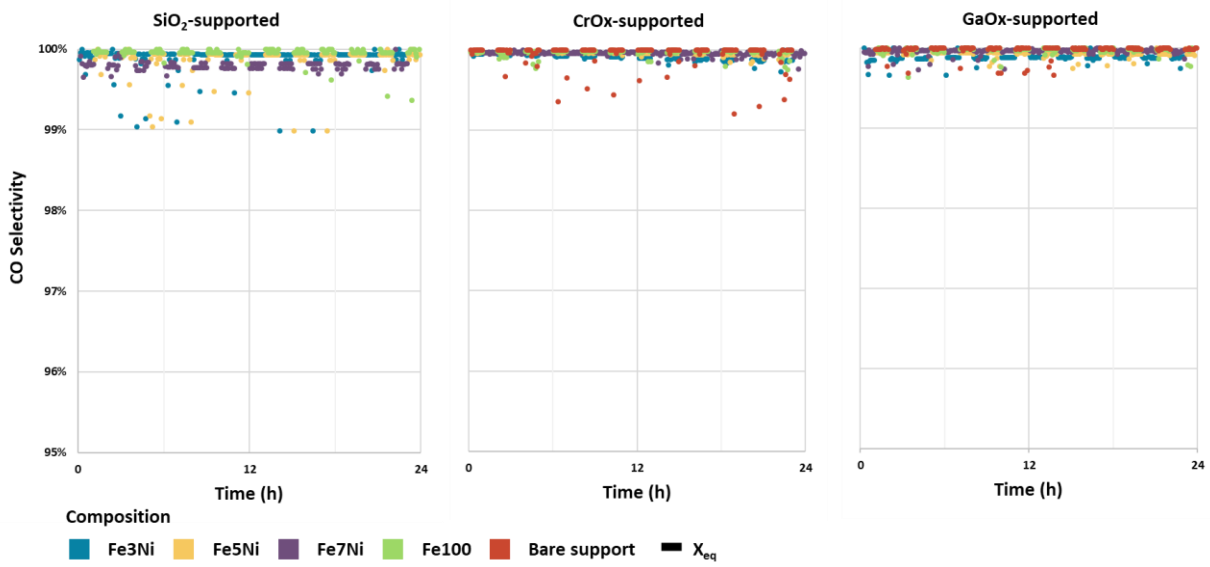

Figure 6-2: CO selectivity results obtained during catalytic performance evaluation of MOx-supported (Ni_xFe_{1-x})Fe_2O_4 nanoparticles under RWGS conditions.

6.3 SPENT CATALYST CHARACTERIZATION

After 24 hours under RWGS conditions, the samples were passivated at room temperature and subjected to spent catalyst characterization. This is done to understand the deactivation of the samples with time on stream, which is rapid and significant in the case of the SiO_2-supported samples and more gradual or even absent for the MOx overlayer-supported samples. Offline XRD was used to analyze the crystalline phases present in the spent samples in comparison to the freshly reduced and passivated sample. XRD can determine the extent to which bulk oxidation and/or sintering can possibly explain catalyst deactivation. Raman spectroscopy was used to determine the extent to which carbon deposition might influence catalyst deactivation.

6.3.1 XRD

Figure 6-3A shows a comparison of the freshly reduced and spent SiO_2-supported samples after 24 hours under RWGS conditions. In the freshly reduced bimetallic samples, the mixture of bcc and fcc alloy phases is observed, increasing the proportion of the bcc phase as expected with an increase in iron content (See Chapter 5.3.2). For Fe100/SiO_2, only a bcc phase corresponding with metallic Fe is detected. The spent samples show that for the bimetallic samples, the intensity of the bcc phase is reduced in all cases while the intensity of the fcc phase is increased. This suggests that the bcc phase is partially consumed. Importantly, no bulk re-oxidation is detected in any of the samples, though the possibility of amorphous oxides or concentrations below the detection limit cannot be ruled out from

XRD analysis of the spent samples. Fe100/SiO_2 is largely unchanged, which is consistent with the findings from Kim et al. (2015) who found the surface structure of their unsupported metallic Fe nanoparticles was unchanged and did not experience significant sintering under comparable RWGS conditions.

Figure 6-3B shows the freshly reduced and RWGS spent CrOx-supported samples. The freshly reduced samples contain the mixture of bcc and fcc alloy phases with an increase in iron content increasing the proportion of bcc phase, as expected. Unlike on SiO_2, here there is no bcc phase detected in any of the spent bimetallic samples. This could suggest that it is completely consumed over the course of the reaction, however the possibility that the reflexes from the underlying γ-Al_2O_3 hinder the detection of any residual bcc phase cannot be ruled out. Again, no re-oxidation back to the spinel structure is detected, but the absence of amorphous oxides cannot be confirmed. The same observations are made on the GaOx-supported samples, seen in Figure 6-3C below.

Table 6-1 below shows a comparison of the volume-weighted average crystallite sizes (d_V) in the freshly reduced and spent supported catalyst samples. The crystallite sizes were computed using the Scherrer equation applied to the fcc reflex at 51° for the bimetallic samples and the bcc reflex at 52° for the pure iron samples. This approach is limited in determining the absolute crystallite size (see Chapter 5.1.4 for discussion) but the trends across samples are relevant. From this analysis, it is apparent that some sintering has occurred in all samples. The sintering detected is not enough to explain the rapid, significant deactivation observed in the SiO_2-supported samples, as well as Fe100/CrOx. It may however account for the gradual deactivation observed in the MOx-supported samples. For emphasis, this XRD analysis of the spent samples shows that the rapid catalyst deactivation seen on the SiO_2-supported samples cannot be explained by bulk oxidation or significant sintering.

Table 6-1: Comparison of select volume-weighted average crystallite sizes (d_V) in freshly reduced vs spent supported catalyst samples. For bimetallic samples, the fcc reflex at 51° was used to compute crystallite size. For the pure Fe samples, the bcc reflex at 52° was used.

Sample	Reduced d_V (nm)	Spent d_V (nm)
Fe3Ni/SiO_2	16.6	22.3
Fe5Ni/SiO_2	17.6	24.1
Fe7Ni/SiO_2	21.4	32.2
Fe100/SiO_2	10.3	12.2
Fe3Ni/CrOx	17.8	23.6
Fe5Ni/CrOx	15.0	17.8
Fe7Ni/CrOx	26.3	27.1
Fe3Ni/GaOx	17.7	27.3

Fe5Ni/GaOx	17.2	26.9
Fe7Ni/GaOx	17.0	27.6

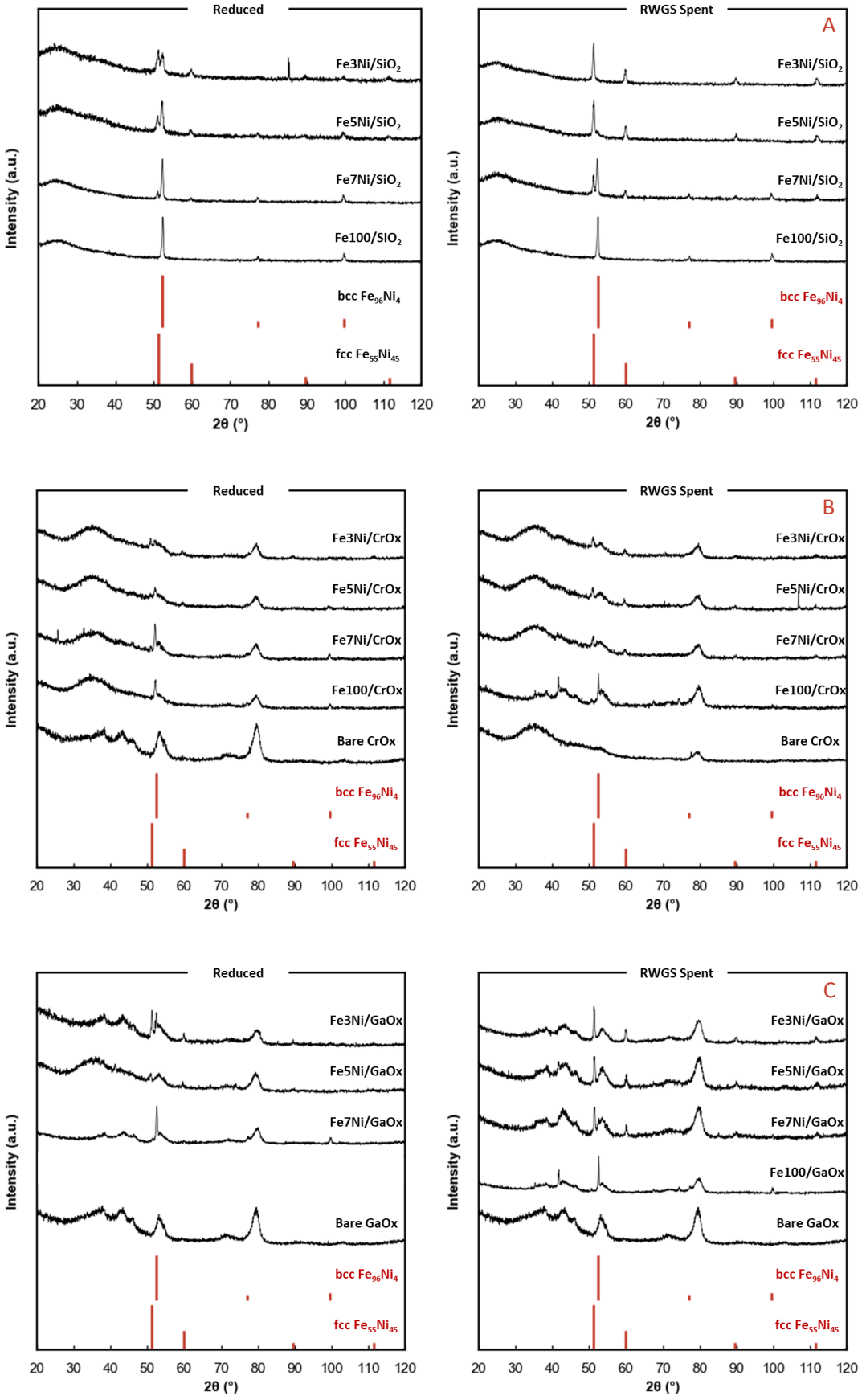

Figure 6-3: Offline XRD of freshly reduced (left) samples and the corresponding spent and passivated samples (right) after 24 hours under RWGS conditions for Fe_xNi_y nanoparticles supported on SiO_2 (A), $CrOx@Al_2O_3$ (B) and $GaOx@Al_2O_3$ (C)

6.3.2 Raman spectroscopy

Figure 6-4 below shows a comparison of the Raman spectra of the spent catalysts after exposure to RWGS conditions for 24 hours. There was no detectable carbon deposition, evident by the absence of characteristic bands at 1600 cm^{-1} and 1350 cm^{-1} for surface carbon. While a small degree of carbon deposition cannot be ruled out due to the site-sensitivity of the technique and detection limits of the instrument, carbon deposition is not a plausible mechanism to explain the significant deactivation seen in the SiO_2-supported samples and bare $CrOx@Al_2O_3$ overlayer. In addition, the characteristic bands associated with bulk MOx are not present in either Bare $CrOx@Al_2O_3$ or Bare $GaOx@Al_2O_3$ samples, suggesting there is no sintering of MOx into crystallites under reaction conditions and that the 2D overlayer dispersed onto the γ-Al_2O_3 surface is stable.

For emphasis, this Raman spectroscopy analysis of the spent samples shows that the rapid catalyst deactivation seen on the SiO_2-supported samples cannot explained by carbon deposition.

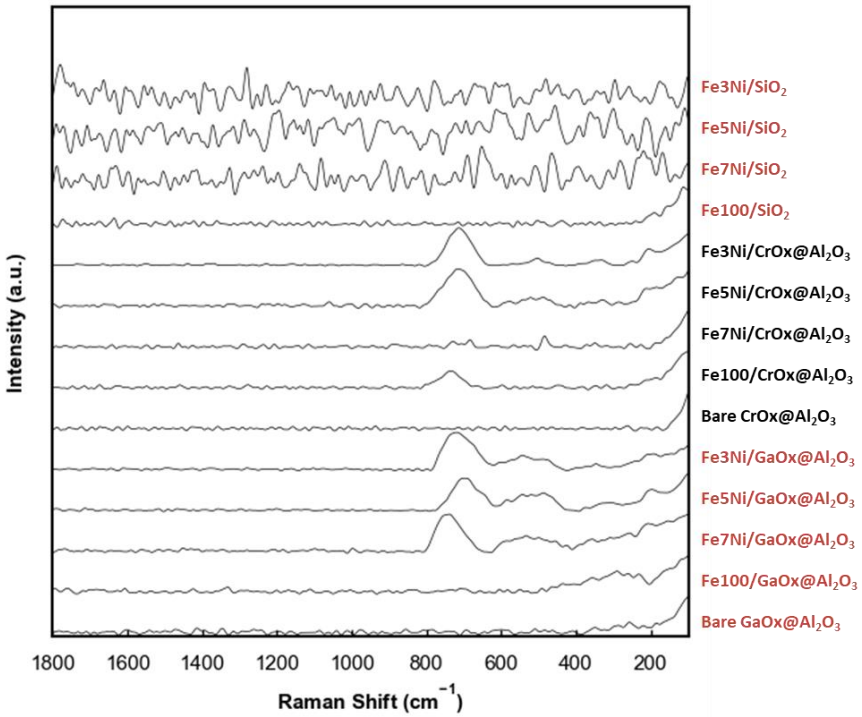

Figure 6-4 Comparison of the Raman spectra of the spent catalysts after exposure to RWGS conditions for 24 hours.

6.4 *IN-SITU* XRD UNDER RWGS CONDITIONS

The spent catalyst characterization discussed above suggests that the rapid deactivation of the SiO2-supported samples cannot be explained by sintering, bulk oxidation and/or significant carbon deposition alone. Moreover, the absence of the bcc alloy phase in any of the $MOx@Al_2O_3$-supported samples suggests that this phase is consumed under reaction conditions. To better understand the phase evolution under reaction conditions, $Fe7Ni/SiO_2$ was studied with *in-situ* XRD in the XRK-900

cell. This sample was chosen as it deactivated rapidly under RWGS conditions and it has a high weight fraction of the bcc alloy phase after reduction, so changes to this phase should be easily detected. The sample was reduced as previously described then exposed to a flow of 5 % each H_2 and CO_2 in Ar while XRD scans were taken every 5 minutes. The results are presented in Figure 6-5 below, showing the top-view of obtained XRD scans (left), refined crystallite sizes of the bcc and fcc alloy phases present in the sample (top) and refined weight compositions of the bcc and fcc alloy phases (bottom). Phase evolution cannot be directly compared to the RWGS fixed-bed results with respect to time on stream due to the different testing conditions, including but not limited to different space velocities and flow patterns through the reactor.

The beginning of the top-view graph shows the familiar phase composition of the freshly reduced Fe7Ni/SiO_2 sample (see Figure 5-8). From ~5 hours TOS, the reflex for the fcc phase at 0.48 $Å^{-1}$ appears below the reflex for the bcc phase at 0.49 $Å^{-1}$. This fcc reflex intensifies over the course of reaction while the bcc phase is diminished. This is supported by modelled phase compositions which show a gradual decrease in the concentration of the bcc phase and corresponding increase in the concentration of the fcc phase with TOS. This confirms what could be inferred from spent catalyst characterization – that the bcc phase is transformed to the fcc phase under RWGS conditions. With reference to the literature presented on RWGS catalysis (see Chapter 2.1.2), this likely proceeds via a Mars van Krevelen-type mechanism in which the bcc phase is oxidized by and then re-reduced to an fcc alloy phase by H_2. The oxide phase would exist as a temporary surface species in small concentration and is therefore not detected by XRD. The re-reduction to an fcc phase instead of a bcc phase at this temperature agrees with the bulk Fe-Ni phase diagram presented earlier (see Figure 2-7). The refined crystallite sizes for each phase are very stable, confirming that sintering of the active phases is not a major deactivation mechanism for this system as suggested by spent catalyst characterization.

6.5 DISCUSSION OF CATALYTIC PERFORMANCE IN CONTEXT OF MATERIAL CHARACTERISATIONS

It is the goal of the present work to further study the materials prepared by Raseale et al. (2021) in the RWGS. This work has shown that while all samples tested were RWGS active and suppressed methanation, catalytic activity is significantly altered by both varying the iron content in an Fe-Ni alloy and varying the chemical nature of the MOx support. For emphasis, it's been shown that the metallic phases of Fe and Fe-Ni alloys in the absence of a support are RWGS active, likewise are the bare MOx@Al_2O_3 overlayers, but that depositing the alloys onto the supports creates an overall activity that is potentially greater than the sum of these two parts.

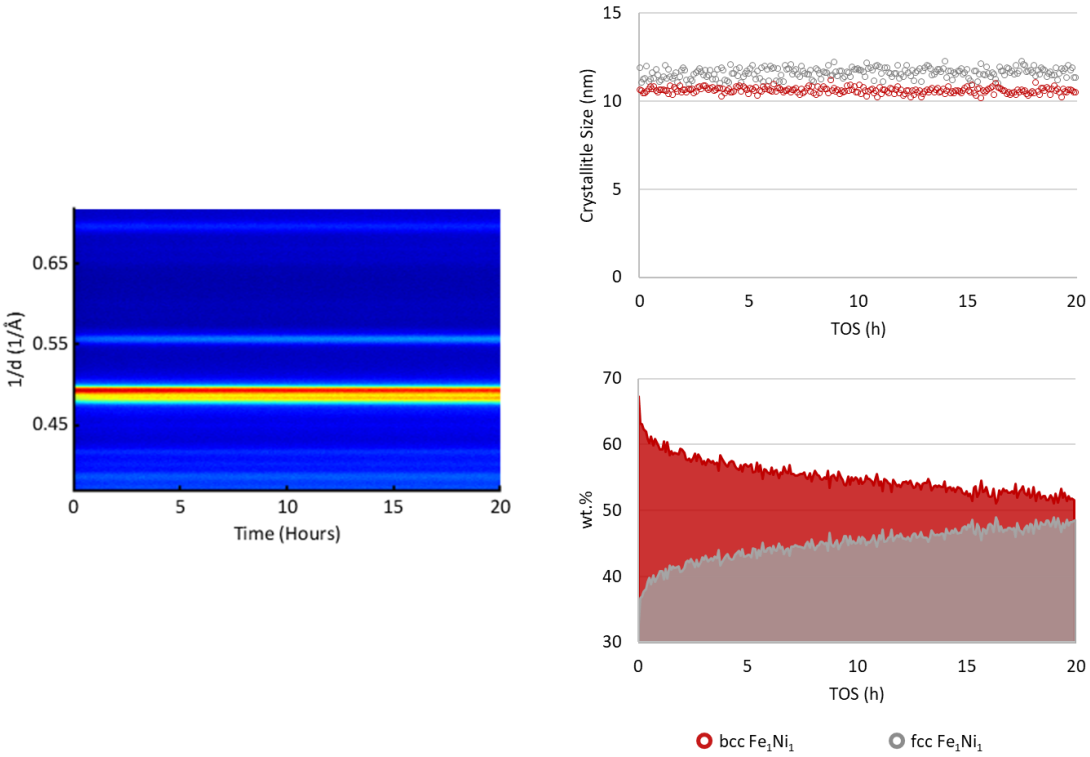

Figure 6-5: Top view of in-situ XRD patterns (left), evolution of crystallite size (top) and phase evolution (bottom) of RWGS experiments performed in the in-situ XRD over Fe7Ni/SiO_2.

To unpack the results of catalytic performance evaluation, it must be emphasized that the observed differences in activity and stability do not appear to be related to deactivation via sintering, bulk oxidation, and major carbon deposition. In terms of sintering, the spent catalyst characterization shows limited sintering across all samples, which was further supported by the refinement of the *in-situ* XRD RWGS run shown in Figure 6-5 above. It is possible that there is undetected oxidation or carbon deposition, though not to a degree which would explain the deactivation observed.

The observed differences are also not an effect of nanoparticle size. Smaller particles can be more active due to the increase in catalytically active specific surface area (Van Santen, 2009). If this were the case, it would be expected that the activity of the supported bimetallic catalysts would increase with a decrease in nanoparticle size, i.e., for CO_2 conversion, Fe3Ni > Fe5Ni > Fe7Ni (see Table 5-2 for particle size). However, the opposite trend is observed on the SiO_2-supported catalysts, and there is little difference in performance on the GaOx-supported catalysts. This trend could hold for the CrOx-supported catalysts in isolation but not in the context of the results on the other two supports.

The difference in performance, once a stabilized conversion is reached, is likely a function of the Ni content of the fcc phase, which was the only metallic phase present in the spent MOx@Al_2O_3 catalyst samples. This is not in agreement with the first hypothesis detailed in Chapter 3.2.1 above which stated that activity and selectivity in the RWGS over Fe_xNi_y alloy catalysts would increase with an

increase in Fe content because an increase in Fe improves the stability of the bcc allotrope of the Fe-Ni alloy. This is unsurprising as it was formulated based off the results from Raseale et al. (2021) who did not see any activation of CO_2 by the fcc phase of the Fe-Ni alloy and concluded that the bcc phase was active while the fcc phase was inert. This was probably due to the relative intensities of the bcc and fcc alloy phases in their studied compositions. Specifically, the intensity of the fcc phase was too strong in the Fe1Ni1 system and too weak in Fe5Ni1 system for changes to be detected. The reduced Fe3Ni1 system studied in this work allowed for changes in the bcc and fcc phases to be clearly observed. This work showed that while the bcc phase has a greater affinity for re-oxidation than the fcc phase, the fcc phase activates CO_2 at elevated temperatures, and that there is some interaction between the fcc phase of the Fe-Ni and a reducible support that sustains catalytic activity at elevated temperatures.

The first hypothesis further stated that under RWGS reaction conditions, CO_2 is activated on the bcc surface of an Fe_xNi_y alloy via a Mars van Krevelen – type mechanism in which the bcc phase is oxidized by O* and regenerated by H*, completing the catalytic cycle. The combined results of CO_2 activation (see Figure 5-15) and the *in-situ* XRD RWGS run (see Figure 6-5) suggest that this Mars van Krevelen – type mechanism does take place through the oxide, but that the bcc phase isn't regenerated. Rather, the oxide is re-reduced to an fcc phase. However, a complete catalytic cycle is demonstrated.

The second hypothesis detailed in section 3.2.2 above stated that catalytic performance will be improved when oxidic Fe_xNi_y precursors are deposited on supports of increasing reducibility and that the support participates in the RWGS mechanism through the provision of a reactive oxygen vacancy on which CO_2 is reduced to CO. While there is not enough evidence to comment on mechanisms in that detail, there is ample evidence that both the reducible support and metallic phase are required for a stable RWGS catalyst. With reference to Figure 5-15 above, the bare $CrOx@Al_2O_3$ showed no CO formation under oxidizing conditions during CO_2 activation experiments but showed moderate activity under RWGS conditions (see Figure 6-1). This supports the hypothesis that when H_2 in introduced to the system the partial reduction of $CrOx@Al_2O_3$ can provision an oxygen vacancy which enhances CO_2 activation. It is also possible that a new RWGS-active site is introduced at the Fe_xNi_y-MOx interface, as was proposed by Yan, Binhang et al. (2019).

The reducibility argument does not explain the enhanced performance seen on the bare $GaOx@Al_2O_3$ overlayer or the GaOx-supported samples. The Lewis acidity of the $MOx@Al_2O_3$ supports is a second variable which may be playing a role which was not explored in this work and $GaOx@Al_2O_3$ has greater surface acidity than $CrOx@Al_2O_3$ (Raseale, 2022). It is also possible that $GaOx@Al_2O_3$ is partially reducible under reaction conditions.

In the context of the reaction mechanisms presented in chapter 2.1.2, this work provides evidence for a bifunctional catalyst system on the active supports, $CrOx@Al_2O_3$ and $GaOx@Al_2O_3$. It was stated in chapter 2.1.3 that catalytic features required for effective RWGS catalysis are good CO_2 adsorption, to encourage a high activity at desired lower temperatures, and facile CO desorption to prevent its hydrogenation to undesired products thus to ensure high CO selectivity. To explain the differences in catalytic performance between metallic compositions and across active supports, it is proposed that the better performing catalysts have the correct balance of CO_2 activation provided by the alloy phases and spillover capacity provided by the support. However, the specific chemical properties resulting in the differences between compositions and across supports cannot be identified with the characterizations carried out so far.

The combined results of this work suggest the following could be taking place on the catalyst surface. When only metallic phases are present, CO_2 is activated and reduced to CO on the bcc allotrope of the Fe_xNi_y alloy, which is oxidized as a result. The resultant oxide is re-reduced by H_2; however, it is re-reduced to the fcc phase, which is lower in activity compared to the bcc phase. This results in a net consumption of the more active bcc phase, which explains the deactivation seen on the SiO_2-supported samples. On the active $MOx@Al_2O_3$ supports however, there is evidence of a tandem mechanism between the alloy nanoparticles and the supports. This is based off the observation that both the alloys themselves (i.e., on SiO_2) and the bare $MOx@Al_2O_3$ supports are RWGS active, but when the alloy is anchored on the supports, the observed CO_2 conversion is greater than the expected, added conversions of the alloys and the supports, suggesting a synergistic effect. This could be the result of enhanced H_2 activation on the fcc phase leading to enhanced CO_2 activation on the MOx support through a spillover-type mechanism, or the creation of new active sites at the fcc-MOx interface which are RWGS active.

7. CONCLUDING REMARKS

The combined results of this work suggest the following

- CO_2 activation is more facile on the bcc allotrope of an iron-nickel alloy surface. On SiO_2, the inert support, the bcc allotrope is oxidized during CO_2 activation and is re-reduced by H_2 under RWGS conditions. It is re-reduced to the fcc phase, which is lower in activity. This results in a net consumption of the more active bcc phase, which leads to a loss of catalytic activity with time on stream.
- In isolation and without support effects, the fcc allotrope of an iron-nickel alloy surface is inactive for CO_2 activation but is stable and resists bulk oxidation, carbon deposition or sintering of crystallites
- Both the Fe_xNi_y alloys themselves (on inert SiO_2) and the bare MOx@Al_2O_3 supports are RWGS active, but when the alloy is deposited on the supports, there is an overall activity which is greater than the sum of the two parts, suggesting a synergistic effect. On these catalytically active supports there is evidence of a tandem mechanism for the RWGS reaction. Some interaction between the fcc allotrope of the iron-nickel alloy and different MOx support materials allows for the catalytic activity to be sustained, though the exact nature of the interaction cannot be pin-pointed by the characterization techniques employed in this work.
- Possible untested explanations for the enhanced activity of the fcc phase on the MOx supports could be enhanced H_2 activation on the fcc phase leading to enhanced CO_2 activation on the support through a H^+ spillover effect, or the creation of new active sites at the fcc-MOx interface which are RWGS active.

8. RECOMMENDATIONS AND FUTURE WORK

To further study the Fe_xNi_y-based catalytic system while maintaining a high CO selectivity the following experimental approaches are recommended:

To test whether surface oxidation is responsible for the deactivation of the SiO_2-supported samples, the regeneration of the samples by H_2 can be attempted in the fixed bed set-up. In these proposed experiments, the SiO_2-supported samples undergo RWGS testing as done previously. After 24 hours or once the samples have deactivated, they will be re-exposed to the reduction conditions used for *in-situ* catalyst activation. The potentially reactivated catalysts will then be exposed to RWGS testing conditions again with product gas analysis via the online GC-TCD. If there is surface oxidation, it is expected that after this reduction treatment, an increase in activity will be observed. This is of particular interest in the case of the deactivation of $Fe100/SiO_2$, which, from spent catalyst characterization, cannot be explained by bulk oxidation, major carbon deposition, sintering or the transformation of an active bcc phase to a less active fcc phase.

This work demonstrates that the chemical properties of a MOx support material have profound impacts on catalytic activity and stability in the RWGS. To further understand the interaction of the fcc phase of the Fe-Ni alloy with the $MOx@Al_2O_3$, it is recommended that further MOx supports be screened for RWGS activity. It is recommended that the Fe3Ni (Fe:Ni = 3:1) system be used for further MOx screening, as XRD of the reduced nanoparticles have a relative intensity between the bcc and fcc alloy phases that is useful in clearly showing changes in these phases under different experimental conditions. Moreover, the best performing sample overall was $Fe3Ni/CrOx@Al_2O_3$. It is recommended that the overlayer synthesis approach be continued in screening various MOx overlayers, rather than the use of bulk supports, to continue to limit the effect of varying textural properties of the carrier materials on catalytic performance evaluation. In addition to Cr and Ga which were studied in this work, $MOx@Al_2O_3$ overlayers have been successfully synthesized with oxides of Sm, Ti, V, and Zr by Raseale et al. (2021) in addition oxides of Y, Ta, W synthesized by Prieto et al. (2015). The aim of this $Fe3Ni@MOx@Al_2O_3$ screening would be to explore and expand on the chemical properties of the MOx which are potential descriptors for observed differences in RWGS performance such as reducibility and/or Lewis acid−base character.

It is stated in chapter 5.2.2 that the overlayer support materials are understood as surface-modified γ-Al_2O_3 rather than as directly comparable to their respective bulk oxides. In addition to the further screening of $MOx@Al_2O_3$ materials, it is recommended that bulk MOx supports be screened, again using the Fe3Ni system as reasoned above. This is because the chemistry of the MOx may be different in the bulk state compared to the overlayer state, particularly for transition metals such as Cr and Zr

which can exist in multiple oxidation states with widely varying chemical properties. In addition, while the $MOx@Al_2O_3$ overlayer approach is useful in decoupling the chemical properties of a support from its physical properties for the purposes of comparison of catalytic performance, bulk supports are more attractive in commercial catalyst development, owing to their ease of synthesis and availability.

9. REFERENCES

Bukur, D.B., Todic, B. & Elbashir, N. 2016. Role of water-gas-shift reaction in Fischer–Tropsch synthesis on iron catalysts: A review. *Catalysis Today.* 275:66-75.

Cheng, Z., Sherman, B.J. & Lo, C.S. 2013. Carbon dioxide activation and dissociation on ceria (110): a density functional theory study. *J Chem Phys.* 138(1):014702. DOI:10.1063/1.4773248.

Daza, Y.A. & Kuhn, J.N. 2016. CO2conversion by reverse water gas shift catalysis: comparison of catalysts, mechanisms and their consequences for CO2conversion to liquid fuels. *RSC Advances.* 6(55):49675-49691. DOI:10.1039/c6ra05414e.

Fischer, N., van Steen, E. & Claeys, M. 2013. Structure sensitivity of the Fischer–Tropsch activity and selectivity on alumina supported cobalt catalysts. *Journal of Catalysis.* 299:67-80. DOI:10.1016/j.jcat.2012.11.013.

Ginés, M.J.L., Marchi, A.J. & Apesteguía, C.R. 1997. Kinetic study of the reverse water-gas shift reaction over CuO/ZnO/A1203 catalysts *Applied Catalysis A: General.* 154(1-2):155-171.

IEA. 2020. Key World Energy Statistics 2020. *IEA.* Paris. Available: https://www.iea.org/reports/key-world-energy-statistics-2020.

IPCC. 2014. *Climate Change 2014: Synthesis Report. Contribution of Working Groups I, II and III to the Fifth Assessment Report of the Intergovernmental Panel on Climate Change*. Geneva, Switzerland.

IPCC. 2018. *Global Warming of 1.5°C. An IPCC Special Report on the impacts of global warming of 1.5°C above pre-industrial levels and related global greenhouse gas emission pathways, in the context of strengthening the global response to the threat of climate change*. Geneva, Switzerland.

Jing, P., Liu, M., Pu, Y., Cui, Y., Wang, Z., Wang, J. & Liu, Q. 2016. Dependence of phase configurations, microstructures and magnetic properties of iron-nickel (Fe-Ni) alloy nanoribbons on deoxidization temperature in hydrogen. *Sci Rep.* 6:37701. DOI:10.1038/srep37701.

Kaiser, P., Unde, R.B., Kern, C. & Jess, A. 2013. Production of Liquid Hydrocarbons with CO2as Carbon Source based on Reverse Water-Gas Shift and Fischer-Tropsch Synthesis. *Chemie Ingenieur Technik.* 85(4):489-499. DOI:10.1002/cite.201200179.

Kim, D.H., Han, S.W., Yoon, H.S. & Kim, Y.D. 2015. Reverse water gas shift reaction catalyzed by Fe nanoparticles with high catalytic activity and stability. *Journal of Industrial and Engineering Chemistry.* 23:67-71. DOI:10.1016/j.jiec.2014.07.043.

Ko, J., Kim, B.-K. & Han, J.W. 2016. Density Functional Theory Study for Catalytic Activation and Dissociation of CO2 on Bimetallic Alloy Surfaces. *The Journal of Physical Chemistry C.* 120(6):3438-3447. DOI:10.1021/acs.jpcc.6b00221.

Martinezhuerta, M., Gao, X., Tian, H., Wachs, I., Fierro, J. & Banares, M. 2006. Oxidative dehydrogenation of ethane to ethylene over alumina-supported vanadium oxide catalysts: Relationship between molecular structures and chemical reactivity. *Catalysis Today.* 118(3-4):279-287. DOI:10.1016/j.cattod.2006.07.034.

Mikkelsen, M., Jørgensen, M. & Krebs, F.C. 2010. The teraton challenge. A review of fixation and transformation of carbon dioxide. *Energy Environ. Sci.* 3(1):43-81. DOI:10.1039/b912904a.

Munnik, P., de Jongh, P.E. & de Jong, K.P. 2015. Recent developments in the synthesis of supported catalysts. *Chemical reviews.* 115(14):6687-6718.

Porosoff, M.D. & Chen, J.G. 2013. Trends in the catalytic reduction of CO2 by hydrogen over supported monometallic and bimetallic catalysts. *Journal of Catalysis.* 301:30-37. DOI:10.1016/j.jcat.2013.01.022.

Porosoff, M.D., Yan, B. & Chen, J.G. 2016. Catalytic reduction of CO2 by H2 for synthesis of CO, methanol and hydrocarbons: challenges and opportunities. *Energy & Environmental Science.* 9(1):62-73. DOI:10.1039/c5ee02657a.

Predel, B. 1995. Fe-Ni (Iron-Nickel): Datasheet from Landolt-Börnstein - Group IV Physical Chemistry · Volume 5E: "Dy-Er – Fr-Mo" in SpringerMaterials (https://doi.org/10.1007/10474837_1321). O. Madelung, Ed.: Springer-Verlag Berlin Heidelberg.

Prieto, G., De Mello, M.I.S., Concepción, P., Murciano, R., Pergher, S.B.C. & Martínez, A.n. 2015. Cobalt-Catalyzed Fischer–Tropsch Synthesis: Chemical Nature of the Oxide Support as a Performance Descriptor. *ACS Catalysis.* 5(6):3323-3335. DOI:10.1021/acscatal.5b00057.

Raseale, S. 2022. Oxidative dehydrogenation of ethane with carbon dioxide over iron-nickel nano-alloys supported on metal oxide overlayers. University of Cape Town.

Raseale, S., Marquart, W., Jeske, K., Prieto, G., Claeys, M. & Fischer, N. 2021. Supported FexNiy catalysts for the co-activation of CO2 and small alkanes. *Faraday Discuss.* 229:208-231. DOI:10.1039/c9fd00130a.

Savaresi, A. 2016. The Paris Agreement: a new beginning? *Journal of Energy & Natural Resources Law.* 34(1):16-26.

Schmidt, P., Batteiger, V., Roth, A., Weindorf, W. & Raksha, T. 2018. Power-to-Liquids as Renewable Fuel Option for Aviation: A Review. *Chemie Ingenieur Technik.* 90(1-2):127-140. DOI:10.1002/cite.201700129.

Spath, P.L. & Dayton, D.C. 2003. *Preliminary screening--technical and economic assessment of synthesis gas to fuels and chemicals with emphasis on the potential for biomass-derived syngas*.

Su, X., Yang, X., Zhao, B. & Huang, Y. 2017. Designing of highly selective and high-temperature endurable RWGS heterogeneous catalysts: recent advances and the future directions. *Journal of Energy Chemistry.* 26(5):854-867. DOI:10.1016/j.jechem.2017.07.006.

Tollefson, J. 2018. Can the world kick its fossil-fuel addiction fast enough? *Nature.* 556(7702):422-425.

Van Santen, R.A. 2009. Complementary structure sensitive and insensitive catalytic relationships. *Accounts of chemical research.* 42(1):57-66.

Wang, W., Wang, S., Ma, X. & Gong, J. 2011. Recent advances in catalytic hydrogenation of carbon dioxide. *Chem Soc Rev.* 40(7):3703-3727. DOI:10.1039/c1cs15008a.

Wolf, M., Fischer, N. & Claeys, M. 2018. Surfactant-free synthesis of monodisperse cobalt oxide nanoparticles of tunable size and oxidation state developed by factorial design. *Materials Chemistry and Physics.* 213:305-312. DOI:10.1016/j.matchemphys.2018.04.021.

Xiaoding, X. & Moulijn, J. 1996. Mitigation of CO2 by chemical conversion: Plausible chemical reactions and promising products. *Energy & Fuels.* 10(2):305-325.

Xie, Z., Winter, L.R. & Chen, J.G. 2021. Bimetallic-derived catalysts and their application in simultaneous upgrading of CO2 and ethane. *Matter.* 4(2):408-440.

Yan, B., Zhao, B., Kattel, S., Wu, Q., Yao, S., Su, D. & Chen, J.G. 2019. Tuning CO2 hydrogenation selectivity via metal-oxide interfacial sites. *Journal of Catalysis.* 374:60-71. DOI:10.1016/j.jcat.2019.04.036.

Yan, B., Yao, S., Kattel, S., Wu, Q., Xie, Z., Gomez, E., Liu, P., Su, D. et al. 2018. Active sites for tandem reactions of CO2 reduction and ethane dehydrogenation. *Proc Natl Acad Sci U S A.* 115(33):8278-8283. DOI:10.1073/pnas.1806950115.

Yáñez-Vilar, S., Sánchez-Andújar, M., Gómez-Aguirre, C., Mira, J., Señarís-Rodríguez, M.A. & Castro-García, S. 2009. A simple solvothermal synthesis of MFe2O4 (M=Mn, Co and Ni) nanoparticles. *Journal of Solid State Chemistry.* 182(10):2685-2690. DOI:10.1016/j.jssc.2009.07.028.

Yang, L., Pastor-Pérez, L., Villora-Pico, J.J., Gu, S., Sepúlveda-Escribano, A. & Reina, T.R. 2020. CO2 valorisation via reverse water-gas shift reaction using promoted Fe/CeO2-Al2O3 catalysts: Showcasing the potential of advanced catalysts to explore new processes design. *Applied Catalysis A: General.* 593. DOI:10.1016/j.apcata.2020.117442.

Zhu, M., Ge, Q. & Zhu, X. 2020. Catalytic Reduction of CO2 to CO via Reverse Water Gas Shift Reaction: Recent Advances in the Design of Active and Selective Supported Metal Catalysts. *Transactions of Tianjin University.* 26(3):172-187. DOI:10.1007/s12209-020-00246-8.

APPENDIX A: SAMPLE CALCULATION – REQUIRED METAL ACETATE PRECURSOR QUANTITIES FOR FE3NI

Target atomic ratio Fe:Ni = 3:1

1 mol $Fe(O_2CCH_3)_2$ = 1 mol Fe

1 mol $Ni(O_2CCH_3)_2 \cdot 4H_2O$ = 1 mol Ni

Required total precursor mass = 4.1 g

Let the required mass of iron(II) acetate equal x.

Required mass of nickel(II) acetate equals $4.1 - x$.

$$\frac{n_{Fe}}{n_{Ni}} = 3$$

$$\frac{m_{Fe(II)ac}/M_{Fe(II)ac}}{m_{Ni(II)ac}/M_{Ni(II)ac}} = 3$$

$$\frac{x/173.93}{(4.1-x)/248.84} = 3$$

$$x = 3.188\ g$$

$$4.1 - x = 0.912\ g$$

APPENDIX B: PRELIMINARY TESTING TO DETERMINE TESTING SPACE VELOCITY

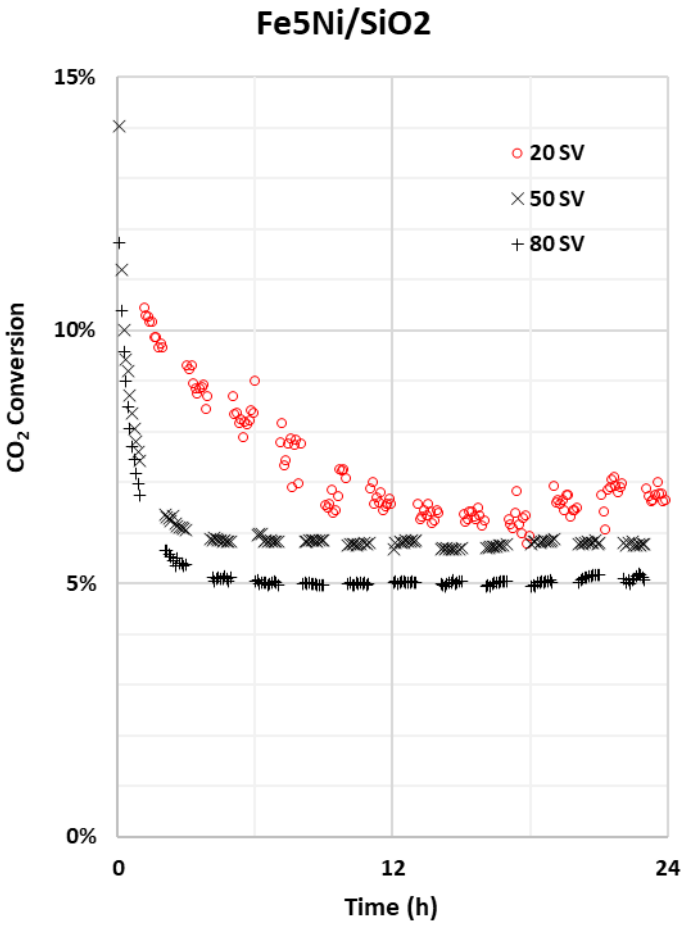

Preliminary RWGS testing to determine future testing space velocity, SV (20 $L \cdot g_{cat}^{-1} \cdot h^{-1}$).

APPENDIX C: LIST OF CHEMICALS

Chemical name	Formula	Supplier	Purity
Acetone	$(CH_3)_2CO$	Kimix	≥ 99.30%
Ammonium hydroxide	NH_4OH	Kimix	25.00 wt.-%
AEROSIL® 200	SiO_2	AEROSIL	≥ 99.8%
Benzyl alcohol	$C_6H_5CH_2OH$	Sigma-Aldrich	≥ 99.90%
Chromium(III) nitrate nonahydrate	$Cr(NO_3)_3 \cdot 9H_2O$	Sigma-Aldrich	≥ 99.90%
Ethanol	CH_3CH_3	Kimix	≥ 99.90%
Gallium(III) nitrate hydrate	$Ga(NO_3)_3 \cdot xH_2O$	Sigma-Aldrich	99.90%
Iron(II) acetate	$Fe(O_2CCH_3)_2$	Sigma-Aldrich	≥ 95.00%
Nickel(II) acetate tetrahydrate	$Ni(O_2CCH_3)_2 \cdot 4H_2O$	Sigma-Aldrich	≥ 98.00%
i-Propanol	$(CH_3)_2CHOH$	Kimix	≥ 99.98%
Puralox SCCa 5-150	γ-Al_2O_3	SASOL	98.00%
Water	H_2O		Deionized

APPENDIX D: SEM-EDX RESULTS FOR UNSUPPORTED FE5NI AND FE7NI NANOPARTICLES

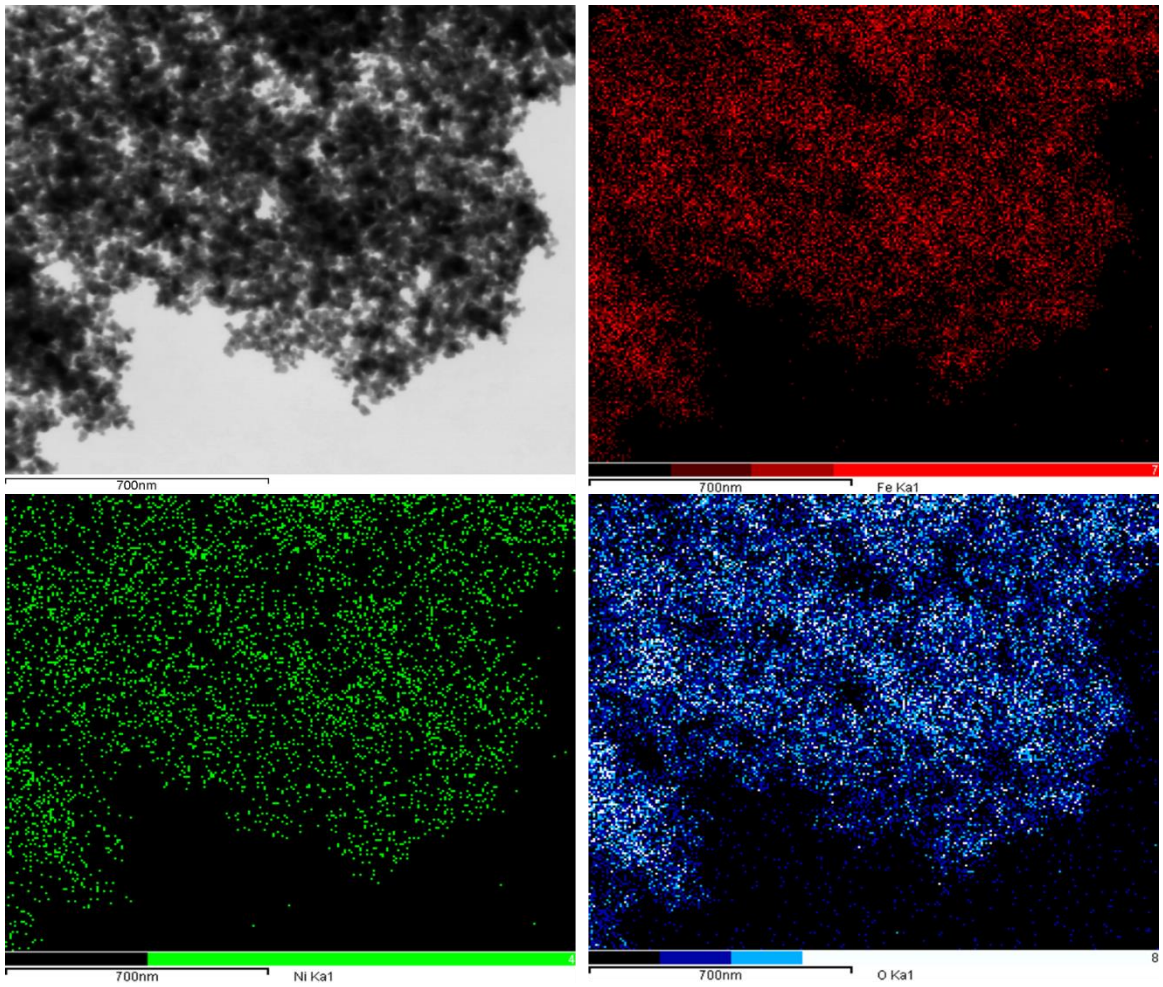

SEM images (top left) and SEM-EDX elemental maps (right) of the as-prepared Fe5Ni nanoparticles. The elemental map for Fe is shown in red (top right), Ni in green (bottom left) and O in blue (bottom right).

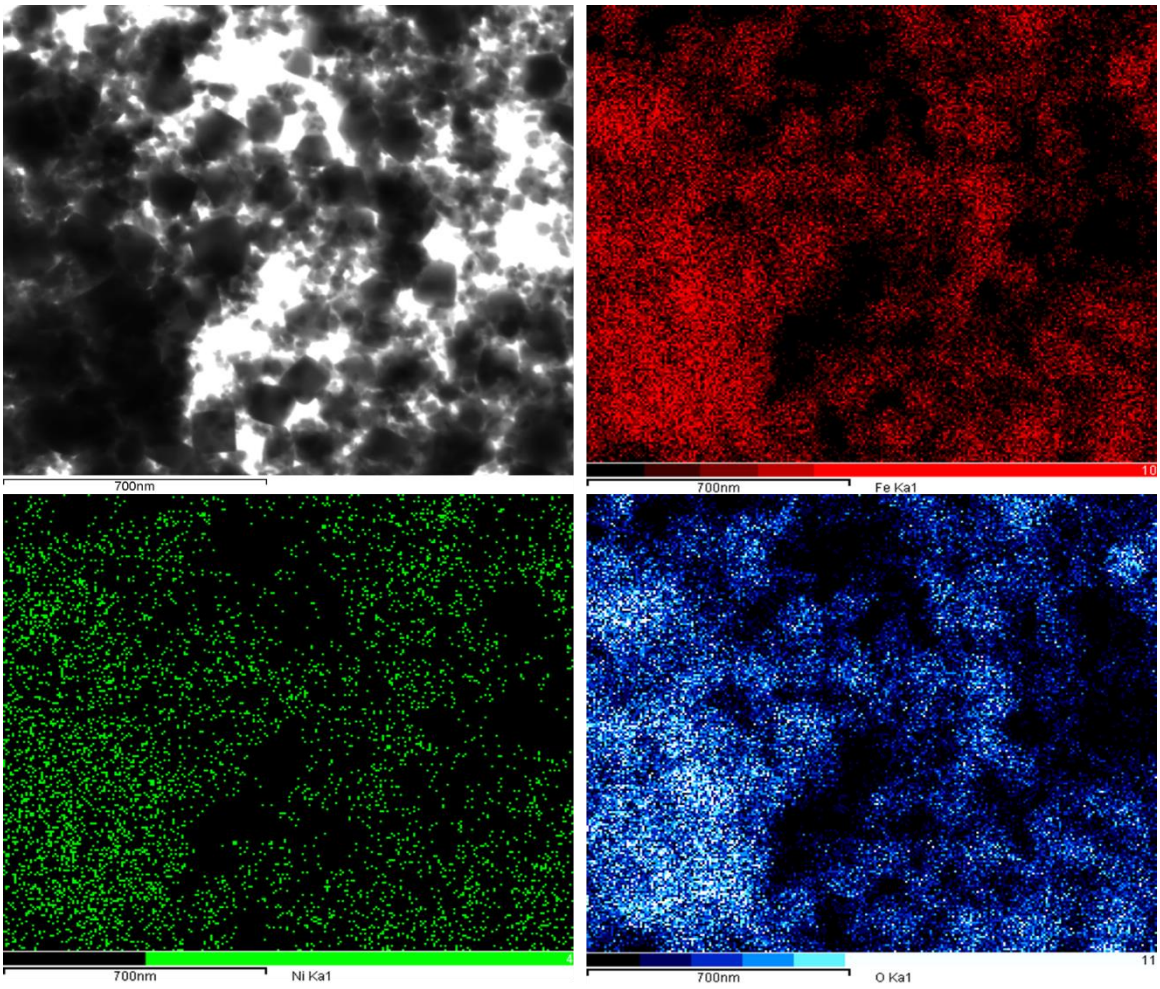

SEM images (top left) and SEM-EDX elemental maps (right) of the as-prepared Fe7Ni nanoparticles. The elemental map for Fe is shown in red (top right), Ni in green (bottom left) and O in blue (bottom right).

APPENDIX D: CARBON BALANCE DATA FOR RWGS RUNS

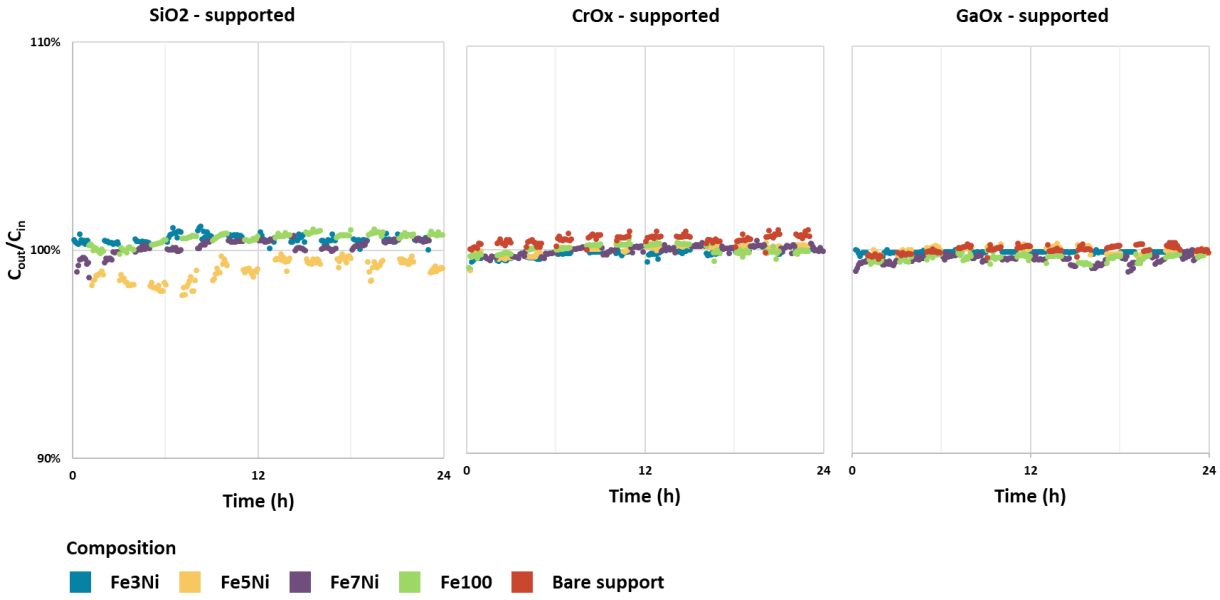

Carbon balance (C_{out}/C_{in}) computed with TOS during catalytic performance evaluation of MOx-supported (Ni_xFe_{1-x})Fe_2O_4 nanoparticles under RWGS conditions.